

Multi-Wavelength Study of Feedback Driven Regions: Star Formation Rate and Efficiency

Thesis

Master of Science

in

Astronomy and Astrophysics

by

Divyansh Chourey

(SC18M018)

Supervised by

Dr. Jessy Jose

Assistant Professor, IISER Tirupati

Dr. Anandmayee Tej

Professor, IIEST Thiruvananthapuram



**Department of Earth and Space Science
Indian Institute of Space Science and Technology
Thiruvananthapuram, India**

July 2020

Certificate

This is to certify that the Thesis titled ***Multi-Wavelength Study of Feedback Driven Regions: Star Formation Rate and Efficiency*** submitted by **Divyansh Chourey**, to the Indian Institute of Space Science and Technology, Thiruvananthapuram, in partial fulfillment for the award of the degree of **Master of Science in Astronomy and Astrophysics** is a bona fide record of the original work carried out by him under my supervision. The contents of this Thesis, in full or in parts, have not been submitted to any other Institute or University for the award of any degree or diploma.

Dr. Anandmayee Tej
Professor
Dept. of Earth and Space Science
IIST, Trivandrum

Dr. Samir Mandal
Associate Professor and HoD
Dept. of Earth and Space Science
IIST, Trivandrum

Dr. Jessy Jose
Assistant Professor
Dept. of Physics
IISER, Tirupati

Place: Thiruvananthapuram
Date: July 2020

Declaration

I declare that this Thesis titled ***Multi-Wavelength Study of Feedback Driven Regions: Star Formation Rate and Efficiency*** submitted in partial fulfillment for the award of the degree of **Master of Science in Astronomy and Astrophysics** is a record of the original work carried out by me under the supervision of **Dr. Jessy Jose**, Assistant Professor, IISER, Tirupati and **Dr. Anandmayee Tej**, Professor, IIIST, Trivandrum, and has not formed the basis for the award of any degree, diploma, associateship, fellowship, or other titles in this or any other Institution or University of higher learning. In keeping with the ethical practice in reporting scientific information, due acknowledgments have been made wherever the findings of others have been cited.

Place: Thiruvananthapuram

Divyansh Chourey

Date: July 2020

(SC18M018)

Acknowledgements

I would first like to express my deep gratitude to my supervisor Dr. Jessy Jose for her continuous guidance and support. she has always been extremely motivating throughout the course of my work, and urged me to explore and find answers right from fundamentals.

I am grateful to Dr. Anandmayee Tej, Professor for her constant guidance and help which made it convenient and easy to work on my project. All of their valuable suggestions and insightful discussions have helped me a lot. Her care, patience and guidance are invaluable. I am really grateful to her for her selfless support *manufacturing* my thesis from the scratch. I have learned a lot from her and I hope I would be able to follow her teachings in my life.

I am sincerely thankful to Dr. Jagadheep D., Dr. Anand Narayanan, Dr. Samir Mandal, Dr. Sarita Vig, Dr. Resmi Lekshmi alongwith Dr. Anandmayee Tej, who were my very first professors and mentors in Astronomy and Astrophysics at IIST. They introduced me to this fascinating discipline in the most beautiful way possible, and rooted my interests firmly into Astronomy. They were always available for discussions and help. I am grateful to Sai ‘chetta’ Krishnan, our Lab Assistant, who was ever ready to provide all the technical help.

I would like to acknowledge the help of Dr. Swagat Ranjan Das, IISER Tirupati for his help on NN map. I big heart-full thanks to Ajay Potdar for his decisive help in generating various maps using Gildas. I do owe him big times and hope I can stand for him in his need of support in coming future. A big thanks to Bhavana D. for her generous help and suggestions regarding SED modelling and VOSA. I vividly remember the time when I was going through some difficult period with a journal paper published by a renowned author from a larger than life University. It was Vipin Kumar, who stood besides me at that time and supported me with his efforts to provide decisive confirmation regarding my hypothesis. I would also like to thank Deepak Chahal and Anindya Saha, who were really instrumental in this project. I am sure I would miss afternoon lemonade with these two. Thank you Manish, Kiran, Pratyush and Mathin for being wonder-full batch-mates.

Finally, I must express my profound gratitude to my loving parents, especially my *papa*, who is responsible for planting the seed of ‘crave for Physics’ in me. Its hard to even

think about finding words to thank my *maa*, it's indeed an undeniable fact that *Kuputro Jayet, Kwachidapy Kumata Na Bhawati*. Finally to my dear brother for providing me with unfailing support and continuous encouragement throughout my years of study. Today whatever I have done, whatever I will do tomorrow, whatever I will become, its all because of my Guru, my God and my Guardians.

Divyansh Chourey

Abstract

Bright-rimmed clouds (BRCs) are small molecular clouds found near the edges of evolved H II regions, with the bright rims facing the ionizing stars. The morphology and physical orientation of BRCs match well with the theoretical models of Radiation driven implosion (RDI), so they are generally believed to be the sites of RDI.

This project is about study of ongoing star formation activity in such BRCs. We have started with studying W5E H II region, which harbours two BRCs, BRC 13 and BRC 14. The data analysis of two BRCs involves multi-wavelength photometric study. For optical, PanSTARRS PS1 catalog is used. In NIR and MIR, NEWFIRM and Spitzer PBCD images are used to perform photometry. The combined catalog from optical, NIR, MIR for this region is used for identification of young stellar objects (YSOs) and modelling of spectral energy distribution (SEDs). Results from SED modelling are used to estimate various parameters like luminosity, mean age, T_{eff} etc. Using all these physical parameters, star formation rate and star formation efficiency is estimated for the two BRCs.

Contents

List of Figures	xiii
List of Tables	xxi
1 Introduction	1
1.1 Effects of Massive star on interstellar medium	1
1.1.1 H II Regions	2
1.1.2 H II region expansion: Phase I	3
1.1.3 H II region expansion: Phase II	4
1.2 Feedback Driven Regions	5
1.3 Triggered Star Formation	9
1.3.1 Collect and Collapse	10
1.3.2 Radiation Driven Implosion	13
1.4 Bright Rimmed Clouds	19
1.4.1 Star Formation in Bright Rimmed Clouds	21
1.5 Motivation, Region of Study and Thesis Outline	22
2 Methodology	25
2.0.1 Aperture Photometry	25
2.0.2 Point spread function (PSF) Photometry	27
2.1 Extinction Estimation Methods	30
2.1.1 Column Density Map	30
2.1.2 PNICER	31
2.1.3 Using NIR and MIR photometry	35
2.2 Classification of Young Stellar Objects	37
2.3 YSO Identification	38
2.3.1 YSO identification:Phase I	39

2.3.2	YSO identification: Phase II	41
2.3.3	YSO identification: Phase III	42
2.4	Spectral Energy Distribution (SED) Modelling	42
2.4.1	Theoretical SED Models	42
2.4.2	VOSA SED Analyzer	45
3	Multi-Wavelength Data and Reduction Procedure	53
3.1	Optical data form PanSTARRS	54
3.1.1	Source Selection	54
3.2	Near Infrared Data	55
3.2.1	NEWFIRM data	55
3.2.2	Source Detection	55
3.2.3	Aperture Photometry	56
3.2.4	PSF Photometry	56
3.2.5	Source Association	58
3.2.6	Calibration and Catalog Merger	58
3.3	Mid-Infrared Data Reduction	62
3.3.1	MIR Source Detection	62
3.3.2	Aperture Photometry	62
3.3.3	PSF Photometry	63
3.3.4	MIR Source Association	64
3.3.5	Calibration and Catalog merger	64
3.4	Combined Optical, NIR and MIR catalog	64
4	Analysis and Results	67
4.1	Magnitude distributions and completeness limit	68
4.2	Extinction Estimation	71
4.2.1	Using Column Density Map	71
4.2.2	Using NIR and MIR photometry	72
4.2.3	Using Field Stars	74
4.2.4	Using PNICER	75
4.3	Class I and II YSO identification	77
4.4	SED Modelling and the HR diagram	79
4.5	Identification of Class III sources	83
4.6	Spatial coverage of BRCs from the stellar density map	87
4.7	Mass estimation and Initial Mass Function (IMF)	89

4.8	Star formation rate and star formation efficiency	90
4.8.1	Estimation of SFE	91
4.8.2	Estimation of SFR	92
4.9	Discussion	92
5	Conclusion	97
	Bibliography	98

List of Figures

1.1	Schematic of H II region. This shows a central ionizing star within a spherically symmetric cloud. The ionization front is trailing to shock front. This shows the collected neutral material and cold dust at the outskirts of H II region. It shows the hot ionized gas and hot dust within the Strömgren radius (Deharveng et al. 2010)	3
1.2	Schematic view of a H II region showing its second phase of expansion along with different mechanism of triggered star formation: (1) Small-scale gravitational instabilities; (2) Large-scale gravitational instabilities resulting in the formation of high-mass protostellar cores; (3) Ionizing radiation imploding on a turbulent ambient medium; (4) Radiation-driven implosion of pre-existing dense clumps (Deharveng et al. 2010).	9
1.3	Column density maps from three different phases of CC process. Left hand column is for smooth simulation and right hand column is for noisy simulation (see text for details) (Dale et al. 2007).	12
1.4	Time sequence of column-density images showing the evolution of the simulated cloud when it is exposed to a relatively high ionizing flux. t/Myr is given in the top right-hand corner of figure. The color bar shows the values of column density in log scale and axes are in parsec Lefloch & Lazareff (1994).	14
1.5	Time evolution of bright rimmed cloud. Three-dimensional projection of bright rimmed cloud is shown in left side. Right side column shows the evolution, color-coded (Ionized gas in blue, neutral gas in red) with column density, contour shows the ionization fraction (Kessel-Deynet & Burkert 2003).	16

1.6 Dense cloud along the symmetry axis is shown (Only the top half portion). An ionization-shock front propagates into this initially spherical cloud. The ionizing photon flux at (r_0, θ_0) depends on the absorption along the dashed line toward the ionizing star (Bertoldi 1989).	18
1.7 Classification of the rim shape (Sugitani et al. 1991). Relation between width (W) and length (L) for all three types of BRCs shown above are given in Table 1.2.	20
1.8 Region of giant molecular complex W5. Color composite image shows two HII regions, W5E and W5W in radio 1.42 GHz (red), Spitzer IRAC 8.0 μm (cyan). The yellow plus sign shows the position of ionizing source (Deharveng et al. 2012).	23
1.9 Color-composite image of W5E HII region with 250 μm Herschel-SPIRE (red), 100 μm Herschel-PACS (green), DSS2 survey (blue). The yellow cross shows HD18326 which is a ionizing star cluster for W5E HII region (Deharveng et al. 2012).	24
2.1 Point source photometry showing the aperture radius with the inner and out sky radius to measure background sky value.	25
2.2 Example of PSF model fitted using analytic function MOFFAT on linear scale (a) and on two dimensional plane (b).	29
2.3 PSF photometry Flowchart	29
2.4 Plot generated by the PNICER showing the density distribution for the feature combinations. This plot is generated as an example for Orion A region.	32
2.5 CC plot generated by the PNICER showing the [J-H] / [H-K] distribution.	32
2.6 Plot generated by the PNICER showing the kernel density distribution map for the JHK _s combinations, Jmag (top), Hmag (middle) and Kmag (bottom). The color coding gives the normalized probability density function for extinction. The yellow pixels shows maximum extinction probability. This plot is generated as an example for Orion A region.	33
2.7 Plot generated by the PNICER showing the extinction map in V-band (top), the uncertainty map (middle) and stellar number density map (bottom). This plot is generated as an example for Orion A region.	34
2.8 Flow chart showing the photosphere modelling process.	43
2.9 Uncertainty grid showing the nine points to calculate the age and mass with their own uncertainty.	51

2.10	Interpolation is used to estimate the minimum distance from point P to get D1 and D2 from either side of the point to the respective isochrone.	51
3.1	Pan-STARR filter profiles.	54
3.2	NEWFIRM filter profiles	56
3.3	Magnitude versus error plots for NEWFIRM JHK photometry. The horizontal axis is magnitude in J band (top left), H band (top right) and K band (bottom). The vertical axis shows error in magnitude (merr).	57
3.4	Distribution of magnitude difference between NEWFIRM and 2MASS. The Gaussian fit is shown in red with mean and standard deviation is given at top of each panel.	59
3.5	Distribution of color difference between NEWFIRM and 2MASS. The Gaussian fit is also shown in red with mean and standard deviation mentioned at top of each panel.	60
3.6	Magnitude versus error Plots for JHK filter of merged 2MASS-NEWFIRM catalog. For $K < 13$ mag, 2MASS data is plotted.	61
3.7	IRAC band filter profiles	62
3.8	Magnitude versus error in magnitude plots for MIR IRAC bands. Channel 1 ($3.6 \mu\text{m}$) (top left), Channel 2 ($4.5 \mu\text{m}$) (top right), Channel 3 ($5.8 \mu\text{m}$) (bottom left) and Channel 4 ($8.0 \mu\text{m}$) (bottom right). Here, only sources with $\text{merr} < 0.20$ are shown.	63
3.9	Distribution of offset for each MIR filter. Channel 1 (3.6 micron) (top left), Channel 2 (4.5 micron) (top right), Channel 3 (5.8 micron) (bottom left) and Channel 4 (8.0 micron) (bottom right). Offset is calculated from Koenig et al. (2008).	65
4.1	NEWFIRM K-band image showing BRC 13 and BRC 14 in the W5E star formation complex. The cyan rectangle denotes the area ($\sim 265.15 \text{ arcmin}^2$) considered for analysis.	67
4.2	Histograms showing the magnitude distribution for the NEWFIRM NIR photometric data. (a) J band ($1.2 \mu\text{m}$), (b) H band ($1.6 \mu\text{m}$) and (c) K band ($2.2 \mu\text{m}$). The distribution is plotted for all sources within the box shown in Fig. 4.1.	68

4.3	Histograms showing the magnitude distribution for Spitzer-IRAC MIR photometric data. (a) CH1 (3.6 μ m) band, (b) CH2 (4.5 μ m) band, (c) CH3 (5.8 μ m) band and (d) CH4 (8.0 μ m). The distribution is plotted for all sources within the box shown in Fig. 4.1.	69
4.4	Histograms showing the magnitude distribution for PanSTARRS optical photometric data. (a) g (0.49 μ m) band, (b) r (0.62 μ m) band, (c) i (0.75 μ m) band, (d) z (0.87 μ m) band and (e) y (0.96 μ m) band. The distribution is plotted for all sources within the box shown in Fig. 4.1.	70
4.5	Extinction map prepared using column density map shown above using relation $N_{H_2} / A_V = 1.37 \times 10^{21} \text{ cm}^{-2} \text{ mag}^{-1}$	72
4.6	Histogram of estimated extinction based on the column density map for sources associated with BRC 13 and 14 and lying within the box shown in Fig. 4.1.	73
4.7	Histogram of estimated extinction based on the NIR and MIR photometry for sources associated with BRC 13 and 14 and lying within the box shown in Fig. 4.1	73
4.8	(a) CC diagram (J-H)/(H-K) for W5E HII from area shown in Fig. 4.1. The continuous curves shows the intrinsic locus of main sequence (below) and giants(above) (Bessell & Brett 1988). The dashed line represents the locus of intrinsic color of Classical T-Tauri (Meyer et al. 1997). The dashed-dotted lines are reddening vectors from (Cohen et al. 1981). Sources shown in green are field stars and Class III sources. (b) Extinction map of W5E HII region made by using the background field stars. The colorbar shows extinction in K-band i.e. A_K . The map has 265 arcmin ² field of view and resolution of 1 arcmin.	74
4.9	CC plot generated by PNICER. Horizontal axis is [J-H] color and vertical axis is [H-K] color. The data is taken from 2MASS Point Source Catalog.	75
4.10	Histogram showing the distribution of extinction values, A_V , estimated using the PNICER method for all those sources falling in green box in Fig. 4.1. The extinction values are taken from PNICER map shown in Fig. 4.11.	76
4.11	Extinction map generated by PNICER. The color bar shows the extinction values in V-band (A_V). The map shown has field of view of 0.5 deg ² with the resolution of 0.5 arcsec.	76

4.12 Extinction uncertainty map generated by PNICER. The color bar shows the extinction uncertainty values in V-band (σA_V) which is calculated from PNICER map. The map shown has field of view of 0.5 deg^2 with the resolution of 0.5 arcsec	77
4.13 CC diagram of $[\text{Ks} - \text{CH1}]_o$ versus $[\text{CH1} - \text{CH2}]_o$ showing the Class II (green) and Class I (blue) sources with field/Class III sources (red). The color cutoff are given in detail in section 2.3. The identification scheme is adopted from Gutermuth et al. (2005, 2009).	78
4.14 Spatial distribution of Class I/II sources identified in the region associated with BRC 13 and 14. Blue sources and red sources are Class II and Class I, respectively.	79
4.15 The HR diagram for YSOs (in black) identified in Section 4.3. The horizontal axis is temperature in K and vertical axis plots the bolometric luminosity (L/L_\odot) in log-scale. The red lines are the isochrones of 0.007 Myr (right most) till 10 Myr (left most). The blue dotted curves are the evolutionary tracks of mass $0.1 M_\odot$ (bottom most) to $30 M_\odot$ (top most). The isochrones and evolutionary tracks are taken from Siess et al. (2000).	80
4.16 Histograms showing the temperature distribution for Class I and II sources for BRC 13 and BRC 14 combined. Bin size used is 1000 K. Mean temperature is 4540 ± 150 K, minimum and maximum temperature is 2600 ± 100 K and 10000 ± 100 K, respectively.	81
4.17 Histograms showing luminosity distribution for Class I and II sources for BRC 13 and BRC 14 combined. Mean of $0.128 \pm 0.112 L_\odot$. The minimum and maximum luminosity values are $0.097 \pm 1.41 L_\odot$ and $1629.29 \pm 1.34 L_\odot$, respectively. Bin size is taken as $0.5 L_\odot$	81
4.18 Histograms showing age distribution in Myr for Class I and II sources for BRC 13 and BRC 14 combined. The minimum age and maximum age obtained are 0.112 ± 0.008 Myr and 4.455 ± 1.722 Myr respectively. Bin size is 0.5 Myr.	82
4.19 Histograms showing mass distribution for Class I and II sources for BRC 13 and BRC 14 combined. The minimum mass and maximum mass obtained are $0.107 \pm 0.001 M_\odot$ and $2.842 \pm 0.18 M_\odot$ respectively. Bin size for this plot is $0.25 M_\odot$	82

4.20 CMD plot showing [z-K] color on horizontal axis and z magnitude on vertical axis. This plot is foreground extinction corrected. The mean foreground extinction is assumed to be $A_V = 2.0$ mag. BRC sources falling inside the box shown in Fig. 4.1 are shown in red. Blue sources are the control field sources. The Class I/II sources identified in Section 4.3 are shown in green. Line shown in magenta is the empirical cutoff (eq. 4.1) to identify the initial set of likely YSOs.	83
4.21 (a) CMD z versus [z-K], sources identified in step 1 is shown in green. Straight magenta line is from eq. 4.1. (b) CMD plot showing [J-K] color on horizontal axis and J magnitude on vertical axis. This plot is foreground extinction corrected. The mean foreground extinction is assumed to be $A_V = 2.0$ mag. BRC sources falling inside the box shown in Fig. 4.1 are shown in red. Blue sources are the control field sources. The Class I/II/III sources identified by Fig. 4.20 are shown in green. Line shown in magenta is the empirical cutoff (eq. 4.2) to identify second set of YSOs. Red horizontal line is 90% completeness limit in J band.	85
4.22 (a) CMD plot showing final set of YSOs in green. These are all the sources lying rightward to the magenta line in Fig. 4.21(b). The straight line of eq. 4.2 is plotted as magenta line. Red line shows the 90% completeness limit of J band. (b) Spatial distribution of YSOs identified in step 2 and shown in (a) in green.	86
4.23 Stellar density map prepared with list of YSOs identified and shown in Fig. 4.22. The nearest neighbor method is used with $j = 16$. The contours plotted in white start from the 3σ threshold. The two identified contours are top right contour (for BRC 13) and bottom contour (for BRC14).	87
4.24 Spatial distribution of YSOs lying within the contours of Fig. 4.23. For BRC 13, top right contour is taken and for BRC 14 bottom contour is considered.	88
4.25 Mass-Magnitude relationship taken from Baraffe et al. (2015) for all sources with mass $< 1.40 M_{\odot}$ and from Siess et al. (2000) for mass $> 1.40 M_{\odot}$. The curve is for 2 Myr isochrone. The vertical axis is the J band magnitude and horizontal axis is showing mass in log scale.	89

4.26 IMF estimated from mass-magnitude relationship after removal of contaminants in each mass bin. The bin size in this plot is 0.2 dex. The green curve represents the log-normal distribution by Chabrier (2003) which is fitted for sources $M < 1.0 M_{\odot}$. The red dotted line is the power-law fitted for sources $M > 0.5 M_{\odot}$ (Salpeter 1955). The error bars shown are Poisson uncertainty. This IMF presented is for the combined region for BRC 13 and BRC 14.	90
4.27 Kennicut-Schmidt diagram. The blue line shows the Kennicutt-Schmidt law given by eq. 4.10 (Kennicutt Jr 1998). Horizontal axis shows the log of gas mass density and vertical axis shows the log of the SFR. Data from various other studies (Aleala et al. 2008; Marin et al. 2008; Lai et al. 2008; Harvey et al. 2007; Allen & Davis 2008) are also shown.	93
4.28 YSO density as a function of the SFE. Data from various other studies (Aleala et al. 2008; Marin et al. 2008; Lai et al. 2008; Harvey et al. 2007; Allen & Davis 2008) are also shown.	94
4.29 YSO density as a function of the SFR. Data from various other studies (Aleala et al. 2008; Marin et al. 2008; Lai et al. 2008; Harvey et al. 2007; Allen & Davis 2008) are also shown.	95
4.30 YSO density as a function of SFRD. Data from various other studies (Aleala et al. 2008; Marin et al. 2008; Lai et al. 2008; Harvey et al. 2007; Allen & Davis 2008) are also shown.	96

List of Tables

1.1	Classification of Ionization fronts (Spitzer Jr 2008)	10
1.2	Classification of BRCs (Sugitani et al. 1991)	20
2.1	YSO classification (Stahler & Palla 2008)	37
2.2	Some commonly used theoretical models with their parameter grid space . .	44
2.3	Sample VOSA input file	46
3.1	Mean Wavelength and Bandwidth for all twelve filters used for this project .	53
3.2	Pan-STARR PS1 5σ depth and seeing	55
3.3	Estimated magnitude offsets with respect to 2MASS photometry.	59
3.4	Offsets used for calibration	64
3.5	Sample Catalog of BRC 13 and BRC 14 for NIR (J, H, K), MIR(CH1, CH2, CH3, CH4), Pan-STARR (g,r,i,z,y)	66
4.1	Estimated completeness limits (90%) in the twelve photometric bands. . . .	71

Chapter 1

Introduction

Massive stars ($M \gtrsim 8M_{\odot}$) are of crucial importance. They drive the chemical and dynamical evolution of the galaxy. They enrich the galaxy with heavy elements by nucleosynthesis in course of their evolution. In addition, they have strong mechanical and radiative feedback on the surrounding ambient medium. The mechanism(s) via which they form are, however, less well understood compared to the low-mass regime. Tremendous progress, both theoretically as well as observationally, in the field of high-mass star formation has happened in the recent years (Tan et al. 2014). Multi-Wavelength observations are growing which would aid in understanding the various proposed theories. As massive stars have been shown to have strong impact on the parental molecular cloud, it is thus important to understand this interaction and the outcome of the same.

In this project, we have attempted to study feedback driven region known as *Bright-Rimmed Clouds* (BRCs). They are the small globular structures found at the outskirts of *H II regions* formed by massive star (or star cluster) located at its center. We probe the star formation activity in BRC regions, focusing mainly on the pre-main sequence (PMS) sources. This study involves multiwavelength photometry, identification of PMS stars and analysing their spectral energy distributions (SEDs).

1.1 Effects of Massive star on interstellar medium

Feedback provided by massive star(s) on ambient medium are profound. Observational manifestations of the interplay between the high mass stars and the surrounding interstellar medium (ISM) are important probes for studying the various evolutionary phases involved in their formation along with various types of feedback mechanisms. The very initial stages are marked by the presence of energetic jets with outflow events. Once the ‘switching-on’ (core hydrogen burning) happens, the outpouring of UV photons ionizes the surrounding

neutral medium resulting in formation of H II regions. H II regions formed by a new-born massive star (or star cluster) expands into the ambient ISM driven by various feedback mechanisms like thermal over pressure, radiation pressure, powerful stellar winds or combinations of all. The result of such feedback mechanisms is a ‘bubble’ which shows up as a dense shell of swept up dust and gas between the shock front and ionization front, surrounding the relatively low density cavity around the central star or star cluster.

1.1.1 H II Regions

Massive stars formed within the giant molecular cloud ionizes the surrounding neutral hydrogen in the cloud. Massive stars (with spectral type O and B) are known to generate photons having energy greater than ionization energy (13.6 eV) of neutral hydrogen atom. Stellar *Lyman continuum radiation*, due to hydrogen recombination, ionizes a spherical volume of neutral hydrogen gas around massive stars. These regions span few parsecs in radius. Recombination of electron and ionized hydrogen produces several spectral lines which include optical *Balmer series* of hydrogen. Apart from this, emission from such regions has been broadly seen in forbidden lines like N II, O II and others. In addition to this, continuum emission at infrared (IR) and radio frequencies, millimeter, submillimeter and hydrogen recombination lines in radio regime are also observed. An illustrative H II region is shown in Fig. 1.1, it shows the shock front and the ionization front with central ionizing star.

Although, ionization and recombination are continuous and concurrent processes, it is straightforward to compute the scale at which these two processes balance each other. This means the volumetric rate at which a gas parcel ionized by ionizing flux from the central cluster is equal to the recombination rate of free electrons and protons. Balancing these two quantities defines the *Strömgren radius*. This implies that for the whole sphere of gas, total ionization events in unit time will be same as the total recombination events. The expression for *Strömgren radius* (Dyson & Williams 1997; Stahler & Palla 2008) is given by;

$$R_{str} = \left(\frac{3 N_*}{4\pi \alpha'_{recom}(T) n_e^2} \right)^{1/3} \quad (1.1)$$

where, N_* is total number of Lyman continuum photons, n_e is number of e^- and α_{recom} is the *recombination coefficient* at temperature T.

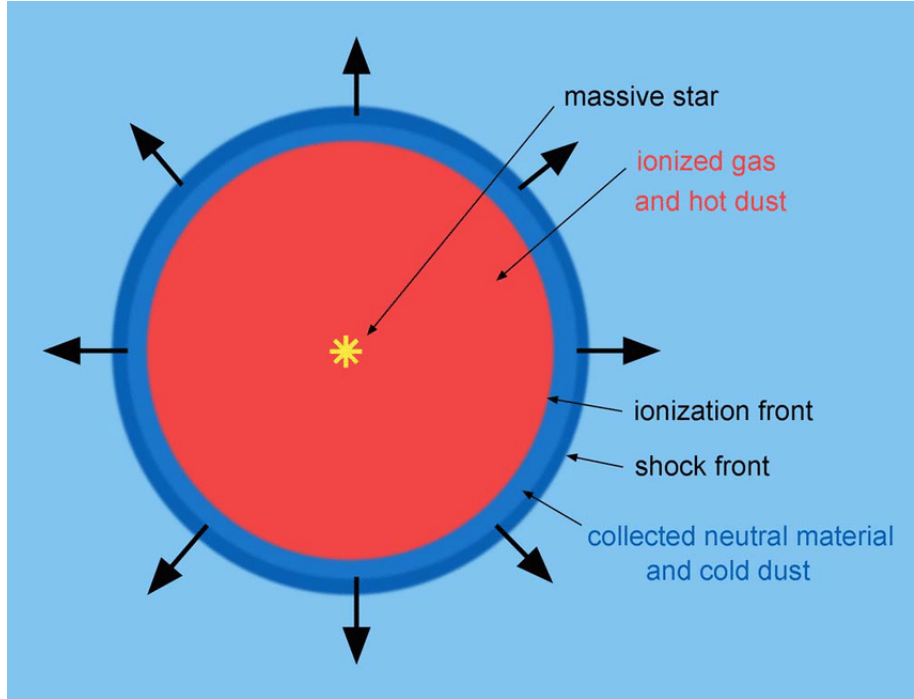


Figure 1.1: Schematic of H II region. This shows a central ionizing star within a spherically symmetric cloud. The ionization front is trailing to shock front. This shows the collected neutral material and cold dust at the outskirts of H II region. It shows the hot ionized gas and hot dust within the Strömgren radius (Deharveng et al. 2010).

1.1.2 H II region expansion: Phase I

The equation derived for the Strömgren radius shows that the region of ionization is a static entity. But this is a dynamical system, hence it has to expand with time. At the very beginning, consider no H II region exists around the massive star. Later, it expands rapidly to first, at the length scale of Strömgren radius, and then slowly afterwards. The moving front of the H II region, known as *ionization front*, though it has some finite width, is narrow enough compared to the scale of Strömgren radius hence it is treated as a sharp discontinuity. At the earliest stage, when the radius of the ionization front is negligible compared to Strömgren radius, the total rate of recombination inside the H II region is inadequate to match the rate of ionization by Lyman continuum radiation. Hence the left over photons reach the edge of the shell thus ionizing the gas beyond this. This explains the first phase of expansion and movement of ionization front radially outward. The equation governing this expansion is given by;

$$\lambda = [1 - e^{(-2\tau/3)}]^{1/3} \quad (1.2)$$

where, λ is the radial distance normalized to Strömgren radius and $\tau (\equiv t/t_{rec})$ is the time constant of this expansion such that $t_{rec} (\equiv \frac{1}{n_H^0 \alpha_{rec}})$ is the recombination time within the H II region (Spitzer Jr 2008; Stahler & Palla 2008).

Subsequently, the pressure gradient plays a key role in transferring the event from Phase I to Phase II. With temperature over 10^4 K, the inner part of the H II region has pressure three orders of magnitude compared to the outer region. As the length scale approaches the Strömgren radius ($\lambda \rightarrow 1$) and ionization front starts slowing down (eq. 1.2), pressure difference drive the second phase of expansion of H II region. In addition to this, the pressure gradient is so high that ionization front is left behind the shock front that expands into the cloud (see Fig. 1.1).

1.1.3 H II region expansion: Phase II

Decline in velocity of ionization front marks the commencement of the next phase of expansion. The value at which this turn over happens is the one at which the ionization front velocity declines to internal sound speed. During the early first phase expansion, the ionization front speed ($> 10^3 \text{ kms}^{-1}$) exceeds way more than sound speed ($\approx 11 \text{ kms}^{-1}$, in a ionized gas at temperature $\approx 10^4 \text{ K}$). It is known that the small pressure perturbation can propagate at the speed of sound in that medium, hence at initial first phase of expansion, these small pressure perturbation can not cross the ionization front. But as the second phase begins, the ionization front moves with velocity close to sound speed in that medium. During this time, the pressure perturbation from inside the H II region can cross the ionization front which leads to an expanding shock.

Material outside the ionization front is compressed to make a relatively thin and neutral shell surrounding the H II region. At this point the ionization and shock front moves almost at the same speed which later on declines below the sound speed of medium. This makes ionization front trail the shock front (see Fig. 1.1). Following is the equation the governs the second phase of expansion;

$$\lambda = \left[1 + \frac{7\tau'}{4} \right]^{4/7} \quad (1.3)$$

where, λ is the radial distance normalized to Strömgren radius and $\tau' (\equiv (\nu t)/R_s)$ is the time constant of this expansion such that ν is the speed of sound in the H II region and R_s is Strömgren radius (Dyson & Williams 1997; Spitzer Jr 2008; Stahler & Palla 2008).

1.2 Feedback Driven Regions

As discussed in the previous section, young massive stars have significant effects on their neighbouring regions. These stars affect the next generation of stars in many ways. In this section, we discuss some decisive feedback mechanisms provided by these massive young stars. They have different classification but broadly they are divided into three categories (Krumholz et al. 2014):

- **Momentum Driven Feedback:** *Momentum feedback* is the deposition of momentum on the neighboring star forming cloud. This action pushes the gas and stimulates turbulent motions within the gas parcel. If this feedback is sufficient enough, it can rip the neighboring medium apart entirely. Dense molecular clouds and lesser dense ISM are very good and efficient in radiative cooling such that when a young star intercepts energy into these clouds, the absorbed energy re-radiates away with time scale less than dynamical time scale of that cloud. Unlike the energy transfer, momentum transferred by the feedback affects the medium severely since it is not possible to dissipate the momentum like energy. This momentum transfer is provided in two ways:
 1. **Protostellar Outflow:** *Protostellar outflow* ejects large amount of mass into ambient region around young stars. Since outflows inject momentum and energy into surrounding medium, this feedback affects the environment in which the stars form (Norman & Silk 1980; McKee 1989). Protostellar outflow feedback becomes more severe in case where large number of stars form close to each other and almost in the same epoch. Low-mass protocluster NGC 1333 is a classic paradigmatic object for this type of feedback. In this case the molecular line data along with the IR observations shows various outflows activities in close proximity (Bally et al. 1996; Knee & Sandell 2000; Bally et al. 2008). Walawender et al. (2005) have studied NGC 1333 which is located to the west of the Perseus molecular cloud. The total molecular mass in the NGC 1333 core is estimated to be about $450 M_{\odot}$. They have investigated that the star cluster associated with NGC 1333 hosts about 150 young stars along with 30 groups of HH objects with many active outflow activities (Warin et al. 1996; Aspin et al. 1994; Greene & Lada 1996; Bally et al. 1996). Bally et al. (1996) has defined the same region as a *microburst of star formation* of interval estimated as less than 1 Myr within a cluster radius of less than 1 pc. Studies by Sandell & Knee

(2001) found that outflows has crucial role in the balancing of the energy budget in NGC 1333. NGC 1333 has a filamentary cloud structure which consist of several cavities, some of which can be traced to remnants of past outflow activity and some of the action of current outflows.

Study by Knee & Sandell (2000) also estimated the NGC 1333 outflow's energy and momentum injection rate as $\dot{P} \sim 10 M_{\odot} \text{ kms}^{-1}$ and $L \sim 0.1 L_{\odot}$. This study consider the mean age of an outflow to be 0.1 Myr which is taken from [(Bally et al. 1996)]. The amount of energy and momentum injection calculated by this study is sufficient to blow off the cloud considering its mean lifetime to be 10 Myr. Sandell & Knee (2001) illustrates that star formation activity could be triggered by density enhancement at the exterior of such cavities. This implies that star formation could be triggered by previous events of star formation and related outflow activity.

2. **Radiation Pressure:** The second form of momentum feedback is radiation pressure from massive stars. Radiation feedback mechanism involved deposition of momentum and energy from the massive stars to the surrounding medium. Except for photons above 13.6 eV, this transfer of energy and momentum is mostly carried by the dust grains. Only few observational studies have been carried out for the investigation of the effects of radiation pressure feedback. Scoville et al. (2001) studied the M51 region and indicated that radiation pressure from young clusters forming there exceeds their self-gravity.

Lopez et al. (2011, 2014); Pellegrini et al. (2011) have studied the giant H II region 30 Doradus in the LMC along with several other H II regions in the Magellanic Clouds to identify various effects of radiation pressure based feedback and the momentum transfer mechanisms.

The formation of OB stars in a cloud core region ceases at the limit when the radiation pressure on the surrounding dust exceeds the self-gravity of the core star cluster. This happens to be at a stellar luminosity-to-mass ratio of $\sim 500 - 1000 (L/M)_{\odot}$ which results for clusters around $> 750 M_{\odot}$ (Scoville et al. 2001). A hydrodynamic model with an initial R^{-2} density distribution in free-fall collapse certify that the core star cluster is expected to self-limit at $\sim 10^3 M_{\odot}$.

Radiation pressure at this given limit effectively terminates further dust and gas accretion to the central dense core. However, radiatively compressed shell will

then propagate towards the outskirts with velocities around few km/s which may possibly trigger a second wave of star formation out to a few parsec distance. Final mass estimated of core cluster was $881 M_{\odot}$ and the luminosity was $10^6 L_{\odot}$. The core accretion was fully terminated by radiation pressure within 0.1 Myr. After this, the radiatively compressed shell is estimated to move outward at around $2-6 \text{ kms}^{-1}$. Since the compressed shell is expected to show Rayleigh-Taylor and Jeans instability, the star formation activity may continue in the outward moving shell (Scoville et al. 2001).

- **Explosive Feedback:** *Explosive feedback* is seen when stars heats up the gas at very rapid rate. The gas has very high temperature, such that it is no longer able to cool itself down on cloud's dynamical timescale. In this case, fraction of the energy added to the cloud is not lost as radiation to the ambient ISM. Also feedback ensues when the hot, over-pressured dense gas parcel expands explosively and does sweep away the surrounding cold molecular material. This feedback has three types:

1. **Stellar Winds:** Massive stars of spectral type O and early B, having photospheric surface temperature above $2.5 \times 10^4 \text{ K}$ produce strong winds (Vink et al. 2000). Main sequence stars have this temperature at mass around $40 M_{\odot}$ or more. Stars with mass in these ranges have shorter Kelvin-Helmholtz timescale such that they reach the main-sequence while they are still accreting the material. (Hosokawa & Omukai 2009). This implies that stellar winds starts to impinge the surrounding medium of gas and dust at very early stage of their evolution. These stellar winds carry less momentum than radiation field (Kudritzki et al. 1999).

The radiation driven stellar wind shows a strong correlation between total mechanical momentum ($\dot{M}_{v_{\infty}}$) transferred to ambient ISM by stellar wind outflow and luminosity of mass loosing giant star (Castor et al. 1975a,b; Pauldrach et al. 1986; Kudritzki et al. 1989). The relation is given by;

$$\dot{M}_{v_{\infty}} \propto R_*^{-1/2} L^{1/\alpha_{eff}} \quad (1.4)$$

where, $\dot{M}_{v_{\infty}}$ is mass-loss rate, v_{∞} is terminal velocity of stellar wind and R_* is the stellar radius and α_{eff} is dimensionless number of the order of 2/3. It shows the power law exponent of the distribution function of line strengths of many spectral lines driving the stellar wind.

2. **Photo-ionization Feedback:** Massive stars with mass $> 10M_{\odot}$ are known to produce large amount of UV photons which ionizes the surrounding gas and dust medium, this creates a ionized bubble (see Section 1.1.1). Equilibrium between heating and cooling processes inside H II regions maintains constant temperatures of about $10^4 K$ and internal sound velocity of 10 km s^{-1} (Osterbrock & Ferland 2006; Spitzer Jr 2008). This influences the evolution of YSOs in nearby region. On smaller scales, photo-ionization is expected to quench the growth of OB stars. Many simulation based studies has been done to study feedback by photo-ionization (Krumholz et al. 2006; Dale et al. 2012, 2013).

Krumholz et al. (2006) presented semi-analytic dynamical models for giant molecular clouds evolving under the influence of H II regions formed by young massive star clusters. Here, they derive the equation of mass, radius and velocity dispersion of giant molecular cloud with given initial approximation of homologous motion of gas. They have also suggested that the predominant destruction mechanism for giant molecular clouds is dynamical unbinding by the momentum propagated by an expanding H II region. But in case of massive clouds, this unbinding event does not happen till the H II region has photo-ionized away about 90% of the giant molecular cloud's mass.

3. **Supernovae:** Supernovae are known as the most energetic source of feedback. Around 10^{51} ergs energy is injected into surrounding ambient medium as thermal energy as well as kinetic energy of particles much of which ends up as thermal energy in a hot phase with a long cooling time. This thermal energy has very long cooling span. Due to time-scale of the process, supernovae turns out to have a limited affect on the process of individual star cluster formation Krumholz & Matzner (2009); Fall et al. (2010). In fact the first supernovae did not occur until 4 Myr of the beginning of the commencement of star formation. However, Krumholz et al. (2014) emphasize that supernovae are unimportant in case of star clusters and does not apply on the larger scales of diffuse giant molecular clouds or galaxies.

- **Thermal Feedback:** Unlike the previous cases, Thermal feedback is the process by which gas parcel do not undergo large scale flows but it does alter the temperature of it. Non-ionizing radiation is known to be the main source of thermal feedback. In the star formation process, gravitational potential energy turns to thermal and kinetic energy during collapse of cloud. This process ends up with formation of stellar core.

After that it results in three types of thermal feedback:

- Radiation from the core
- Luminosity from accretion onto the star
- Luminosity from continued collapse of the cloud and disk accretion

1.3 Triggered Star Formation

When star formation activity is driven by external factors we have the process of *Triggered star formation*. This can be accomplished in many ways, either directly altering the density distribution of the cloud or by a propagating shock into cloud, which makes regions satisfy the Jeans criteria of collapse. These triggering events can be achieved with the feedback mechanisms explained in the previous section (Section 1.2). Based on the discussed feedback mechanism, two most popular triggering processes have been proposed, *Collect and Collapse (CC)* and *Radiation Driven Implosion (RDI)* which are discussed in this section.

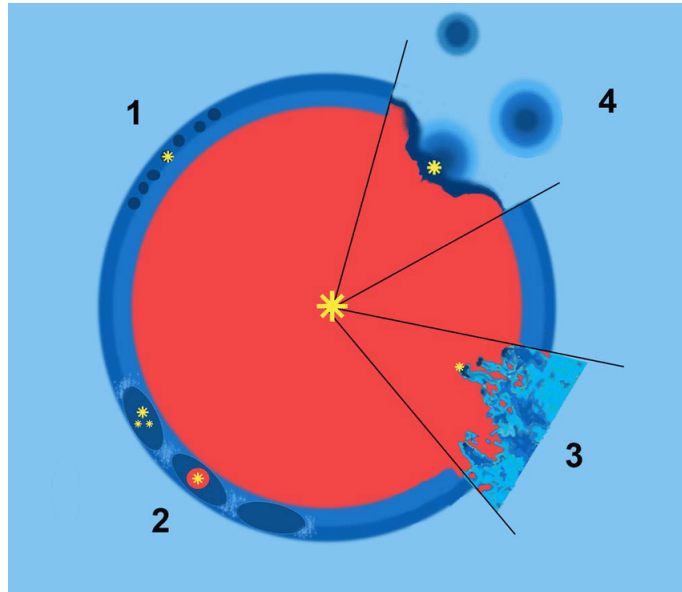


Figure 1.2: Schematic view of a H II region showing its second phase of expansion along with different mechanism of triggered star formation: (1) Small-scale gravitational instabilities; (2) Large-scale gravitational instabilities resulting in the formation of high-mass protostellar cores; (3) Ionizing radiation imploding on a turbulent ambient medium; (4) Radiation-driven implosion of pre-existing dense clumps (Deharveng et al. 2010).

1.3.1 Collect and Collapse

Collect and Collapse process is driven by massive stars that have formed inside a molecular cloud. This mechanism is known to be a large scale process taking place on relatively long span of time, as it takes time for a sufficient mass of gas to be swept up by the fronts and subsequently undergo collapse. The mass of the gas swept up by the fronts is large enough to form many stars. Collect and Collapse mechanism was first put forward by Elmegreen & Lada (1977). This is a simple model to explain induced star formation. Whitworth et al. (1994) has studied this in great detail. When ionizing source turns on inside a uniform gas distribution, the initial UV photon flux drives a spherical ionization front radially outward from the source. Velocity of the ionization front at this stage is much higher than the speed of sound in the cold neutral gas and the number of extra ionizing photons after ionizing the gaseous medium are still too large (see Section 1.1.2). This is referred to as the *R-type ionization front* (Kahn et al. 1954; Osterbrock 1974).

Table 1.1: Classification of Ionization fronts (Spitzer Jr 2008)

Ionization Front Type	Mach Number	Pressure	Density	Relative Velocity
Strong R	$M_1 > 1, M_2 < 1$	$P_2 > P_1$	$\rho_2 > \rho_1$	$v_2 < v_1$
Critical R	$M_1 > 1, M_2 = 1$	$P_2 > P_1$	$\rho_2 > \rho_1$	$v_2 < v_1$
Weak R	$M_1 > 1, M_2 > 1$	$P_2 > P_1$	$\rho_2 \geq \rho_1$	$v_2 \leq v_1$
Weak D	$M_1 < 1, M_2 < 1$	$P_2 \leq P_1$	$\rho_2 < \rho_1$	$v_2 > v_1$
Critical D	$M_1 < 1, M_2 = 1$	$P_2 < P_1$	$\rho_2 < \rho_1$	$v_2 > v_1$
Strong D	$M_1 < 1, M_2 > 1$	$P_2 < P_1$	$\rho_2 < \rho_1$	$v_2 > v_1$

As the region expands, the gas inside the R-type ionization front also increases, also it takes more and more photons to ionize the medium. This leads to decrease in speed of ionization front. As the speed of ionization front matches with the speed of sound of that medium, ionization front changes from R-type to *D-type ionization front* (at $\sim 10 \text{ kms}^{-1}$, for Hydrogen at 10^4 K) (see Section 1.1.3). This is at distance we know as Strömgren radius (sec. 1.1.1). The different properties of these ionization fronts are given in Table 1.1. Here M_1 and M_2 are the Mach number at the two sides of ionization front (subscript 1 corresponds to upstream and 2 corresponds to downstream) which is defined by the ratio of velocity of front to the sound speed in that medium (Newman & Axford 1968).

The expansion of an H II region through the surrounding neutral gas is highly supersonic and drives a shock front sweeping up an increasingly massive and dense shell of cool and neutral material (see Fig. 1.2). This is known as *Collect Phase*. In this phase ionization

front acts as a snowplough. If this process continues for long enough such that the density, mass and temperature of the shell reaches the point where Jeans instability is achieved. The shell starts to fragment and start a non-linear *Collapse Phase* which finally leads to triggered star formation.

1.3.1.1 Collect and Collapse: Simulation

Zavagno et al. (2006) suggest triggered star formation to be a result of collect and collapse process. Using SEST-SIMBA 1.2-mm continuum maps and ESO-NTT SOFI JHK_S images of RCW 79, they have identified five large massive fragments along the borders of H II region. Of these, two most massive fragments are found at diametrically opposite each other in shape of a ring. Their formation is presumably been triggered by the pressure gradient induced collapse of pre-existing molecular clumps. It is also possible that clumps might be resulting from dynamical instabilities in the collected layer. The large and massive fragments observed at the periphery of RCW 79 inferred to be mostly due to the the gravitational collapse of the layer of collected material by the ionization and shock fronts, according to the collect and collapse process.

This same study by citezavagno2006triggered has conducted simulations for CC process with particle hydrodynamics under the smoothed regime. They have simulated the evolution of a uniform and spherical molecular cloud given that ionizing source i.e. a massive young star is present at its centre. Simulations are done using the smoothed particle hydrodynamics (SPH) code. In addition, they have adopted a 3-D geometry. The cloud is assumed to be self-gravitating, however it is restricted from global collapse. Particles of this system can be considered as point masses called sink particles. As discussed by them, the shell of material driven by the shock front in the H II region fragments to form number of self-gravitating objects. This model calculates parameters at four numerical resolutions to confirm that the model is a converging one. Comparing their results to analytical model presented in Whitworth et al. (1994) shows that their simulations agrees in the same sense that the shell fragmentation predicts at the time and radius given by simulations in Whitworth et al. (1994), though with a given deviation of approximately 20-25 %. Most of the massive fragments predicted in this study have two highest resolution calculations and their masses are approximately half the mass of those predicted by Whitworth et al. (1994). The authors further stress that the results are robust against the presence of noise (randomness in the initial position of particles). in the gas and that the initial particle distribution has no significant effect on the evolution of the system (see Fig. 1.3). The conclusions of this study are robust and unaffected by effects of random noise or numerical resolution. In addition

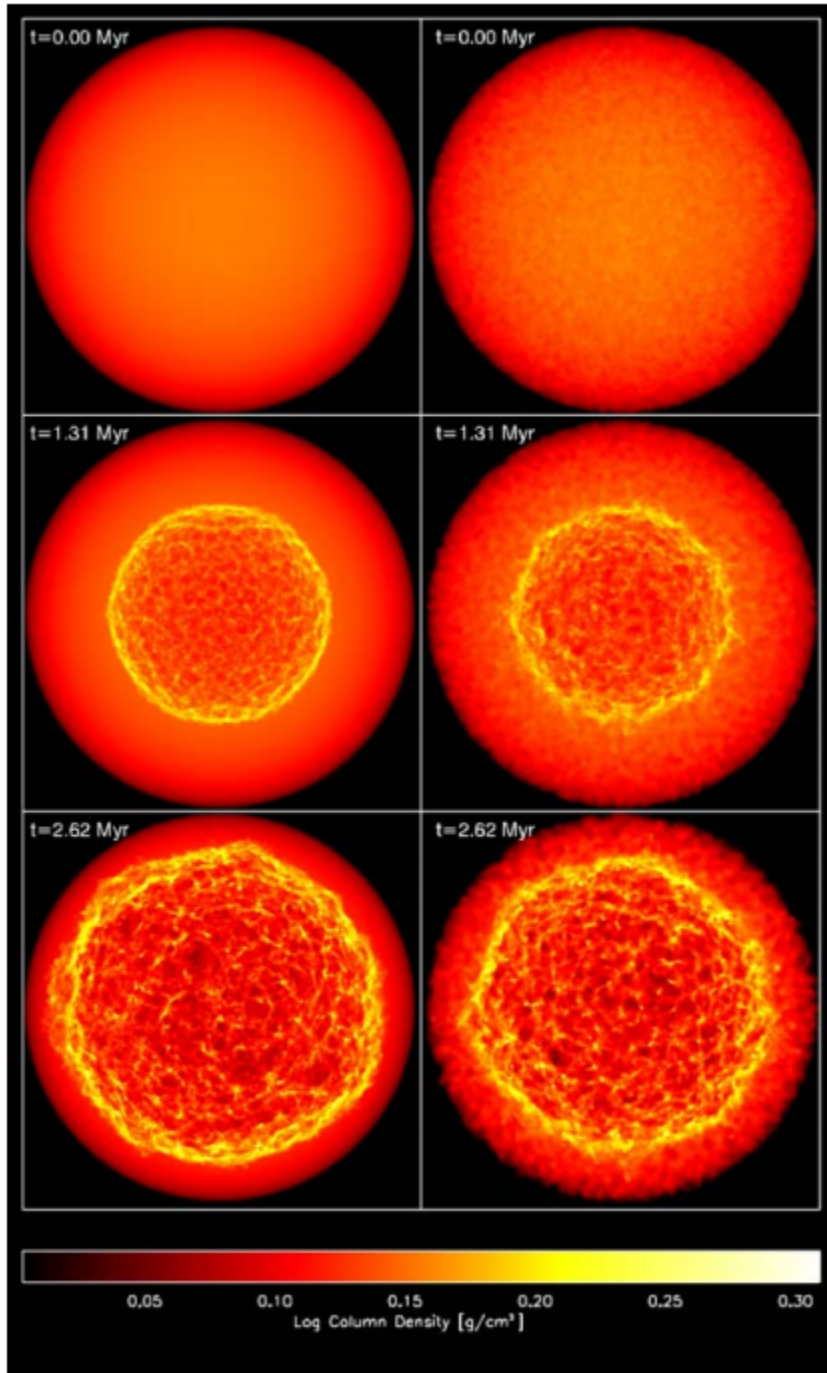


Figure 1.3: Column density maps from three different phases of CC process. Left hand column is for smooth simulation and right hand column is for noisy simulation (see text for details) (Dale et al. 2007).

to this, several other studies have been conducted to model the CC process with power-law radial density profiles (Tenorio-Tagle et al. 1986; Franco et al. 1990).

1.3.2 Radiation Driven Implosion

Considering the effect of diffuse UV radiation, the weak D-type ionization fronts are expected to be stable against the growth of ionization front up to the length scales larger than 0.2 pc. This UV radiation is primarily caused by recombination to the ground state of hydrogen atoms. These weak D-type ionization fronts span a considerable portion of the evolution of H II regions. This implies that hydro-dynamical instability can not explain the formation of structures like elephant trunks, cometary globules, bright rimmed cloud, etc. (Spitzer Jr 1954; Pottasch et al. 1956; Axford 1964). Radio observations shows the presence of clumps (and fragmented structures) at periphery of molecular clouds, as elephant trunks or BRCs which are usually regarded as remnant cloud clumps left in expansion process of HII regions (Ogura 2010).

Unlike the collect and collapse model of triggered star formation, RDI involves the photo-ionization of a pre-existing neutral, dense cloud located at the periphery of a H II region (see Fig. 1.2). This involves the exposure of neutral dense cloud to the ionization and shock fronts, which leads to the photo-ionization process of these clouds. To understand the RDI process, we need to first look at the underlying physics of the photo-evaporation process (see 1.3.2.2).

1.3.2.1 Radiation driven implosion: Simulations

Numerical calculations and simulations of the evolution of such clouds has been carried out by Lefloch & Lazareff (1994). This study involves dynamical evolution of a neutral hydrogen cloud exposed to the ionizing radiation of young OB stars. Results of this 2-dimensional hydro-dynamical simulation present a detailed evolutionary process from the beginning i.e. from cloud's collapse to the quasi-stationary phase of cometary evolution. The simulation result is shown in Fig. 1.4, showing the time sequence of column-density of a cloud which is exposed to high ionizing flux. From the results of the simulations, they have generated maps of projected density, emission measure and position-velocity diagrams. These authors suggest that the second phase goes on for approximately 90 % of the cloud's lifetime. The maps of emission measure exhibit a striking resemblance to various bright-rimmed structures different kinds of cometary globules found in HII regions. Simulation shows that they are stable and supported by the magnetic fields. In addition to

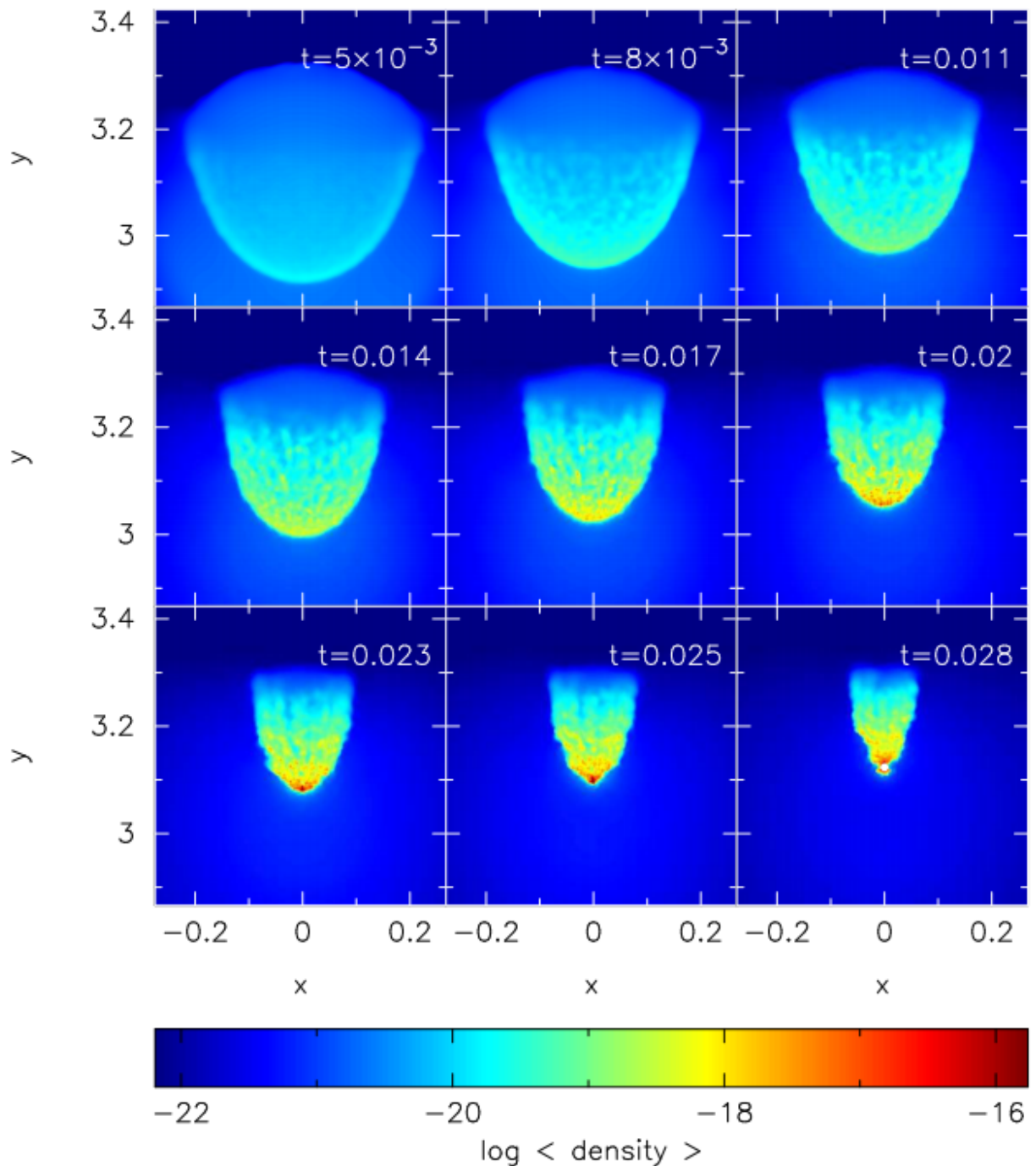


Figure 1.4: Time sequence of column-density images showing the evolution of the simulated cloud when it is exposed to a relatively high ionizing flux. t/Myr is given in the top right-hand corner of figure. The color bar shows the values of column density in log scale and axes are in parsec Lefloch & Lazareff (1994).

this, this study also checks the gravitational stability of such cometary structures. They also derive the condition for the stability of the ionization and shock fronts in the cometary phase and presented it with results from the simulations.

Based on their simulations, Lefloch & Lazareff (1994) show that the evolution can be divided into three phases;

1. Cloud undergoes a short collapse phase ($\sim 10^5$ yr) with maximum compression.
2. Cloud bounces in the temporary phase of re-expansions and re-compression.
3. Cloud settles into a long-lived cometary phase ($\sim 10^6$ yr)

Kessel-Deynet & Burkert (2003) also present three-dimensional simulation and calculations of molecular clouds exposed to radiation driven implosion. This simulation involves self-gravity and ionization through diffuse UV radiation. It demonstrate that radiation driven implosion could be an efficient process for injecting disordered kinetic energy into neutral isolated clouds in the neighbourhood of massive stars. Results shows that the effects of density perturbations of globules. It also shows that the beginning of gravitational collapse can be halted for a various of the implosion time-scales. The simulation from their study is shown in Fig. 1.5

Following are the four different phases that one can identify from Fig. 1.5:

1. After the ionizing source starts propagating, a weak R-type ionization front is propagated supersonic velocity towards the outskirts of the ambient H II region. The denser region of the cloud is shoveled and encircled by ionized gas after ~ 1.5 kyr. The ionization front stalls and slows down to velocity of sound in that medium. It is converted from weak R-type ionization front into a weak D-type front, (Fig. 1.5, top panels).
2. In next phase, shock front drives out of the cloud because of pressure imbalance with velocity $\sim 5 \text{ kms}^{-1}$ which is approximately equal to sound speed in that medium. The shock front sweeps a thin layer of dense cloud shocked material (Fig. 1.5, middle panels). Simulation starts converging to a finger-like structure referred to as a ‘globule’. Given that the structure depends on curvature of the ionization front once it enters the globule, hence the cloud shape and its curvature is primarily determined by the properties of ionization front.

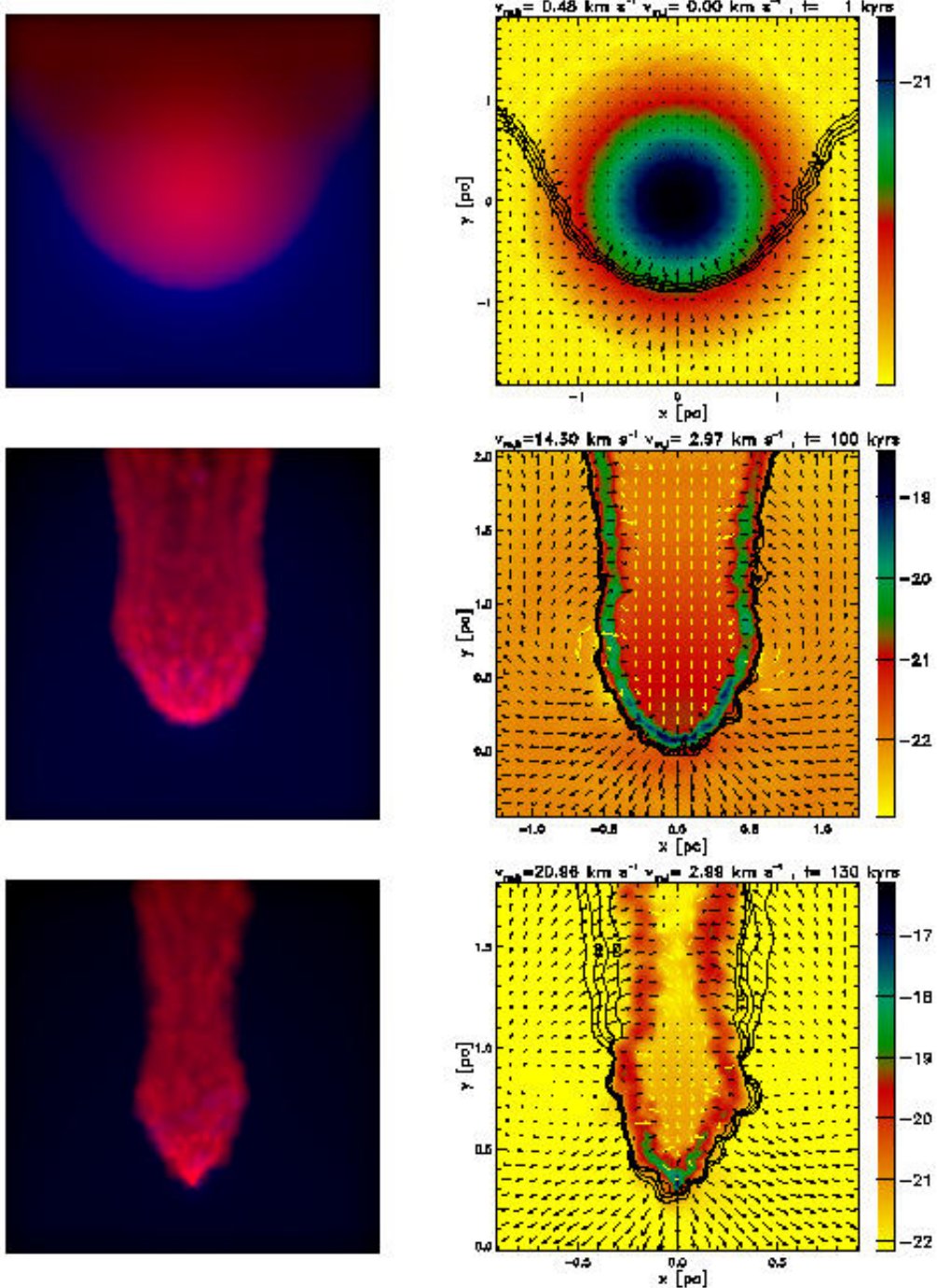


Figure 1.5: Time evolution of bright rimmed cloud. Three-dimensional projection of bright rimmed cloud is shown in left side. Right side column shows the evolution, color-coded (Ionized gas in blue, neutral gas in red) with column density, contour shows the ionization fraction (Kessel-Deynet & Burkert 2003).

3. The globule reaches a stage of maximum compression in about 130 Myr (Fig. 1.5, bottom panels). Considering the intense surge in pressure, the globule starts to expand again.
4. Subsequently, the structure enters the final phase, in which gas is ionized off the surface that continuously faces the ionizing source. This is how the bright rimmed cloud takes its shape.

Results shows that the cloud will have mass loss of $10^{-4} M_{\odot} \text{yr}^{-1}$. Further, velocity of gas at the ionization front is estimated to be around 13 km s^{-1} . This causes a *rocket effect*, which accelerates the material towards the direction of photon flow i.e. towards the ionization source (see arrow in Fig. 1.5). This makes the structure in which the gas spreads within the globule into a lid-shaped morphology which faces the ionization source. After about ~ 600 kyr, dynamical instabilities disintegrates the cloud partially leaving behind the remaining fragments, which are after some tens of kilo years, ionized completely and shaped into various structure that we observe like BRCs, pillars etc.

In addition to these studies, there are several numerical simulations carried out to understand the radiation driven implosion and how it shapes different types of structure like BRCs, pillars, trunks etc. All these numerical simulations show somewhat similar results with minor differences (Pavlakis et al. 2001; Miao et al. 2006, 2009; Gritschneder et al. 2009; Henney et al. 2009; Bisbas et al. 2011).

Bright rimmed clouds, cometary globules, pillars, elephant trunks etc. are found in H II region and they are believed to be the result of radiation driven implosion into the neutral, dense cloud at the outskirts of expanding H II regions. They are classified according to their appearance (Wasserburg et al. 1985). They are found to have typical mass of about $0.3 - 100 M_{\odot}$, size of ~ 0.1 pc and density about $10^5 - 10^6 \text{ cm}^{-3}$. Their origin is attributed to *Rayleigh-Taylor instability* at the periphery of expanding H II regions and it was first proposed by Spitzer Jr (1954). This will be discussed in more detail in later section.

1.3.2.2 Photo-evaporation of Interstellar Cloud with Radiation Driven Implosion

In Fig. 1.6, a spherically symmetric cloud of neutral hydrogen is shown. The direction of ionizing photon flux is shown by arrows. The ionization front is shown at distance r_0 from the center of the cloud. The velocity of the ionization front depends on the density of the medium normal to the direction to the star. The total ionizing flux reaching the I-front at some angle θ_0 is equal to the incident flux, F_i diminished by the number of recombination to excited levels of hydrogen in a column of unit cross section extending from the ionizing

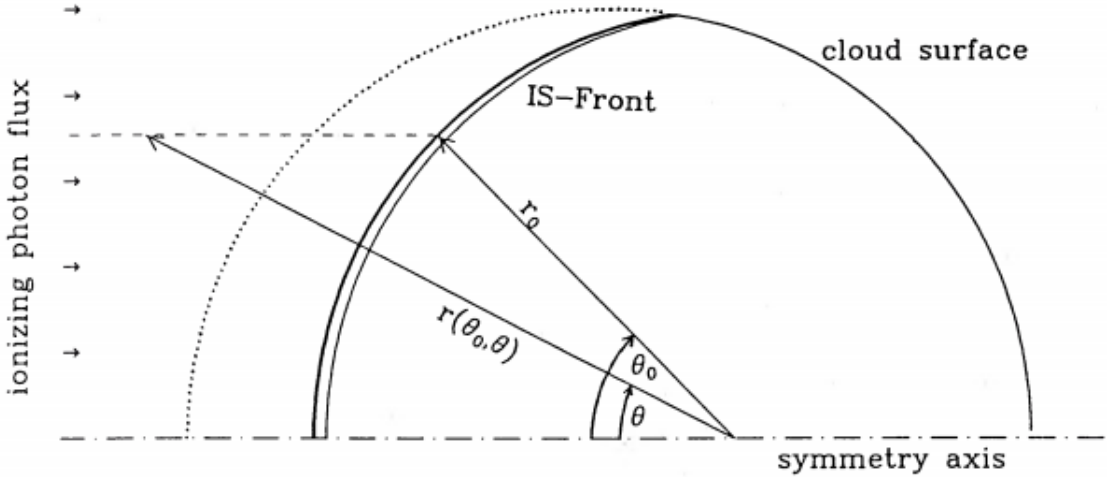


Figure 1.6: Dense cloud along the symmetry axis is shown (Only the top half portion). An ionization-shock front propagates into this initially spherical cloud. The ionizing photon flux at (r_0, θ_0) depends on the absorption along the dashed line toward the ionizing star (Bertoldi 1989).

source to the point on the surface shown. The later is specified by the radius of curvature of the front and the azimuthal angle from the axis (r_0, θ_0) . The ionizing flux reaching the I-front at θ_0 is then given by;

$$F(r_0, \theta_0) = F_i - \int \alpha_{recomb} n_e^2 ds \quad (1.5)$$

where the integration is carried out along the line connecting (r_0, θ_0) with the ionizing star. The Lyman continuum flux at a distance R_0 from the ionizing source is given by;

$$F_i = \frac{S}{4\pi R_0^2} = 8.36 \times 10^{10} \frac{S_{49}}{R_{0,pc}^2} s^{-1} cm^{-2} \quad (1.6)$$

where S is the central ionizing star's emission rate of photons beyond Lyman limit.

Consider the point on the cloud surface closest to the star, the Lyman continuum flux here is such that conditions are M-type, i.e. ionization front drives a shock into neutral gas, compressing it to such pressure that ionization front is approximately D-critical. The initial shock velocity at the symmetry axis, V_0 can be calculated by equating the shock ram pressure $\rho_0 V_0^2$ to the total pressure at D-critical point such that;

$$v \equiv \frac{V_0}{c_i} = \left(\frac{2F_i}{n_0 c_i} \right)^{1/2} = 12.1 \left(\frac{S_{49}}{n_{0,3} R_{0,pc}^2} \right)^{1/2} \quad (1.7)$$

Notice that the velocity of shock front is inversely proportional to number density of the cloud (Bertoldi 1989). In Fig. 1.6, the velocity of the shock front will be different at different geometrical positions of the cloud. This implies that velocity of the portion of shock front which propagates along the symmetry axis will trail the shock front which propagates along the direction offset to symmetry axis as shown in Fig. 1.6. This explains the basic formation mechanism for BRCs and how they take their peculiar shape. Since the incoming flux plays a key role in shaping the BRCs, hence the orientation of such structures is found facing towards the central ionizing cluster of that H II region. It can also be inferred from it that the shape and size of BRCs depends on the incoming ionizing flux, the distance of initial cloud from the central cluster, the initial density of such cloud and the ambient magnetic field in that region.

1.4 Bright Rimmed Clouds

We have discussed the formation mechanism and the evolution of bright rimmed cloud in detail in Section 1.3. The evolution of a neutral dense cloud of hydrogen to an ionized, cometary shaped structure is a long process and takes several kyr. Further, the Rayleigh-Taylor instability and Jeans instability criteria needs to be satisfied before star formation process can begin. Several studies have addressed various aspects of formation and evolution of Bright Rimmed Clouds in detail. Pioneering work by Oort, Spitzer and Kahn on the structure and evolution of steady photo-evaporation gas flow off spherical ionization front helped in understanding the physical processes in these regions (Oort et al. 1955; Kahn et al. 1954; Kahn 1958, 1969). The first complete theory of photo-evaporation of interstellar clouds was put forward in Bertoldi (1989); Bertoldi & McKee (1990). In addition, Wasserburg et al. (1985) classified the observed clumps in these regions according to their appearance. Their shape is typically spherical or elongated and directed away from the main ionizing source. We have seen in section 1.3.2 that the bright rims are seen on the cloud's side facing the ionizing source (Pottasch et al. 1956, 1958; Pottasch 1958). The dense shells surrounding H II regions as well as the neutral globules have been cited as possible centers for star formation (Elmegreen & Lada 1977; Sandford et al. 1982). Understanding the evolution of neutral condensations is the key to answering the question, whether star formation can be triggered by the dynamical effects of O and B stars. Based on the detailed model that we have discussed in section 1.3.2.1, calculations of the RDI process have been carried out by several authors (Bertoldi 1989; Lefloch & Lazareff 1995; Kessel-Deynet & Burkert 2003; Miao et al. 2006). BRCs are considered as the sites of RDI.

BRCs are known to be associated with HH objects and IRAS sources, which is indicative of ongoing star formation.

BRCs are classified into three types according to their rim morphology: (1) Type A, moderately curved rim; (2) Type B, tightly curved rim; and (3) Type C, cometary rim. The rim sizes, length (L), and width (W), are defined in Fig. 1.7. Type A should have a length to width ratio, L/W , less than 0.5, and type B greater than 0.5. The range of their sizes is 0.2-3 pc and most of them are less than 1 pc. The average lengths and widths of these three types of rims are given in Table 1.2 (Sugitani et al. 1991).

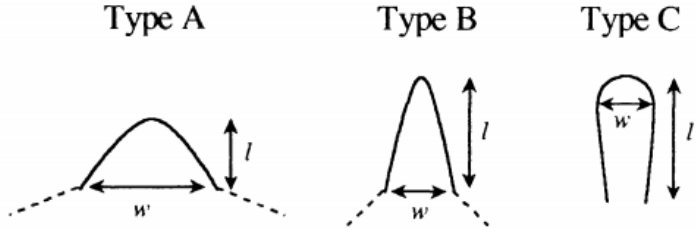


Figure 1.7: Classification of the rim shape (Sugitani et al. 1991). Relation between width (W) and length (L) for all three types of BRCs shown above are given in Table 1.2.

Table 1.2: Classification of BRCs (Sugitani et al. 1991)

Morphology	Length (L)	Width (W)	X (L/W)	Feature
A	0.39	1.0	$X < 0.50$	Moderately Curved Rim
B	1.0	1.20	$0.5 < X < 1.0$	Tightly Curved Rim
C	0.58	0.18	$X > 1.0$	Cometary Rim

Three well known sites of radiation driven implosion were reported by Sugitani (1989). In a later study, using Palomar sky survey, the same group has considered 44 BRCs which are associated with IRAS sources which were also considered as excellent sites for triggered star formation induced by RDI (Sugitani et al. 1991). Out of these, about 9 BRCs are seen to be associated with the molecular outflow activity and two are associated with HH objects. Sizes of most of the BRCs were found to be within 1 pc which is comparable to Bok globules. The luminosity of these associated IRAS sources are relatively large, about 10 to 10,000 L_{\odot} . IRAS luminosity to cloud mass ratios found to be more than those in dark globules or in dense cores in dark cloud complexes. These 44 BRCs are now cataloged as the *SFO catalog*. Since these sources belong to the northern hemisphere, this forms the first part of the catalog. Next part of the same catalog involves regions from southern

hemisphere. BRCs are known to be associated with IRAS sources, these are most probable protostar or YSO, forty-five BRCs associated with IRAS point sources selected from ESO (R) Atlas (Atlas is a 4500 square degree survey done by La Silla Paranal Observatory in u,g,r,i,z filters). Four of them are associated with HH objects and three sources with molecular outflows. Sources in this catalog also have sizes less than 1 pc. The luminosity of the associated IRAS sources are approximately $20L_{\odot} - 3 \times 10^4 L_{\odot}$. About 80% of the BRCs have radii of <0.5 pc. Forty percent of the clouds found to have small masses of $< 100 M_{\odot}$. About 40% of the associated IRAS sources have spectral energy distributions of the type I and about 30% have spectral energy distributions of the type II (For classification of YSOs based on SED see sec. 2.2). In addition, a molecular outflow survey of the northern BRCs have been carried out by the same group with the KOSMA (Kolner Observatorium for Submillimeter Astronomy) 3 m telescope in order to look for evidence of molecular outflows with CO(J=2-1) and CO(J=3-2) transitions.

1.4.1 Star Formation in Bright Rimmed Clouds

Detailed study by Sugitani et al. (1991); Sugitani & Ogura (1994) show that the BRCs are potential sites for probing radiation driven implosion and triggered star formation activity. The detection of large number of associated young stellar objects imply BRCs as active star forming regions. Sugitani et al. (1991) have also shown that stars formed through RDI are expected to contribute $\sim 5\%$ of the total stellar mass in the Galaxy. It is also believed that a significant number of intermediate mass stars may be formed in BRCs around H II regions. Another study by Sugitani et al. (1995) used NIR observations of 44 BRCs to reveal elongated aggregates of YSOs around BRCs with older stars near ionizing sources.

Chauhan et al. (2011) have studied W5 H II region. It has three BRCs namely, BRC 13, BRC 14 and BRC NW. By considering photometric data from 2MASS, MIR-spitzer data, they have estimated the mass and the age of the YSOs in all the three BRCs. To identify the YSOs, they have used NIR color-color diagrams. The resultant mass distribution for both of the BRCs has been estimated along with the mean age of the YSOs inside and outside the rim of the BRCs. Mass of the YSOs have been estimated using $V/(V-I)$ color-magnitude diagram (CMD) as explained in Pandey et al. (2008); Chauhan et al. (2009). It is interesting to note that the cumulative mass function (CMF) of the these BRCs show a break in the slope at $\sim 0.8 M_{\odot}$. The slopes in the mass range $0.2 \leq M/M_{\odot} \leq 0.8$, for both the BRCs are almost same. A similar analysis has done by Panwar et al. (2014) for BRC 5, BRC 7 and BRC 39.

Several authors have also studied triggered star formation in different regions. Study by Karr & Martin (2003) shows example of interaction between massive young stars and surrounding interstellar medium. The target region of their study is W5 H II region. They have quantitatively shown that star formation rate (SFR) is higher towards the edges of H II regions. There are some studies on the structural analysis and star formation efficiencies in BRCs. Sharma et al. (2016) have done this observations on 8 BRCs by identifying YSOs of different classes. In addition to it, they have also obtained a linear relation between number of YSOs and density of cloud. Also they have found a higher star formation efficiency (SFE) which is defined as the percentage of neutral hydrogen gas mass converted into stellar mass. Recent investigation by Evans II et al. (2009) indicated that YSO clustering of higher surface density show higher SFE than lower surface density.

As discussed earlier, Sugitani & Ogura (1994) found that elongated small clusters or aggregates of YSOs aligned towards the direction of the ionizing star. These YSOs showed a tendency that ‘redder’ (relatively younger) stars tend to be located closer to the BRCs, and relatively ‘bluer’ (relatively older) stars are found outside/away the clouds, indicating an age gradient. This hypothesis is called *small-scale sequential star formation (S⁴F)*. If the BRCs is relatively large, the star formation might have propagated along the axis of the BRCs as the ionization front and shock front advances towards into the molecular cloud (Kessel-Deynet & Burkert 2003). One of such evidence is presented by Chauhan et al. (2011). This shows that the young sources with higher NIR-excess (larger A_V) with the age estimated shows a age gradient from center of the ionizing cluster towards the BRCs. This suggested that the process of radiation driven implosion in past begin from center of H II region towards the present location of BRCs.

1.5 Motivation, Region of Study and Thesis Outline

This project is part of a larger program to study BRCs in different H II complexes like W3, W4 and W5. The key motivation to attempt this project is to understand the star formation process at BRCs by estimating their star formation rate and star formation efficiency. We require a good statistical analysis of SFR and SFE to fully uncover the true science at BRCs. This would demand a large sample of BRCs. The whole W3, W4 and W5 complex hosts 14 BRCs in total. All these BRCs are active site for ongoing star formation. This statistical interpretation of SFR and SFE can give some idea about the difference in star formation activity in BRCs in contrast with other cloud core. The other motivation of this project is to look at the trend of initial mass function towards the brown dwarf limit ($M/M_\odot < 0.08$).

Since BRCs are excellent site for low mass star formation, we expect a large sample of point sources in this mass regime. The trend in initial mass function is poorly understood at lower mass limit because of insufficient depth in available surveys. Since we have used deep NIR images from a 4m class telescope of NEWFIRM, we expect to have sufficient statistics available at lower mass limit.

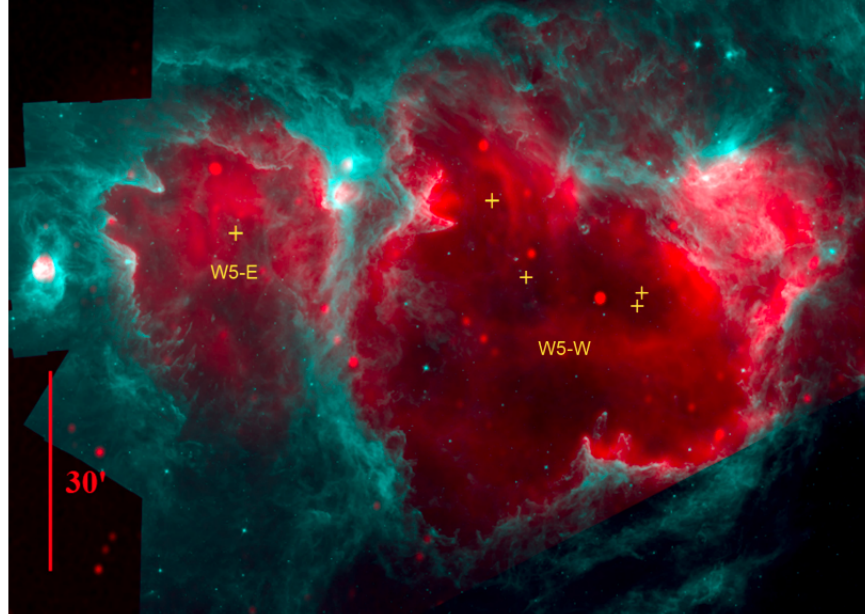


Figure 1.8: Region of giant molecular complex W5. Color composite image shows two HII regions, W5E and W5W in radio 1.42 GHz (red), Spitzer IRAC 8.0 μm (cyan). The yellow plus sign shows the position of ionizing source (Deharveng et al. 2012).

In the beginning of project, we have started with studying W5E H II region which includes two BRCs, BRC13 and BRC14 (see Fig. 1.8). W5E H II region is located in the Perseus arm of the Galaxy. The region is ionized by star cluster HD 18326. The cluster center turned out to be at $\alpha_{2000} = 02^h 59^m 22.0^s$; $\delta_{2000} = 60^\circ 34' 37''$. Distance of this region is close to 2.372 ± 0.231 Kpc. The spectral type of ionizing cluster members are B0 or earlier. BRC 13 shows type B morphology. Its head is symmetric with respect to the direction of its ionizing source HD 18326. This head spans over 1.7 pc (see Fig. 1.9). Using deep photometry in V, I band, Chauhan et al. (2011) has estimated ages of 24 point sources outside the rim of BRC 13 as 2.44 ± 1.37 Myr and 10 sources inside the rim BRC 14 as 1.61 ± 1.41 Myr. BRC 14 shows type A morphology, its head is also symmetric with respect to direction of HD 18326 suggesting radiation from central ionizing cluster has shaped both the BRCs. BRC 14 has head of length of about 1.0 pc (see Fig. 1.9). Chauhan et al. (2011) has also estimated ages for 18 sources inside BRC 14 rim as 1.01 ± 0.73 Myr

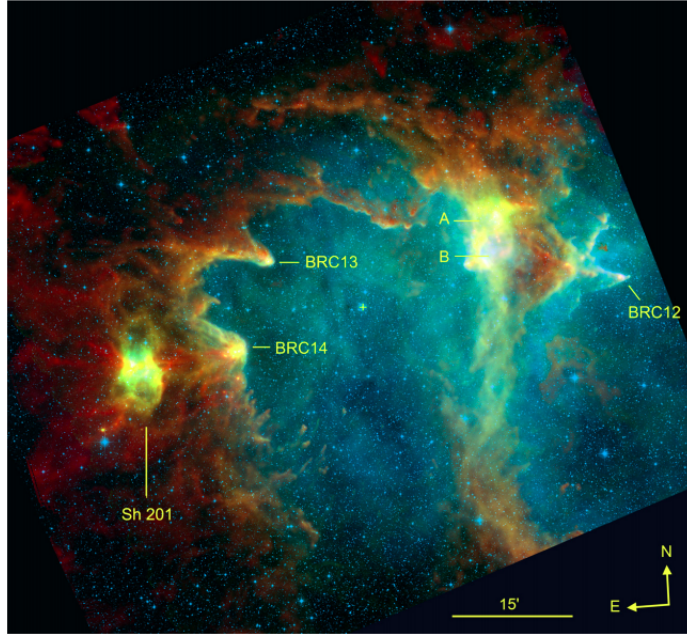


Figure 1.9: Color-composite image of W5E HII region with $250 \mu\text{m}$ Herschel-SPIRE (red), $100 \mu\text{m}$ Herschel-PACS (green), DSS2 survey (blue). The yellow cross shows HD18326 which is a ionizing star cluster for W5E HII region (Deharveng et al. 2012).

and 58 sources outside the rim as 2.32 ± 1.22 Myr.

This thesis has total five chapters. It starts with discussing various methodology used in this project in chapter 2. This involves brief introduction of aperture and PSF photometry (sec. 2.0.1, 2.0.2). Following this, various methods for extinction estimation that we have carried out is introduced (see sec. 2.1). After this, by introducing various types of YSO classification, we have given a brief introduction to spectral energy distribution modelling (see 2.4). Following that, we have discussed different methods and algorithm followed by VOSA (see sec. 2.4.2).

In chapter 3, we have kept our focus on data reduction and analysis. It begins with introducing the multi-wavelength spectrum overview, leading to data reduction and calibration process. Following section starts with optical spectrum (Pan-STARR PS1, see sec. 3.1), then to near-infrared (NEWFIRM, see sec. 3.2) and finally ends up with mid-infrared (Spitzer IRAC, see sec. 3.3) data reduction and analysis. In chapter 4, we have given our results and discussion. It contains all the maps and plots derived for the data reduction, identification various classes of YSO's and finally coming up the star formation rate and efficiency. Chapter 5 gives the conclusion and possible future work.

Chapter 2

Methodology

In this chapter, we have discussed the various data analysis methods used for our study. These include, photometric methods like aperture and PSF photometry, extinction estimation, YSO identification and SED modelling.

2.0.1 Aperture Photometry

The basic principle of aperture photometry is to add up the flux observed within a given radius also called as ‘Aperture’ from the object center. Prior to this, it is essential to subtract the sky background such that it measures only the flux from the astronomical object. As it is known that seeing, focusing errors, tracking, mount errors etc. may bias the amount of flux within the aperture radii. Hence aperture radius should be considered carefully. Figure 2.1 shows the aperture radii, inner and outer radii to measure the source flux and background flux respectively.

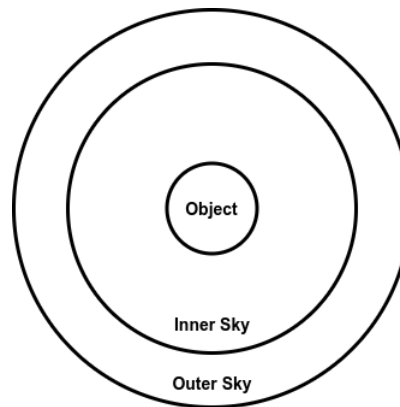


Figure 2.1: Point source photometry showing the aperture radius with the inner and outer sky radius to measure background sky value.

Choice of optimum aperture is crucial. As the aperture radius increase, the Poisson shot

noise of the background sky also increase. The S/N ratio of the flux approaches a maxima at a moderate aperture radius (Howell 1989). Using a smaller radius brings the issue that the fraction of the total flux will be different for objects of different flux. Hence, aperture corrections has to be done.

Image Reduction and Analysis Facility (IRAF) provides the following tasks to perform aperture photometry;

1. *imexamine* - single aperture photometry (defined at ‘rimexam’) using the image display software ds9.
2. *phot* - User interactive or batch mode multi-aperture photometry for multiple point sources with several parameters.
3. *qphot* - User interactive or batch mode multi-aperture photometry for multiple point sources with minimal parameters.
4. *polyphot* - User interactive or batch mode single aperture photometry for polygon-like apertures.
5. *wphot* - User interactive or batch mode multi-aperture photometry for multiple point sources with parameter weighting option.

In order to calculate the magnitude of point source, following are the quantities measured by the various tasks of IRAF for photometry (Davis et al. 1994).

$$Flux = Sum - (area \times msky) \quad (2.1)$$

$$Magnitude = Zmag - 2.5 \log_{10}(Flux) + 2.5 \log_{10}(itime) \quad (2.2)$$

$$err = \left(\frac{\left[\frac{Flux}{epadu \times Rdnoise} + (area \times stdev^2) + (area \times stdev)^2 \right]}{nsky} \right)^{1/2} \quad (2.3)$$

$$merr = 1.0857 \times \frac{error}{Flux} \quad (2.4)$$

where itime: integration time, Flux: Total flux inside aperture excluding sky value, Sum: Total counts including sky value in aperture, area = Aperture area, msky: Mean sky value,

Zmag: Zero-point magnitude, itime: Exposure time (Sec), epadu: CCD Gain in adu, Rdnoise: CCD Read Noise, stdev: Standard deviation of background, nsky: Number of sky pixels.

2.0.2 Point spread function (PSF) Photometry

PSF photometry used in case of crowded fields, where point sources are very closely located, hence fixing an aperture without contamination from the neighbouring source becomes extremely difficult. The task DAOPHOT is used for the same. DAOphot was first developed by Dr. Peter Stetson for precise ground-based photometry for crowded fields like globular clusters. This method can remove the variations due to seeing and enabling larger effective radii to be used. Following are the main tasks involved in PSF photometry;

1. *daofind* - search point sources in a FITS image using the DAOFIND algorithm.
2. *phot* - This computes initial magnitudes for a list of stars, it is simply an aperture photometry with one or more than one aperture radius, the results from this photometry is used to model the PSF. In place of ‘phot’ any other aperture photometry tasks can be used as mentioned in section 2.0.1.
3. *psf* - Estimates the point spread function for the list of point sources.
4. *peak* - This fits the PSF model to single point source.
5. *nstar* - This models the PSF for multiple point sources defined earlier by user.
6. *allstar* - This task groups and fits the PSF model to multiple point source simultaneously.
7. *substar* - This subtracts the fitted point source from the FITS image.

Following is the summary of PSF photometry including all the steps and tasks to perform modelling and estimating photometric magnitudes;

- In order to prepare list of all the point sources, an user defined threshold (usually $3-5\sigma$) value is given. Task *daofind* is used to consider source to be star (point source) or extended source like galaxies or defects like cosmic rays. In order to perform this operation, two pset parameter files are important to configure, *datapars* and *findpars*. It is important to fix parameters like ‘datamin’, ‘datamax’, ‘readnoise’, ‘epadu’ etc. before doing the *daofind* task. The values for these parameters can be found in the header of the image.

- Aperture photometry is then carried out on all the identified point sources from *daofind*. Before doing this task, it is important to fix three pset parameter files, *photpars*, *centerpars* and *fitskypars*. *photpars* mainly handles parameters related to setting aperture radii. Parameter file *centerpars* fixes parameters like ‘calgorithm’ and ‘CBOX’ which are important to initiate the aperture photometry. Similarly *fitskypars* sets parameters which are important to estimate the background like ‘annulus’ and ‘dannulus’.
- Before performing PSF modelling, identify point sources that are close to the edge of FITS image or are too faint and then remove them from the list. Consider only bright, isolated stars spread across the FITS frame. This is done by tasks like *psselect*, that fixes the parameters like ‘maxnpsf’ (the number of PSF point sources to be modelled) or ‘interac’ (the process can be done manually or interactively).
- In order to build a semi-empirical PSF model, all the PSF point sources identified are used. The analytic functions available to model the PSF are bivariate Gaussian, Moffat or Lorentz functions. The modelling is an iterative process to produce a ‘clean’ PSF in some cases, whereby PSF modelling and fitting is performed. Contamination in the form of faint neighbouring point sources are identified, subtracted and then fitting is carried out. In order to model the PSF, first *daopars* parameter file has to be set. This includes choice of analytic function to be modelled by setting ‘function’ parameter. The other two important parameters here are ‘psfrad’ and ‘fitrad’.
 1. *psfrad*: This defines the radius of circle within which the PSF model is set. It can be 1-2 pixel greater than 2-3 times FWHM of the bright star in the FITS image. This should never be set to more than size of PSF model. But this can be set smaller values in task *ALLSTAR*.
 2. *fitrad*: This parameter defines fitting radius in scale unit. Only pixel fall within this radius from the center of point source will add to the fits by *ALLSTAR*. This has to be equal to the average FWHM of the list of PSF point sources. Example psf model is shown in Fig. 2.2.
- Using the centroid of a point source as the profile center and sky background as determined for aperture photometry in step 2, the PSF model is shifted and scaled to fit the observed stellar FITS image by non-linear least-squares. The scaling estimates the magnitude values. This process of photometry including aperture and PSF photometry is illustrated in Fig. 2.3 as a flowchart.

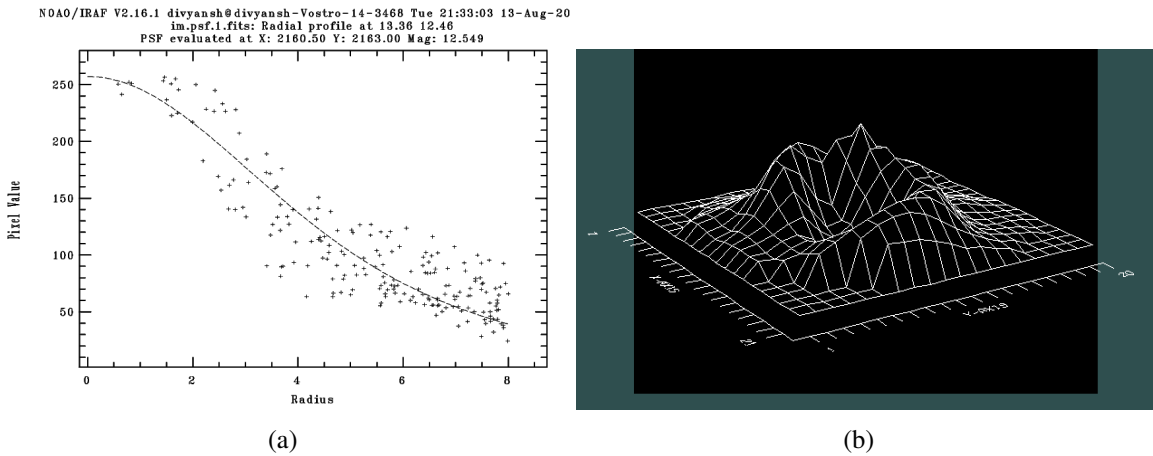


Figure 2.2: Example of PSF model fitted using analytic function MOFFAT on linear scale (a) and on two dimensional plane (b).

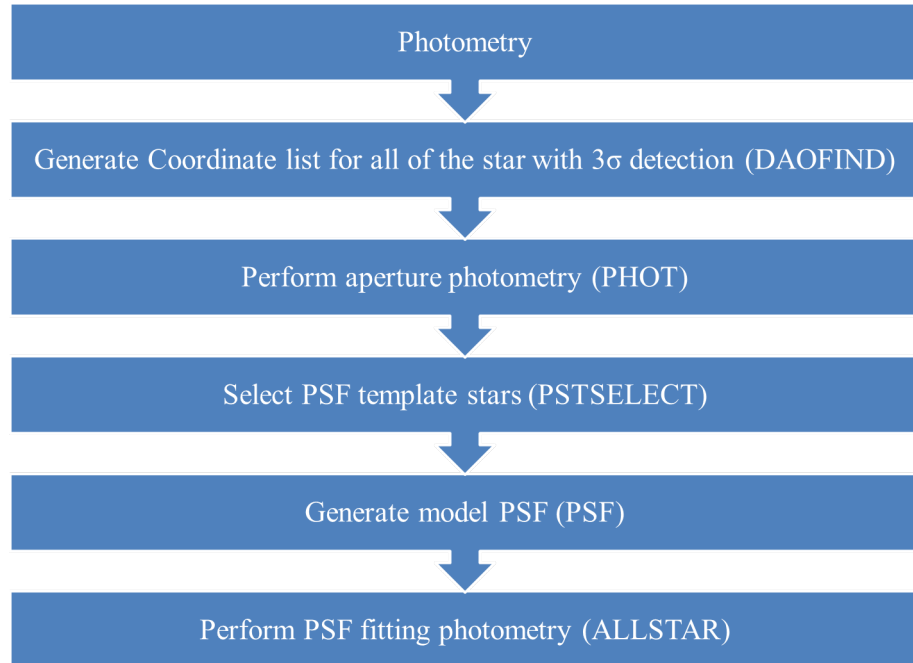


Figure 2.3: PSF photometry Flowchart

2.1 Extinction Estimation Methods

2.1.1 Column Density Map

Column density map can be used for extinction calculation by using the linear relationship between column density $N(H_2)$ and visual extinction A_V . In order to calculate the column density, it is assumed that the emission from cold dust at Herschel-SPIRE wavelengths is optically thin. Using this approximation, the estimation of properties like mass of the different structures, hydrogen column density, temperature etc is done. Derivation and limitations of this method are discussed in detail by Hildebrand (1983). The total mass (including both gas and dust) of a region is related to its flux density S_ν by:

$$M_{gas+dust} = 100 \left(\frac{S_\nu D^2}{\kappa_\nu B_\nu(T_{dust})} \right) \quad (2.5)$$

Here D is distance to source, κ_ν is dust opacity per unit mass and $B_\nu(T_{dust})$ is Planck distribution. Usually gas-to-dust ratio is considered as 100 (Deharveng et al. 2012). Calculation of dust opacity depends on the shape, size, chemical composition, physical structure, grains temperature (Martin et al. 2012; Fischera & Martin 2012; Roy et al. 2013). Preibisch et al. (1993) has suggested to estimate the dust opacity κ_ν for protostellar envelopes as given by;

$$\kappa_\nu = 10 \left(\frac{\nu}{1000GHz} \right)^2 \quad (2.6)$$

Due to several unknown properties of the dust grains, the dust opacities is uncertain by at least a factor ~ 2 . Hence, the quantities derived by this method also shows uncertainty of the order of ~ 2 Preibisch et al. (1993). Using the Herschel fluxes and a modified blackbody (also known as grey body), estimation of the temperature is done using grey body fitting. Using the surface brightness F_ν and the temperature T_ν from the grey body fitting, the H_2 column density is given by;

$$N(H_2) = \frac{100F_\nu}{2.8\kappa_\nu B_\nu(T_{dust})m_H\Omega_{beam}} \quad (2.7)$$

where, F_ν is surface brightness expressed in Jy/beam, B_ν is flux density in Jy, m_H is the hydrogen mass, Ω_{beam} is the beam solid angle and $N(H + H_2)$ is in particles $cm^{-2}mag^{-1}$. The visual extinction can now be estimated from this column density as;

$$N(H + H_2) = 5.8 \times 10^{21} E(B - V) \quad (2.8)$$

From the relation between interstellar extinction A_V and the color excess given by;

$$A_V = 3.1 \times E(B - V) \quad (2.9)$$

Rearranging above two equation will give;

$$A_V = 5.34 \times 10^{-22} N(H + H_2) \quad (2.10)$$

or;

$$A_V = 1.07 \times 10^{-21} N(H_2) \quad (2.11)$$

Equation 2.11 gives the extinction value in V-band for a given line-of-sight.

2.1.2 PNICER

Extinction due to dust is one of the most promising tracer of the gas distribution in interstellar medium. Although, the extinction measurement is limited by several systematic uncertainties occur during calculation of intrinsic color of background sources. To overcome this issue, PNICER is an astronomical software made for estimating extinction using unsupervised machine learning algorithms for individual sources by creating extinction maps (Meingast et al. 2017). Determination of extinction towards a single sources is done by fitting Gaussian Mixture Models along the extinction vector to a nearly extinction-free control field data which makes it possible to define the extinction of sources using probability densities. This fits Gaussian Mixture Models along the extinction vector in arbitrary numbers of dimensions to derive probability densities describing the extinction for each source.

It requires two different regions, namely science field and control field. The science field is the target region and the control field is a region with nearby unextincted regions (or regions with minimum extinction). This is used to compare the two region's extinction. Using the machine learning algorithm, it makes a map which gives A_V values for each pixel. It uses JHKs data and their measured color with a given extinction law to get the extinction value A_V . PNICER requires few dependencies like numpy, astropy, scipy, matplotlib, and scikit-learn. Using this method, it can effectively eliminates known biases and makes them in cases of deep observational data (in case the number of background sources is significant, or when a large parameter space is used in the intrinsic color distributions). PNICER is offered as an open-source software written entirely in Python.

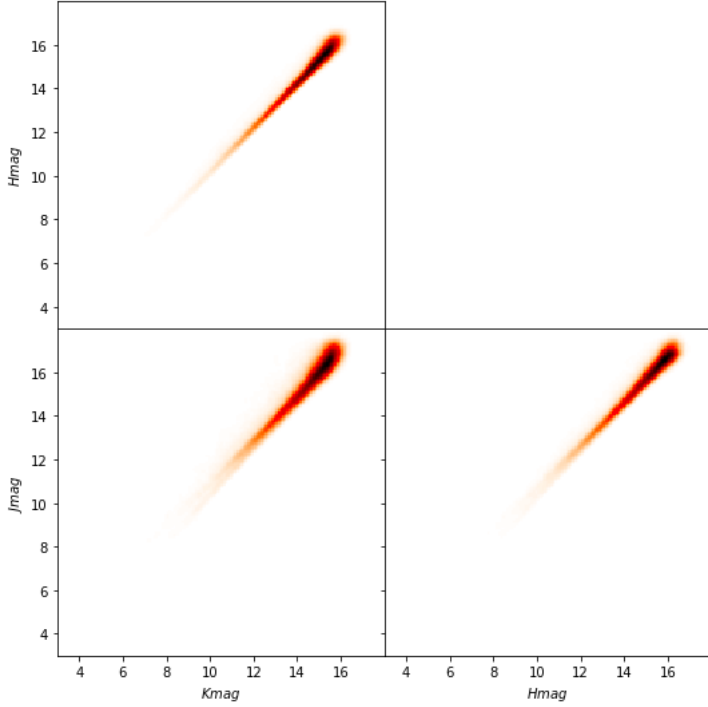


Figure 2.4: Plot generated by the PNICER showing the density distribution for the feature combinations. This plot is generated as an example for Orion A region.

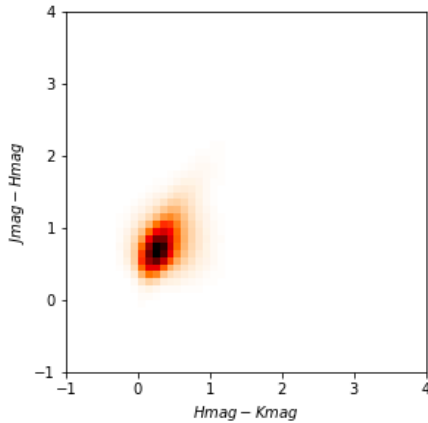


Figure 2.5: CC plot generated by the PNICER showing the [J-H] / [H-K] distribution.

As mentioned earlier, PNICER uses measured intrinsic magnitudes (or colors) in an extinction-free control field to deredden an extincted sources at the science field. In order to generate an extinction map (Example map of Orion A molecular cloud is given) a science field (Orion A) and another field (may be a few degrees away) as control field is considered. Two JHK_s data sets for each field can be retrieved as a FITS table from platforms like

VizieR¹. After setting up the python environment, one can give the path of these two data sets to initiate the process. An extinction vector is required, which is by default set up as a K-band normalized vector [2.5, 1.55, 1.0] from Indebetouw (2015).

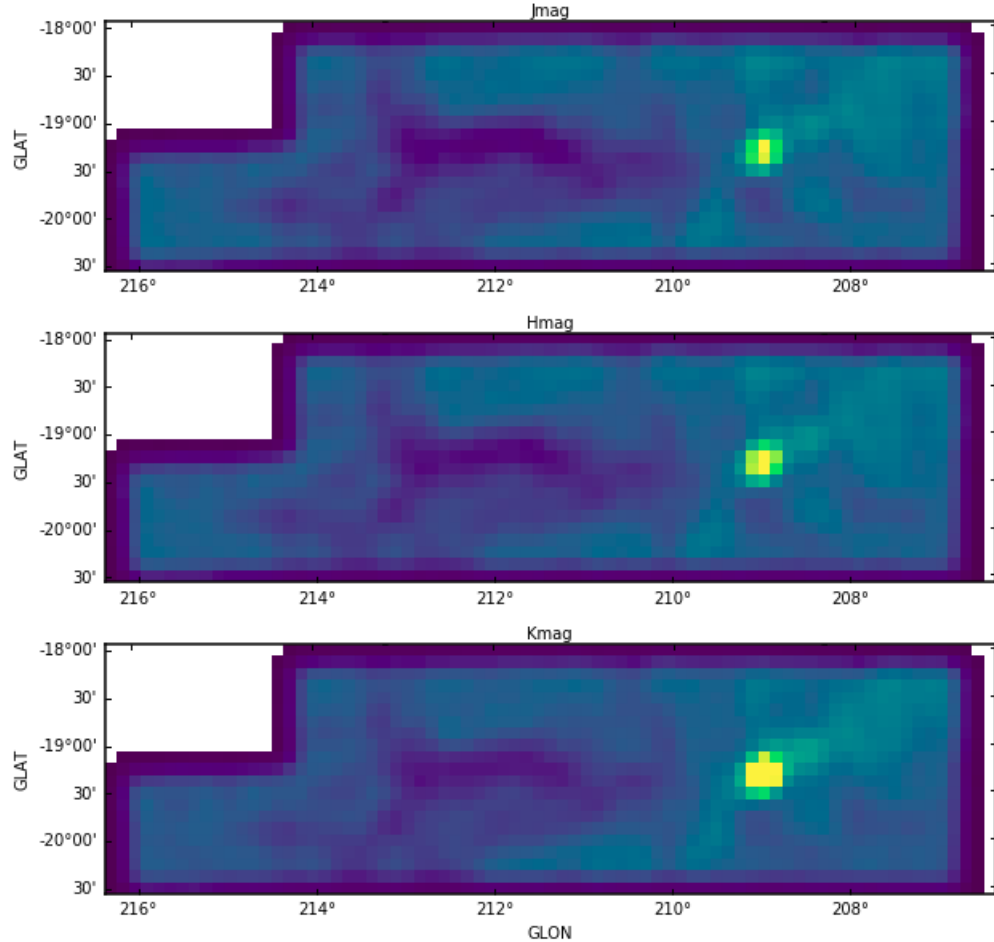


Figure 2.6: Plot generated by the PNICER showing the kernel density distribution map for the JHK_s combinations, Jmag (top), Hmag (middle) and Kmag (bottom). The color coding gives the normalized probability density function for extinction. The yellow pixels shows maximum extinction probability. This plot is generated as an example for Orion A region.

PNICER does include some plotting methods, which helps visualize data. It first plots the density distribution for the JHK_s combinations which is shown in Fig. 2.4, following that it also shows the CC diagram $[J-H] / [H-K]$ which is shown in Fig. 2.5. It also displays a kernel density map for JHK_s band as shown in Fig. 2.6. This shows the map in galactic projection with color coding showing normalized extinction probability density function. This is estimated by comparing JHK_s data of science field with control field. After this,

¹<http://vizier.u-strasbg.fr/viz-bin/VizieR-2>

it generates the extinction map of the region. This map comes along with two other maps also, first the error in A_V and second, the stellar number distribution. The entire panel is shown in Fig. 2.7. For more details on the part of unsupervised learning technique, please refer Meingast et al. (2017). The steps involved in generating the extinction map is given in detail at Smeingast (2017).

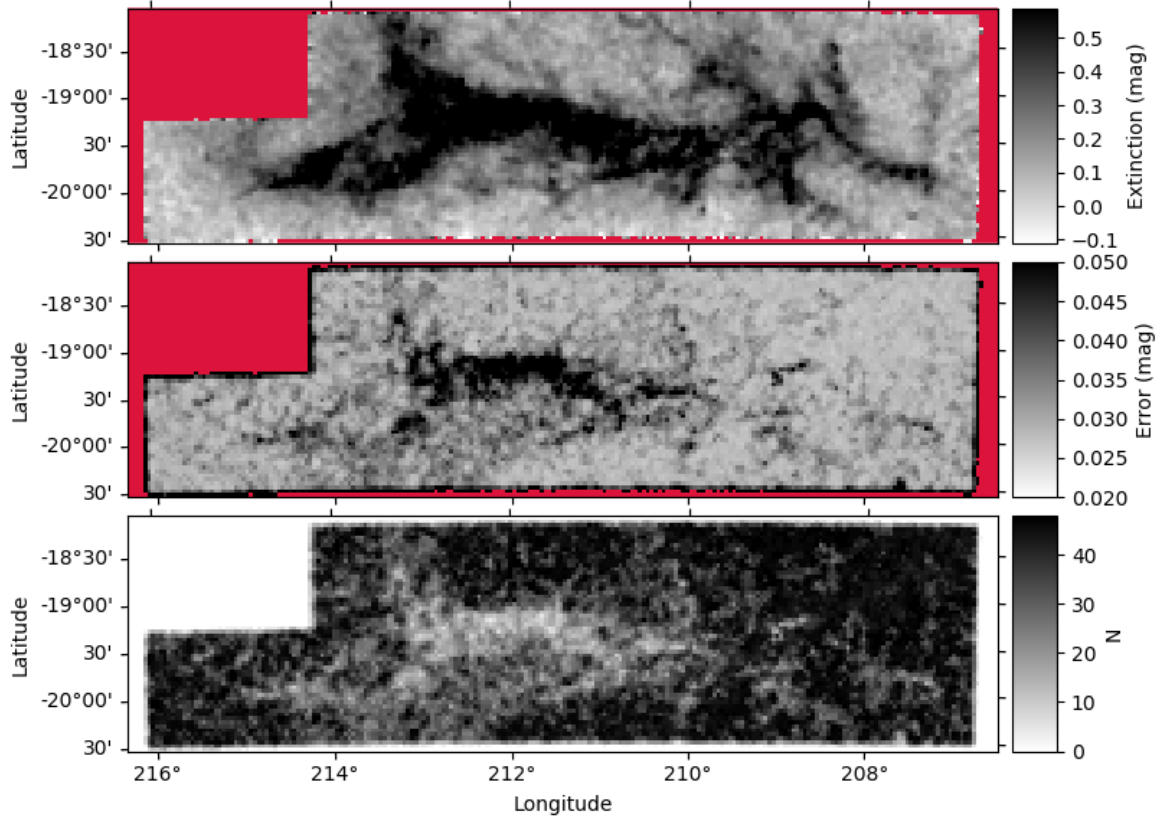


Figure 2.7: Plot generated by the PNICER showing the extinction map in V-band (top), the uncertainty map (middle) and stellar number density map (bottom). This plot is generated as an example for Orion A region.

2.1.3 Using NIR and MIR photometry

This method is suggested by Gutermuth et al. (2009) (appendix A, phase 2) which uses five photometric band to estimate the extinction. In this method, H and K band are essential, J and [CH1][CH2] are used whenever they are available. The data used must have high quality photometry ($\sigma < 0.2$). These details are sufficient to discriminate the excess source with those which are showing NIR excess because of the line of sight dust only (Gutermuth et al. 2005). To estimate the line of sight extinction, which in this method is parameterized by color excess E_{H-K} from the line of sight reddening due to dust.

The process of estimating the extinction is in two steps. In the first step, A_V is estimated by using all the sources which has J band data available, along with H and K_S photometric data. This also uses color excess ratio (E_{J-H} / E_{H-K}) with the baseline color of main sequence stars from Bessell & Brett (1988), classical T-Tauri stars (CTTS) locus from Meyer et al. (1997). This is accomplished by constraining the $[J-H]_o \leq 0.6$ which is a approximation for the intrinsic color of low mass stars. Using all these conditions, the first set of equations are given by;

$$[J - H]_o = 0.58 \times [H - K]_o + 0.52; \quad [H - K]_o > 0.14 \quad (2.12)$$

$$[J - H]_o = 0.60; \quad [H - K]_o \leq 0.14 \quad (2.13)$$

From the standard equation of color transformation, we can write;

$$[H - K]_o = [H - K]_{meas} - ([J - H]_{meas} - [J - H]_o) \times \frac{E_{J-H}}{E_{H-K}} \quad (2.14)$$

Putting eq. 2.12 to eq. 2.14, we get;

$$[H - K]_o = \frac{[J - H]_{meas} - \frac{E_{J-H}}{E_{H-K}} \times [H - K]_{meas} - 0.52}{0.58 - \frac{E_{J-H}}{E_{H-K}}} \quad (2.15)$$

Putting eq. 2.13 to eq. 2.14, we get;

$$[H - K]_o = [H - K]_{meas} - ([J - H]_{meas} - 0.6) \times \frac{E_{J-H}}{E_{H-K}} \quad (2.16)$$

Using eq. 2.15 and eq. 2.16, one set of intrinsic color can be calculated but these calculation has to be restricted for only those sources which has J band data available.

In second step, rest of the sources where J band data is unavailable but CH1 and CH2 data is available are used. Using the color excess $\frac{E_{[CH1]-[CH2]}}{E_{H-K}}$, derived from Flaherty et al. (2007) along with the baseline color YSO locus of $[CH1 - CH2] / [H - K]$ color-color space given in Bessell & Brett (1988); Gutermuth et al. (2005). This constrain is forced by applying condition $[H - K]_o \leq 0.2$, which is an approximation for intrinsic color of low mass stars. Using these, the second set of equations are as follow;

$$[H - K]_o = 1.33 \times [CH1 - CH2]_o + 0.133; \quad [CH1 - CH2]_o > 0.06 \quad (2.17)$$

$$[H - K]_o = 0.20; \quad [CH1 - CH2]_o \leq 0.06 \quad (2.18)$$

from the standard equation of color transformation, we can write;

$$[H - K]_o = [H - K]_{meas} - ([CH1 - CH2]_{meas} - [CH1 - CH2]_o) \times \left(\frac{E_{H-K}}{E_{[CH1-CH2]}} \right) \quad (2.19)$$

Putting eq. 2.17 to eq. 2.19, we will get;

$$[H - K]_o = \frac{1.33 \times \left(\frac{E_{H-K}}{E_{[CH1-CH2]}} \times [H - K]_{meas} - [[CH1 - CH2]]_{meas} \right) - 0.133}{\left(1.33 \times \frac{E_{H-K}}{E_{[CH1-CH2]}} \right) - 1} \quad (2.20)$$

Using these two steps, $[H-K]_o$ for all the source from eq. 2.15, eq. 2.16, eq. 2.18 and eq. 2.20 is calculated. Using the following steps, the visual extinction (A_V) value is calculated from the intrinsic color $[H-K]_o$;

we can define;

$$\frac{E_{H-K}}{E_{B-V}} = \frac{E_{H-V}}{E_{B-V}} - \frac{E_{K-V}}{E_{B-V}} \quad (2.21)$$

From Rieke & Lebofsky (1985); for the interstellar medium $\frac{E_{H-V}}{E_{B-V}} = -2.55$ and $\frac{E_{K-V}}{E_{B-V}} = -2.744$, such that;

$$\frac{E_{H-K}}{E_{B-V}} = \frac{E_{H-V}}{E_{B-V}} - \frac{E_{K-V}}{E_{B-V}} = 0.194 \quad (2.22)$$

And as we know for the interstellar medium, the color excess to visual extinction ratio is given by;

$$\frac{E_{B-V}}{A_V} = 3.1 \quad (2.23)$$

Using the above two equations;

$$A_V = \frac{3.1}{0.194} \times E_{H-K} = 15.979 \times ([H-K]_{meas} - [H-K]_o) \quad (2.24)$$

Where $[H-K]_{meas}$ is the measured color excess and $[H-K]_o$ is the intrinsic color calculated from eq. 2.15, eq. 2.16, eq. 2.18 and eq. 2.20). Hence the extinction in V-band can be calculated from equation 2.24.

2.2 Classification of Young Stellar Objects

It is empirically defined to measure the infrared excess as slope of SEDs to estimate the age of young stellar objects. These slop is called *Infrared spectral index* and it is given by:

$$\alpha_{IR} \equiv \frac{d \log (\lambda F_\lambda)}{d \log \lambda} \quad (2.25)$$

Table 2.1: YSO classification (Stahler & Palla 2008)

S. No.	YSO Class	NIR spectral index	Comments
1	Class 0	$\alpha > 0$	Deeply embedded, Rising SEDs, sources with strong, spherical envelopes
2	Class I	$\alpha > 0$	Rising SEDs, sources with strong spherical envelopes
3	Class II	$-2 < \alpha < 0$	Pre-Main Sequence star with optically thick accretion disk
4	Class III	$-3 < \alpha < -2$	Little or no disk left

Following is the brief discussion of three categories of young stellar objects (Adams et al. 1987; Lada & Lada 2003; Robitaille et al. 2007; Stahler & Palla 2008):

- **Class 0 sources** ($\alpha_{IR} > 0$): Class 0 sources are embedded very deep and they are impossible to get observed even in near-infrared. Extended sub millimeter continuum emission shows the presence of spheroidal circumstellar dust envelope and peak comes in sub-millimeter wavelengths. In addition to this, they have also observed

high ratio between sub-millimeter luminosity to bolometric luminosity which suggest that envelope mass must have exceeded the central stellar mass. It also shows bipolar CO outflows (Bally et al. 1999).

- **Class I sources** ($\alpha_{IR} > 0$): These are the sources whose SED fits the models of mass accreting YSOs from circumstellar disk. These are completely obscured in visible spectrum that implies that the sources must be deeply embedded. The strong NIR excess is the result of the emission from the accreting circumstellar disk. They are often associated with the molecular outflows.
- **Class II sources** ($-2.56 < \alpha_{IR} < 0$): These are the evolved version of class I objects in which the surrounding envelope is pushed away by strong stellar winds or may be molecular outflows. Unlike the Class I sources, these are visible in optical wavelengths. This phase of evolution is popularly known as classical T-Tauri phase (CTTs). SEDs of such sources can be fitted by a photo-sphere with circumambient disk. These sources often have molecular outflows.
- **Class III sources** ($\alpha_{IR} < -2.56$): This phase of evolution includes sources known as Weak line T-Tauri (WTTs). In these sources the circumstellar disk is partially or completely accreted (or dispersed by stellar winds and molecular outflows). SEDs of such sources very much resembles a stellar blackbody and can be modelled by a simple blackbody source with interstellar medium in between. They might show a little (or none) excess in NIR spectrum because of the cold dust particles presence. Table 2.1 gives the summary for the classification based on SED slope.

2.3 YSO Identification

The young stellar objects (see Section 2.2) show reddening due to interstellar gas and dust as well as circumstellar material. This circumstellar reddening caused because of the presence of circumstellar disc (or envelope). These envelope/disk absorbs optical/UV radiation and re-radiate them at longer wavelengths like NIR/MIR. To identify these YSOs, the contribution of interstellar reddening is subtracted from the total reddening such that only the circumstellar reddening left. Hence to identify the YSO, first YSOs are dereddened by using line-of-sight extinction from Section 4.2. Based on the IR excess, the sources can be classified in Class I/II/III sources (see Section 2.2). The identification and classification of these YSO is explained as a multi-phase process (Gutermuth et al. 2005, 2009). The

first phase eliminates the false NIR excess sources and first set of YSOs. This method uses the IRAC four bands. Second phase deals with identification of another set of YSOs using JHKs and CH1/CH2 data. The final phase adds another set of YSOs by using MIPS 24 μm photometric data.

2.3.1 YSO identification:Phase I

Beginning of first phase starts with eliminating the false source like PAH background galaxies, AGNs etc. To eliminate the active star forming galaxies, it uses the fact that these sources shows very red [CH3 - CH4] colors (Stern et al. 2005). Sources which obey following constrains are identified as active PAH galaxies;

$$[CH2 - CH3] < \frac{1.05}{1.2} \times ([CH3 - CH4] - 1) \quad (2.26)$$

$$[CH1 - CH3] < \frac{1.5}{2} \times ([CH2 - CH4] - 1) \quad (2.27)$$

$$[CH2 - CH3] < 1.05 \quad (2.28)$$

$$[CH3 - CH4] > 1.00 \quad (2.29)$$

$$[CH1 - CH3] < 1.50 \quad (2.30)$$

$$[CH2 - CH4] > 1.00 \quad (2.31)$$

$$[CH2] > 11.50 \quad (2.32)$$

A similar constraints is drawn for the broad-line AGN, these sources shows their MIR color largely consistent with the true NIR excess YSOs (Stern et al. 2005). Unlike the previous case where it uses CC plot, this time it uses CMD plot which is [CH2] / [CH2 - CH4] plot. The sources which follows given constraints are identified as broad line AGNs can are discarded;

$$[CH2 - CH4] > 0.5 \quad (2.33)$$

$$[CH2] > 13.5 + ([CH2 - CH4] - 2.3)/0.4 \quad (2.34)$$

$$[CH2] > 14.0 + ([CH2 - CH4] - 0.50) \quad (2.35)$$

$$[CH2] > 14.5 + ([CH2 - CH4] - 1.2)/0.3 \quad (2.36)$$

$$[CH2] > 13.5 \quad (2.37)$$

To eliminate the unresolved knots of shock emission, which is another source of contamination, it again uses the CC diagram $[CH1 - CH2] / [CH3 - CH4]$. Following are the conditions for which unresolved knots of shock emission are identified;

$$[CH1 - CH2] < \frac{1.20}{0.55} \times ([CH2 - CH3] - 0.3) + 0.8 \quad (2.38)$$

$$[CH2 - CH3] \leq 0.85 \quad (2.39)$$

$$[CH1 - CH2] > 1.05 \quad (2.40)$$

There is another source which can pretend to be a NIR excess source, which is when a resolved PAH emission has contaminated the photometric apertures of faint field stars, which shows spurious excess emission in $[CH3]$ and $[CH4]$ bands. These can be identified with following conditions;

$$\sigma_1 = \sigma[[CH2 - CH3]] \quad (2.41)$$

$$\sigma_2 = \sigma[[CH1 - CH2]] \quad (2.42)$$

$$[CH1 - CH2] - \sigma_2 \leq 1.40 \times (([CH2 - CH3]) + \sigma_1 - 0.7) + 0.15 \quad (2.43)$$

$$[CH1 - CH2] - \sigma_2 \leq 1.65 \quad (2.44)$$

Now once all these contaminants are eliminated from the database, first set YSOs can be identified. With all those sources, which shows following are identified as Class I YSOs;

$$[CH2 - CH3] > 0.70 \quad (2.45)$$

$$[CH1 - CH2] > 0.70 \quad (2.46)$$

With those objects remaining, sources which shows following conditions are identified as Class II YSOs;

$$\sigma_3 = \sigma[[CH2 - CH4]] \quad (2.47)$$

$$\sigma_4 = \sigma[[CH1 - CH3]] \quad (2.48)$$

$$[CH2 - CH4] - \sigma_3 > 0.50 \quad (2.49)$$

$$[CH1 - CH3] - \sigma_4 > 0.35 \quad (2.50)$$

$$[CH1 - CH3] + \sigma_4 \leq \frac{0.14}{0.04} \times (([CH2 - CH4] - \sigma_3) + 0.5) \quad (2.51)$$

$$[CH1 - CH2] - \sigma_4 > 0.15 \quad (2.52)$$

2.3.2 YSO identification: Phase II

Second phase of YSO identification involves five band identification scheme (JHKsCH1CH2), high quality photometric data with read flag set as '222' in case of JHKs from 2MASS is considered. After dereddening the sources by following the procedure explained in Section 2.1.3, the sources can be identified as Class II sources if they follow these conditions;

$$\sigma_1 = \sigma[[CH1 - CH2]]_{meas} \quad \sigma_2 = \sigma[[K - CH1]]_{meas} \quad (2.53)$$

$$[[CH1 - CH2]]_o - \sigma_1 > 0.101 \quad (2.54)$$

$$[[K - CH1]]_o - \sigma_2 > 0 \quad (2.55)$$

$$[[K - CH1]]_o - \sigma_2 > -2.85714 \times ([[CH1 - CH2]]_o - \sigma_1 - 0.101) + 0.5 \quad (2.56)$$

$$[CH1]_o < 16.30 \quad (2.57)$$

Sources which follows following condition along with the previous constraints;

$$[[K - CH1]]_o - \sigma_2 > -2.85714 \times ([[CH1 - CH2]]_o - \sigma_1 - 0.401) + 1.70 \quad (2.58)$$

$$[CH1]_o < 16.80 \quad (2.59)$$

The constraint applied in eq. 2.57 and eq. 2.59, is actually decided based on the depth of GLIMPSC-MIR survey. These two conditions basically eliminates faint extra-galactic contaminants. Sources identified with this phase along with phase I are considered as second YSO set.

2.3.3 YSO identification: Phase III

This phase rechecks the YSO set from phase I and phase II, and identifies deeply embedded YSOs using MIPS 24 μm which are not possible to identify by using IRAC and 2MASS. This also search for heavily reddened Class II sources which is misidentified as Class I. Following conditions are used to identify Class II sources;

$$[CH3 - [24]] > 2.5 \quad (2.60)$$

$$[CH2 - [24]] > 2.5 \quad (2.61)$$

and as protostar Class I if they follow;

$$[CH2 - [24]] > 4.5 \quad (2.62)$$

$$[CH4 - [24]] > 4.0 \quad (2.63)$$

Hence by using all these three phase, a final list of YSO is prepared.

2.4 Spectral Energy Distribution (SED) Modelling

2.4.1 Theoretical SED Models

In order to replicate the stellar conditions, many models have been proposed. Modelling the spectral energy distribution of the stellar photosphere is one of the most common method to estimate the fundamental parameters of young stellar objects which helps understanding the star formation process of a given region. The stellar photosphere is the outer surface layers from which radiation escapes the star. These layers can be mathematically probed using model atmospheres. The synthetic spectra can be generated by formulating the radiative transfer equations on the model photosphere. These model spectra is used to compare with the actual observed spectra (or some photometric data points in different wavelengths) to extract various physical parameter of the star.

The basic idea behind the photospheric model is to simulate the variation of temperature and pressure at different scales of photosphere. The variation in these quantities depends on various parameters of the star, but it is predominantly varies according to the radiation flux passing the different levels of photosphere and the successive absorption and emission by the same photospheric levels. These different depths of the photosphere act differently among themselves. However, the flux passing through these different depths are, if con-

sidered, constant (which is given by the Stefan-Boltzmann law; $F = \sigma T_{eff}^4$), then the only parameter to be taken care of is the absorption through these layers. This is governed by the term called *opacity*. The opacity is a function of the photospheric temperature (T_{eff}), pressure and the composition of the layer of photosphere. For the composition, metallicity is considered as proxy parameter. Similarly, surface gravity (g) can be treated as a proxy variable for pressure. In order to model the photosphere as a function of its depths, parameter space is defined as $[T_{eff}, \text{ metallicity}, \text{ surface gravity (g)}]$ (Hauschildt et al. 1996; Hauschildt & Baron 1999).

Simple models use an assumption of 1-D plane-parallel photosphere, which implies that the parameter space depends only on the depth of the atmosphere. However, this assumption fails for thick atmospheres and hence, spherically symmetric atmosphere is assumed in such case. Another common assumption used while modelling is local thermodynamic equilibrium (LTE). This assumption combines thermal, chemical and mechanical equilibrium and inflow of radiation, which can be considered to have a blackbody spectrum. The Maxwell-Boltzmann distribution can be applied to calculate the number of atoms or molecules occupying different excited energy states and the Saha equation can be used to determine the number of atoms in different ionization states. Many models also assume hydro-static equilibrium, and that the total flux passing through the outer layers remains constant with depth.

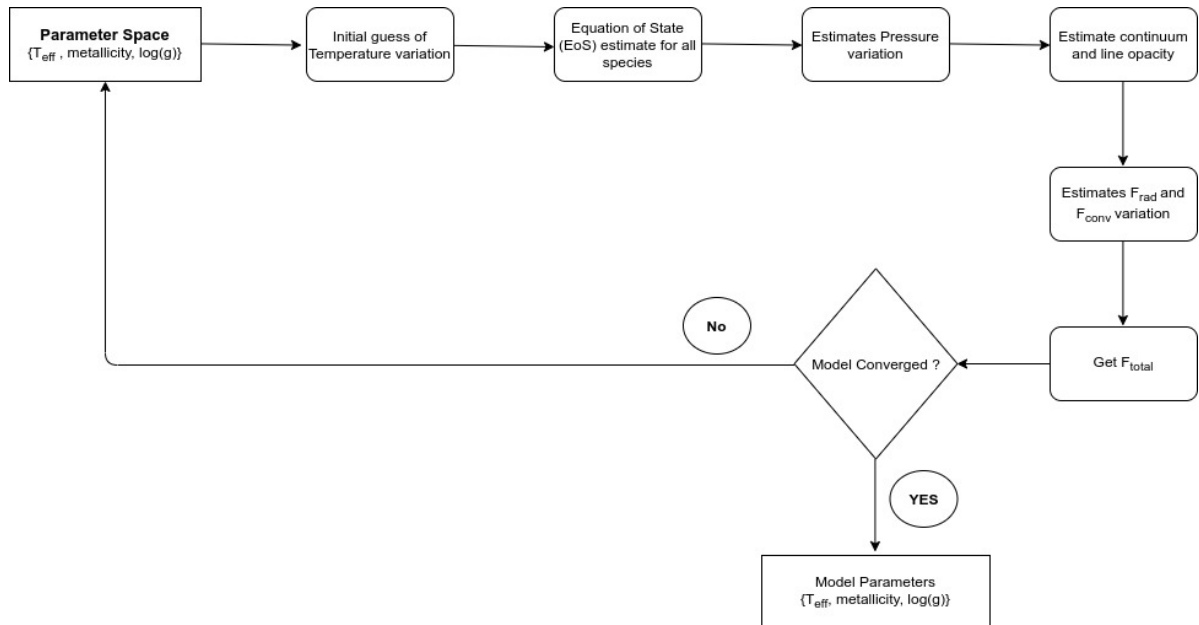


Figure 2.8: Flow chart showing the photosphere modelling process.

The amount of flux absorbed by the different layers of photosphere depends vividly on opacity, which intern is a function of composition of these different photospheric layers. It is computationally impossible to model the absorption feature of every element/molecule present in that layer. This problem is taken care by method called *opacity sampling*. This technique samples the wavelength space into smaller number of bins (closely about 1% of the space).

There is another method to handle the opacity called *opacity distribution function*. These are the pre-tabulated statistical function of line opacity (opacity defined over pressure and temperature for given set of abundance), generated for different set of pressure and temperature grid, which computes the opacity for entire grid and samples it according to the wavelength bin. Fig. 2.8 shows the iterative process of modelling the atmosphere. It initialize the process with the parameter space assumed over the different layers of atmosphere. After that the pressure is estimated with the presumed equation of state (it can be different for different atmospheric model). This leads to estimating the different line opacities with pressure and temperature gradient for each layer. After that, formulating the equation of radiative transfer, convective and radiative flux is estimated. Using these, calculation of the total flux crossing each layer is done. A converging value of flux leads to finalizing the parameter grid, otherwise, the deviation parameter space is calculated and feedback is applied to restart the process with an updated parameter space. Some of the commonly used models with their parameter grid is shown in table 2.2.

Table 2.2: Some commonly used theoretical models with their parameter grid space

Model	T_{eff} (K) (ΔT_{eff})	Metallicity (Δ Metallicity)	Log(g) (Δ Log(g))
Kurucz ATLAS9	3500 -50000 (250)	-2.5 - +0.5 (0.5)	0.0 - +5.0 (0.5)
Phoenix NextGen	800 - 70000 (100)	-4.0 - +0.5 (0.5)	-0.5 - +5.5 (0.5)
BT-NextGen	2700 - 70000 (100)	-4.0 - +0.5 (0.5)	-0.5 - +5.5 (0.5)
BT-Dusty	1700 - 2700 (100)	-4.0 - +0.5 (0.5)	-0.5 - +5.5 (0.5)
BT-Cond	800 - 70000 (100)	-4.0 - +0.5 (0.5)	-0.5 - +6.0 (0.5)
BT-Settle	400 - 70000 (100)	-4.0 - +0.5 (0.5)	-0.5 - +6.0 (0.5)
BT-Settle CIFIST	1200 - 7000 (100)	0	2.5 - 5.5 (0.5)

2.4.2 VOSA SED Analyzer

VO SED Analyzer (VOSA)² Bayo et al. (2008). is a online tool designed by Spanish Virtual Observatory (SVO) to perform task related to many astronomical analysis. This tool is developed to perform task in a user friendly environment in an automatic manner. VOSA is able to perform following tasks;

- VOSA can read photometric table build by user in given specific format.
- Using this user is able to make query to several catalogs accessible through VO services. This makes wavelength coverage to increase such that the user can analyze the data.
- Using this user can make query to various theoretical models and user can estimate their own synthetic photometry.
- Using this user can perform a test and examine which model can produce the observed data with least uncertainty. This allows user to make fitting optionally as well as optimize the interstellar extinction, such that, user can make likelihood of the model space as well as the reddening.
- To make the bolometric correction VOSA uses the best-fit model.
- Using modelling user can estimated bolometric luminosity for all sources.
- After modelling the SED, VOSA can generate a HR diagram using the estimated parameters using appropriate isochrones and evolutionary tracks.
- VOSA also provides an estimation of the mass and age of each source using the HR diagram.

2.4.2.1 IR excess detection and Model Fitting

This project aims to identify the young stellar object and estimate the physical properties like age, mass, luminosity etc. This can be achieved by fitting the SED with a theoretical model. VOSA provides large variety of theoretical models. To do this task, VOSA needs user photometric data in as specific format. The sample vosa input file is shown in table 2.3. The wide variety of filters available at VOSA library makes it convenient to do the entire

²Online VOSA tool can be accessed at <http://svo2.cab.inta-csic.es/theory/vosa/index.php>

Table 2.3: Sample VOSA input file

Obj ID	RA	DEC	dis	Av	filter	flux/mag	error	pntopts	objopts
11203	45.44665	60.64207	2100+/-300	—	NOAO/NEWFIRM.JX	12.867	0.021	—	Av:0.5/25
11203	45.44665	60.64207	2100+/-300	—	NOAO/NEWFIRM.HX	12.451	0.034	—	Av:0.5/25
11203	45.44665	60.64207	2100+/-300	—	NOAO/NEWFIRM.KX	12.3	0.019	—	Av:0.5/25
11203	45.44665	60.64207	2100+/-300	—	Spitzer/IRAC.I1	12.133	0.012	—	Av:0.5/25
11203	45.44665	60.64207	2100+/-300	—	Spitzer/IRAC.I2	11.872	0.029	—	Av:0.5/25
11203	45.44665	60.64207	2100+/-300	—	Spitzer/IRAC.I3	12.126	0.022	—	Av:0.5/25
11203	45.44665	60.64207	2100+/-300	—	Spitzer/IRAC.I4	13.855	0.313	—	Av:0.5/25
11203	45.44665	60.64207	2100+/-300	—	PAN-STARRS/PS1.g	15.7704	0.0011	—	Av:0.5/25
11203	45.44665	60.64207	2100+/-300	—	PAN-STARRS/PS1.r	14.9093	0.0021	—	Av:0.5/25
11203	45.44665	60.64207	2100+/-300	—	PAN-STARRS/PS1.i	14.44	0.0037	—	Av:0.5/25
11203	45.44665	60.64207	2100+/-300	—	PAN-STARRS/PS1.z	14.1575	0.0035	—	Av:0.5/25
11203	45.44665	60.64207	2100+/-300	—	PAN-STARRS/PS1.y	13.9236	0.0012	—	Av:0.5/25

process without taking care of filter transmission profile, convolution etc. Models available at VOSA for SEDs fitting consider contribution of photosphere only. Still for young sources like Class I/II, the circumstellar contribution can not be ignored, hence the color excess appear in observed SED. This color excess is detected by VOSA by observing the SED slope.

The algorithm used by VOSA to estimate the presence of infrared excess is inspired from the method given by Lada (2006). To identify the excess sources, the slope of the regression of the log-log curve (νF_ν versus ν) at every data point in IR is measured. If this slope turns out to be less than 2.56, VOSA consider it as start of infrared excess. The identification of excess is very prone to bad photometric data point. In order to avoid false IR excess detection, following steps are followed;

1. Process initiates with photometric point considered as $\lambda > 21500\text{\AA}$
2. If a points is labeled as ‘nofit’, then they are not considered for further steps.
3. The linear regression is done for every points from the first to is calculated.
4. Given that $y = \log(\nu F_\nu)$ which is a function of $x = \log(\nu)$) value calculated for this point with a line starting on initial point showing $slope = 2.56$, is called as y_L . The slope = 2.56 is called here as ‘critical slope’.
5. VOSA marks “excess suspicious” to a point if it qualifies both of the given conditions;
 - Regression slope (b) with the uncertainty in the slope, is smaller than critical

slope, that is;

$$b + \sigma(b) < 2.56 \quad (2.64)$$

- The observed value of y equal to minimum of 3σ above the value calculated from critical slope, that is;

$$(y_{obs} - y_l) > 3\sigma(y) \quad (2.65)$$

6. If a point is marked as ‘suspicious’, then it will not be considered for further process of linear regressions.
7. If two successive points are identified as ‘suspicious’ then VOSA marks infrared excess to the first points of the beginning.
8. If a point is marked as ‘suspicious’, however if the next point is not marked, then VOSA keeps the marks as it is. The first point (the suspicious one) is not be considered for further steps in making linear regression, however VOSA keep on checking the further points.
9. If VOSA finds the last point as ‘suspicious’ such that it qualifies both excess conditions mentioned above so that the point is taken at the beginning of IR excess.
10. In addition to these, one final condition is taken by VOSA. The slope calculated with the above method for one of the last two points at least, then it has to be sigma matched with smaller than critical slope of 2.56 ³.

2.4.2.2 SED Modelling

Once the IR-excess sources are identified, the photometric data point which belongs excess are no longer considered for fitting the theoretical model. Modelling process involves the comparison of the observed SED with the theoretical SEDs of a given model (multiple models can be selected by user, but it will take longer time with bigger grid). The best fitted grid point corresponds to the grid parameter [T_{eff} , $\log(g)$, metallicity]. The best

³Process of estimating the IR-excess source does not classify them further into Class I, II and III. This process will however, be able to make user identify excess sources and exclude excess data from modelling, please refer to vosa help-desk for step-wise procedure of IR excess identification.

fitting is done by using least square minimization method. The fitting accuracy is checked by calculating the reduced χ^2_r value, which is given by;

$$\chi^2_r = \frac{1}{N - n_p} \times \sum_{i=1}^N \left(\frac{(Y_{i,o} - M_d Y_{i,m})^2}{\sigma_{i,o}^2} \right) \quad (2.66)$$

Where N is total number of photometric data points; n_p is number of fitted parameters; Y_o is observed flux; Y_m is theoretical flux; σ_o is error in observed flux; M_d is the multiplicative dilution factor.

Calculation of M_d is done by scaling the observed SED to the theoretical SED from the model chosen. This factor is also given by the relation of radius to distance of source ($M_d = (R/D)^2$). The distance is given by the user in the input file as shown in Table 2.3.

2.4.2.3 Synthetic Photometry and Bolometric Luminosity

Once the source is modelled with a given theoretical model, it can be used to generate the synthetic photometry. Let the function defining theoretical spectra is given by $F_i(\lambda)$ with the given unit $\text{erg/cm}^2/\text{s}/\text{\AA}$ and let the given filter is given by a dimensionless filter response curve given by $G_f(\lambda)$. Then the synthetic photometry corresponding to the F_i spectra as it is observed through the given filter G_f can be expressed by;

$$F_{i,f} = \int_{\lambda} F_i(\lambda) N_f(\lambda) d\lambda \quad (2.67)$$

where the $N_f(\lambda)$ is the normalized filter response given by;

$$N_f(\lambda) = \frac{G_f(\lambda)}{\int G_f(x) dx} \quad (2.68)$$

The synthetic photometry can be used to confirm whether the difference in physical parameters, as obtained from the model fitting, can result in the observed variations in the colors of the two groups. The best fitting model is used to calculate the total observed flux for each source of the sample. The total theoretical flux for the source can be calculated by;

$$F_M = \int M_d \cdot F_M(\lambda) d\lambda \quad (2.69)$$

To estimate the total observed flux for the source, substitute the flux corresponding to the observing filters by the observed ones, such that most of the flux comes from the observa-

tions.

$$F_{tot} = \int M_d.F_M(\lambda)d\lambda + F_{obs} - F_{mod} \quad (2.70)$$

Theoretical density flux corresponding to the observed one $F_{o,f}$ can be calculated using the normalized filter response N_f given by;

$$F_{M,f} = \int M_d.F_M(\lambda)N_f(\lambda)d\lambda \quad (2.71)$$

To calculate the total observed flux, it is important to estimate the amount of overlapping among different filter observations. To do that, it approximates the coverage for each filter with its effective width after that it can identify spectral regions such that we define a *overlapping factor* as;

$$over_r = \frac{\sum W_i}{(\lambda_{max,r} - \lambda_{min,r})} \quad (2.72)$$

This can be used to estimate the degree of oversampling in every region and hence, the total observed and model flux can be approximate by;

$$F_{obs} = \sum_f \frac{F_{o,f} \cdot W_{eff,f}}{over_r} \quad (2.73)$$

and;

$$F_{mod} = \sum_f \frac{F_{M,f} \cdot W_{eff,f}}{over_r} \quad (2.74)$$

So total flux is given by;

$$F_{tot} = F_M + \sum_f \frac{[F_{o,f} - F_{M,f}] \cdot W_{eff,f}}{over_r} \quad (2.75)$$

Where $F_{M,f}$ and $F_{o,f}$ are the model and observed flux densities corresponding to the filter f. Now the bolometric luminosity can be given by;

$$L(L_\odot) = 4\pi D^2 F_{obs} \quad (2.76)$$

2.4.2.4 Estimation of stellar radius and mass

The multiplicative dilution factor (M_d) calculated from the fitting can be used to estimate the stellar radius given by;

$$R_1 = \sqrt{D^2 M_d}; \quad \delta R_1 = R_1 \frac{\delta D}{D} \quad (2.77)$$

There is another way of calculating the stellar radius using the T_{eff} and L_{bol} given by;

$$R_2 = \sqrt{\frac{L_{bol}}{4\pi\sigma_{SB}T_{eff}^4}}; \quad \delta R_2 = \sqrt{\frac{1}{4} \left(\frac{\Delta L_{bol}}{L_{bol}} \right)^2 + 4 \left(\frac{\Delta T_{eff}}{T_{eff}} \right)^2} \quad (2.78)$$

These values of stellar radius can be used to estimate mass, similar to estimation of stellar radius, mass will also have two expressions given by;

$$M = \frac{10^{\log(g)} R^2}{G_{NW}} \quad (2.79)$$

Putting expression of R_1 and R_2 in above equation is given by;

$$M_1 = \frac{10^{\log(g)} R_1^2}{G_{NW}}; \quad \delta M_1 = M_1 \sqrt{\ln(10)^2 (\Delta \log(g))^2 + 4 \left(\frac{\Delta R_1}{R_1} \right)^2} \quad (2.80)$$

and;

$$M_2 = \frac{10^{\log(g)} R_2^2}{G_{NW}}; \quad \delta M_2 = M_2 \sqrt{\ln(10)^2 (\Delta \log(g))^2 + 4 \left(\frac{\Delta R_2}{R_2} \right)^2} \quad (2.81)$$

2.4.2.5 Estimation of age and mass from HR diagram

Using various types of available theoretical isochrones and evolutionary track (e.g. BT-Settle, Siess, BACH15 etc.), estimation of the age (and mass) of the source is done. Once the HR diagram is plotted, then following are the steps involved in estimating the age and mass from the plot;

1. Identifying the points ($Teff$, $\log(L)$) falling within the isochrones (and Evolutionary tracks). For those who do fall, the following steps has been taken;

2. Using $(T_{eff,min}, T_{eff,max})$ and $(\log L_{min}, \log L_{max})$, making the small grid of 9 points (e.g. $(T_{eff}, \log L)$, $(T_{eff,min}, \log L)$, $(T_{eff,max}, \log L)$, $(T_{eff}, \log L_{min})$...) as shown in Fig. 2.9. For each source following are the steps carried out using these 9 point grid;

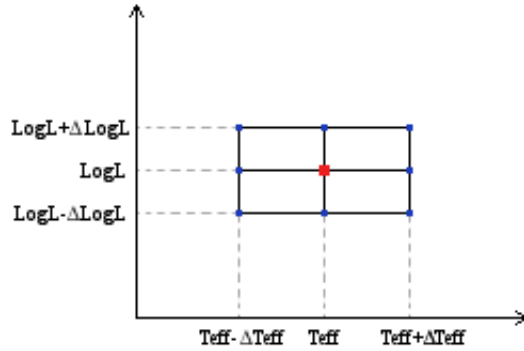


Figure 2.9: Uncertainty grid showing the nine points to calculate the age and mass with their own uncertainty.

3. The interpolation between isochrones involves finding the two closer isochrones to the $(T_{eff}, \log L)$ point (one to each side of the point). The two closest isochrone points would be required for the next step. Let the two closest isochrones have age T_1 and T_2 as shown in Fig. 2.10 (In case of mass estimation, the two closest evolutionary tracks have mass M_1 and M_2).

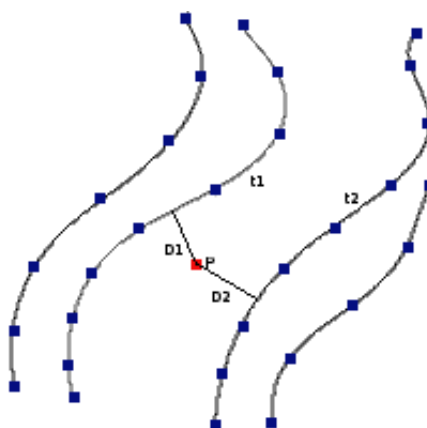


Figure 2.10: Interpolation is used to estimate the minimum distance from point P to get D_1 and D_2 from either side of the point to the respective isochrone.

4. Calculating the projection of $(T_{eff}, \log L)$ to the line defined by the closest point of isochrone (and evolutionary track for mass estimation) and either the next point in the curve or the prior one. This distance is used for the next step. Call this distance for each isochrone as D1 and D2.
5. To calculate the age of the source, take the average of T1 and T2 weighted by D1 and D2.

$$Age = \frac{(T1 \cdot D2 + T2 \cdot D1)}{D1 + D2} \quad (2.82)$$

6. Doing step (3-5) for each source having 9 grid points explained in step 2. Hence for each source, we will get one age value corresponding to $(T_{eff}, \log L)$ and 8 age values for the rest of the grid. These 8 age values standard deviation will give the sigma value for the age.

Chapter 3

Multi-Wavelength Data and Reduction Procedure

This project involves the photometric study of the region of interest in 12 filters, covering the optical, NIR and MIR wavelengths. The filters used and their details are listed in Table 3.1. Optical photometric data is retrieved from PS1 catalog for all five filters. For NIR, NEWFIRMs images are used and PSF photometry is carried out to get J, H and K band photometric data. Similarly in MIR, deep IRAC PBCD images are used for photometric analysis in 4 IRAC bands.

Table 3.1: Mean Wavelength and Bandwidth for all twelve filters used for this project

Filter	λ_{mean} (Å)	λ_{min} (Å)	λ_{max} (Å)
PanSTARRS (PS1)			
g	4900.10	3943.00	5593.00
r	6241.30	5386.00	7036.00
i	7563.80	6778.00	8304.00
z	8690.10	8028.00	9346.00
y	9644.60	9100.00	10838.00
NEWFIRM (NOAO)			
J	12511.50	11393.00	13612.00
H	16319.10	14575.00	18105.00
K	21451.70	19462.00	23480.00
Spitzer IRAC			
CH 1	35572.60	31296.00	39614.00
CH 2	45049.30	39173.00	50561.00
CH 3	57385.70	48983.00	65089.00
CH 4	79273.70	62994.00	95876.00

3.1 Optical data form PanSTARRS

Panoramic Survey Telescope and rapid Response System (Pan-STARRS)¹ is a system of astronomical imaging situated at Mount Haleakala, Hawaii on a 1.8 meter telescope of Ritchey–Chrétien telescopes type with 1.4 Gigapixel camera (GPC1) (Kaiser et al. 2010; Hodapp et al. 2004; Onaka et al. 2008). The instrument is equipped with five broadband filters (g,r,i,z,y) (Stubbs et al. 2010). Pan-STARR 1 is the first data release. The telescope used for Pan-STARR 1 survey has covers 7 square degree area of sky. Survey is done primarily towards north of -30° (Tonry et al. 2012). This has 60 orthogonal transfer arrays. This survey has been carried out in two parts, 3π steradian survey and medium deep survey. Image processing is done by PS1 Image processing pipeline (IPP) (Magnier 2006). This pipeline also does photometry (Magnier 2007) and automatic astrometry (Magnier et al. 2007). The calibration accuracy for photometric data is better than 1 % (Schlafly et al. 2012; Tonry et al. 2012). The filter profiles for the five filters are shown in Fig. 3.1. We have used data from the PS1 photometric catalog for this project.

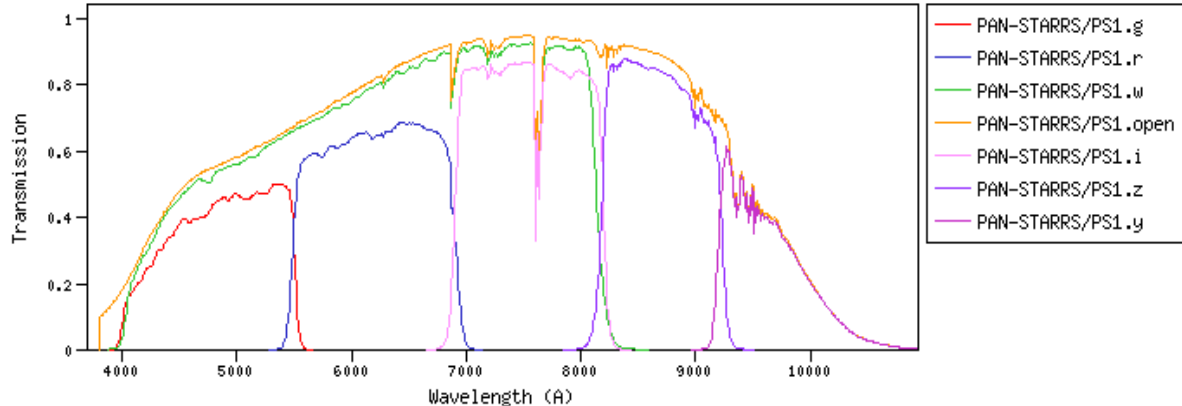


Figure 3.1: Pan-STARR filter profiles.

3.1.1 Source Selection

5σ depth in magnitude scale for all five filters of PanSTARR along with seeing is shown in Table 3.2. Depth of a survey is often given in integer multiples of observed standard deviation (σ) in data. The point source selection is done by taking $\sim 50''$ search in PS1 catalog available at ViZieR/MAST platforms keeping $\text{RA} = 02^h 30^m 00^s$, $\text{Dec} = 60^{\circ} 35' 0''$ as

¹The online catalog can be accessed from catalogs.mast.stsci.edu/

Table 3.2: Pan-STARR PS1 5σ depth and seeing

Pan-STARR Filters	5σ depth (mag)	Median Seeing (arcsec)
g	23.30	1.31
r	23.20	1.19
i	23.10	1.11
z	22.30	1.07
y	21.30	1.02

center. In addition to this, we have only retained sources with g band magnitude less than 20.0 mag, hence all the sources beyond this limit have been removed. Also to limit the uncertainty, all the sources considered have magnitude error less than 0.20 mag in all five filters. All the point sources included in the catalog are matched with rest of the filter data by procedure given in 3.2.5.

3.2 Near Infrared Data

3.2.1 NEWFIRM data

Near Infrared Observation has been taken by NEWFIRM instrument on 2009-11-14. NEWFIRM, the National Optical Astronomy Observatory (NOAO) Extremely Wide Field Infrared Imager, images a 28×28 arcmin² field of view on the NOAO 4-m telescopes. It covers a wavelength range of 1 - 2.4 microns with plate scale 0.4 arcsec/pixel. It was offered on the 4-m Mayall telescope on Kitt Peak through April, 2009. It is currently operating on the 4-m Blanco telescope on Cerro Tololo. The detector focal plane consists of four 2048 x 2048 arrays arranged in a 2 x 2 mosaic. We have used images in three bands, J filter (1.3 micron with bandwidth 1048.4 nm, FWHM 160.6 nm), H filter (1.5 micron with bandwidth 1555.7 nm, FWHM 174.7 nm) and K filter (2.2 micron with bandwidth 2165 nm, FWHM 257nm) for our study. The filter profiles for NEWFIRM are shown in Fig. 3.2.

3.2.2 Source Detection

The initial process involves source detection which is carried out using the DAOFIND task of IRAF v2.16 APPHOT package. The average full width at half maximum (FWHM) of point spread function (PSF) was estimated using 30 bright unsaturated point sources. To estimate the background, several regions were selected. Care was taken to ensure that there

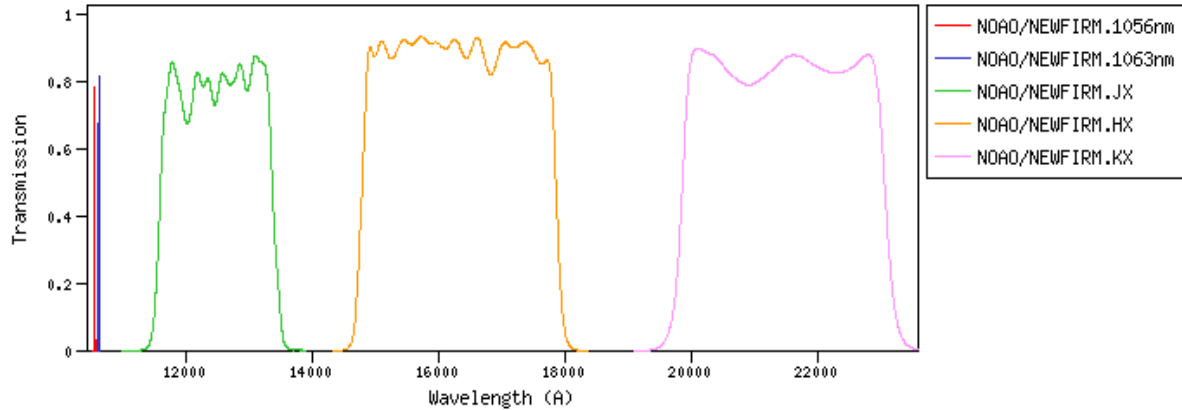


Figure 3.2: NEWFIRM filter profiles

is no contamination from bright sources. A threshold of 3σ was set for source detection, σ being the average standard deviation of the background regions selected. With these parameters (FWHMPSF = 2.2; σ = 0.7; Threshold = 3), 31835 sources are detected in the K-band image.

3.2.3 Aperture Photometry

In aperture photometry, a point source is marked by an aperture of few time of its FWHM (usually 2-3 times of FWHM). After that an annulus is marked over the source to estimate the background value which is further subtracted from apertures value. Using this method, the magnitude and its uncertainty is calculated. Since there are many crowded regions in the field of view, hence the results of aperture photometry are insufficient for our study. We have done PSF photometry for all three filters using the results of aperture photometry as initial values for tasks like psf and allstar.

3.2.4 PSF Photometry

While doing photometry on crowded star fields, such as globular clusters or open clusters, aperture photometry will not yield reliable results. In such cases, PSF photometry yields better results. PSF photometry involves modelling the PSF by using appropriate number of bright stars. This modelled PSF is then fitted with different available functions (e.g. gaussian, lorentz moffat15, moffat25, penny1, penny2). As an initial guess of magnitude values, results of aperture photometry are used. Output of psf task is the model PSF file which fits the model PSF to all stars in field. Subsequently, task ALLSTAR is used to determine the

x,y coordinates, sky values, and magnitudes for the stars by fitting the modelled PSF to all stars in the image. Performing ALLSTAR results in rejection of some stars which do not fit the model psf well enough. That's why we get different number of photometric result in all three filters. Out of 31835 point sources identified using DAOFLUX, 29766 point sources converged after ALLSTAR in K filter. Similarly 29048 point sources for J filter and 29261 point sources for H filter get converged. Fig. 3.3 shows the magnitude versus error plot for all three filters. These plots include only those sources which have magnitude estimates in all three filters.

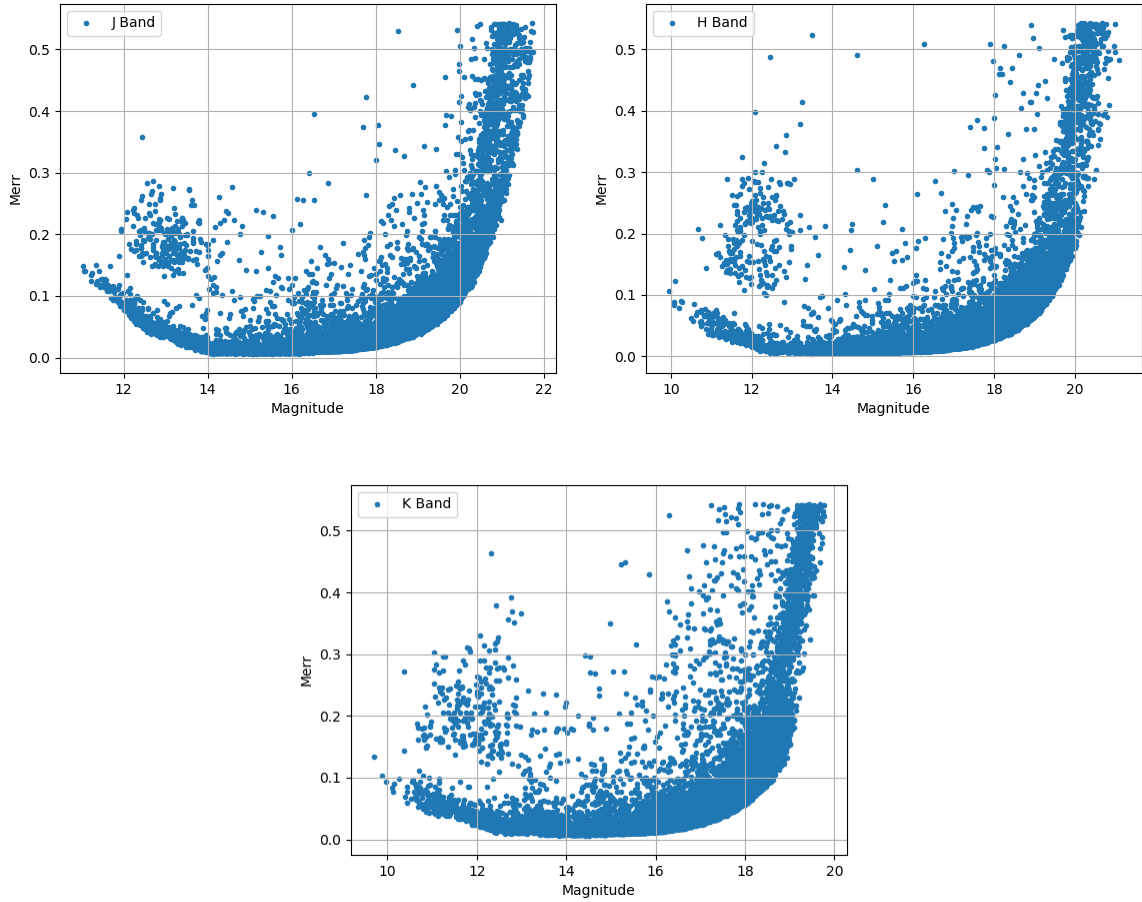


Figure 3.3: Magnitude versus error plots for NEWFIRM JHK photometry. The horizontal axis is magnitude in J band (top left), H band (top right) and K band (bottom). The vertical axis shows error in magnitude (merr).

3.2.5 Source Association

Since the number of point sources in all three filter photometry are different, it is important to cross-identify sources in the three filters. To do this, we use the ‘astropy’ package and generate a python script. The basic procedure for the cross-identification algorithm is to find the distance of each source in a filter with respect to all sources in other filter. The criterion for cross-identification is that the distance should be equal to the size of one pixel or it is comparable with the seeing of the observation. Following this a NEWFIRM catalog is generated which includes more than 28500 point sources with photometric data in JHK band.

3.2.6 Calibration and Catalog Merger

3.2.6.1 Calibration of NEWFIRM catalog

Our NEWFIRM catalog is calibrated by 2MASS² photometric data (Skrutskie et al. 2006). Online available photometric data of 2MASS for the same field of view (~ 30 arcmin cone) with error constraint ($\text{merr} < 0.1$) and magnitude constraint ($13 < \text{mag} < 15$) is fetched. The magnitude constraints are given because in NEWFIRM image, point sources brighter than about 11-12 mag are close to saturation or saturated. Whereas in case of 2MASS survey, as the magnitude of point source approaches to values faint as 18 mag, the error in observation rapidly increases. To do the calibration, magnitude range of 13-15 mag from both the catalog are used to plot the distribution of difference in magnitude for all filters. This is done after carefully identifying the source counterpart in 2MASS catalog using the same approach discussed in section 3.2.5. The distribution histogram with 50 bins and its Gaussian best fit is shown in Fig. 3.4. The offset values in NEWFIRM catalog is calculated from Gaussian best fit. Mean values and Sigma values for all the distribution is shown in Table 3.3. Also the similar distribution is plotted for all three colours (J-H), (H-K) and (J-K) and that is shown in Fig. 3.5. Since the color offset tends to zero for all three filters, hence we have not given any color correction.

3.2.6.2 Catalog merger (2MASS and NEWFIRM)

Two telescopes used for observation by 2MASS and NEWFIRM are having 1m and 4m aperture. Because of that in case of 2MASS data, point sources bright enough (10 mag or less) are unsaturated and have very less photometric uncertainty. In contrast with this, for

²Catalog can be accessed at <https://irsa.ipac.caltech.edu/Missions/2mass.html>

Table 3.3: Estimated magnitude offsets with respect to 2MASS photometry.

Filter	δMag (2MASS-NEWFIRM)	Standard Deviation σ
J	0.0591	0.098
H	-0.0964	0.079
K	-0.0331	0.086

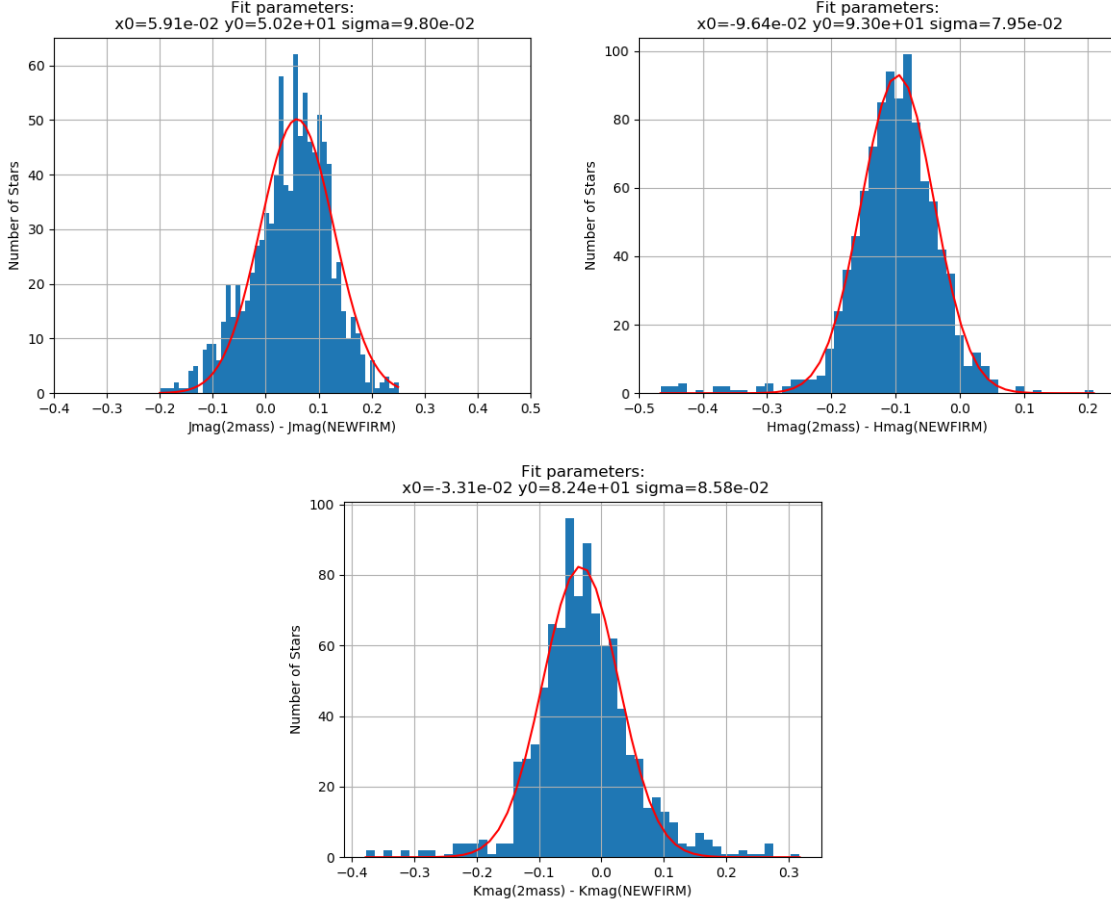


Figure 3.4: Distribution of magnitude difference between NEWFIRM and 2MASS. The Gaussian fit is shown in red with mean and standard deviation is given at top of each panel.

NEWFIRM, the point sources faint enough (17mag or more) shows good accuracy. Hence this study bounds to use mixture of data from both the observations. The cut-off/saturation limit set for the merger of two catalogs is 13 mag. Hence point sources brighter than 13 mag in NEWFIRM are discarded and point sources fainter than 13 mag in 2MASS are discarded. The rest of the point sources in both the catalog are merged to make a complete catalog. All the source with $\text{merr} > 0.20$ mag is ignored.

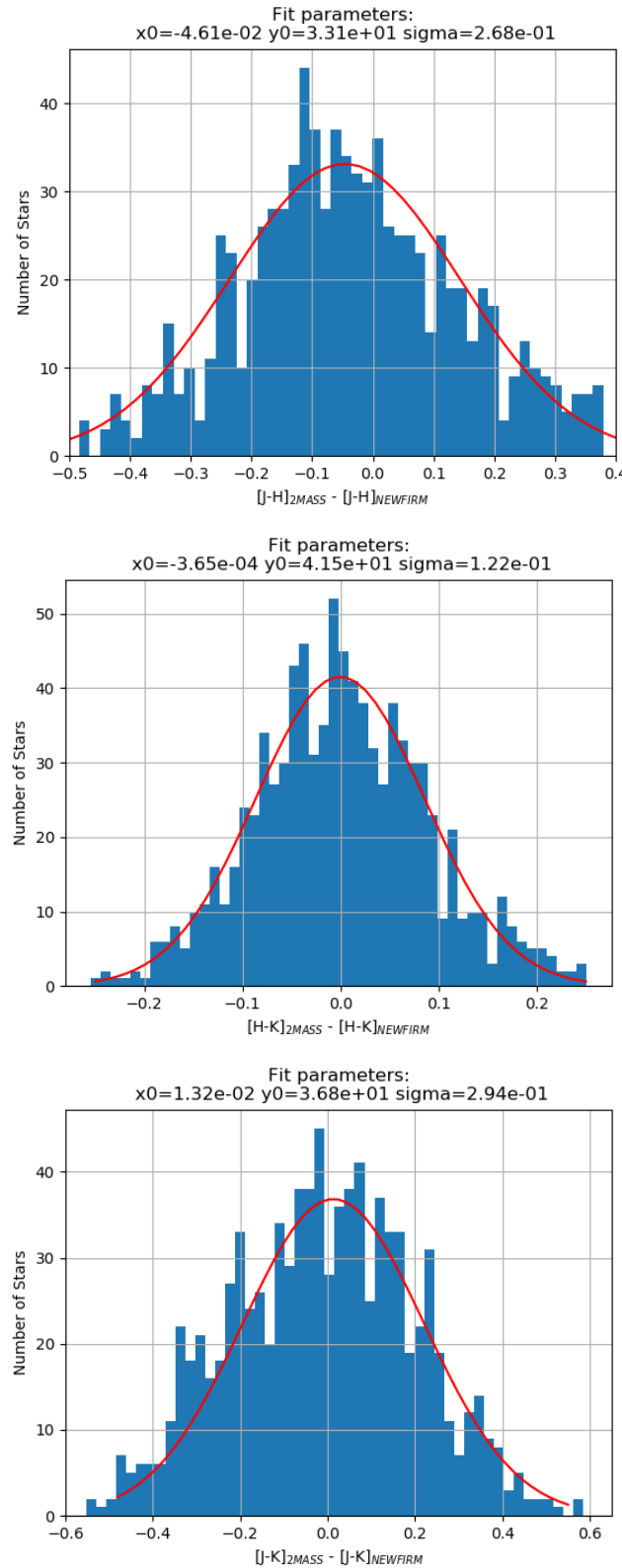


Figure 3.5: Distribution of color difference between NEWFIRM and 2MASS. The Gaussian fit is also shown in red with mean and standard deviation mentioned at top of each panel.

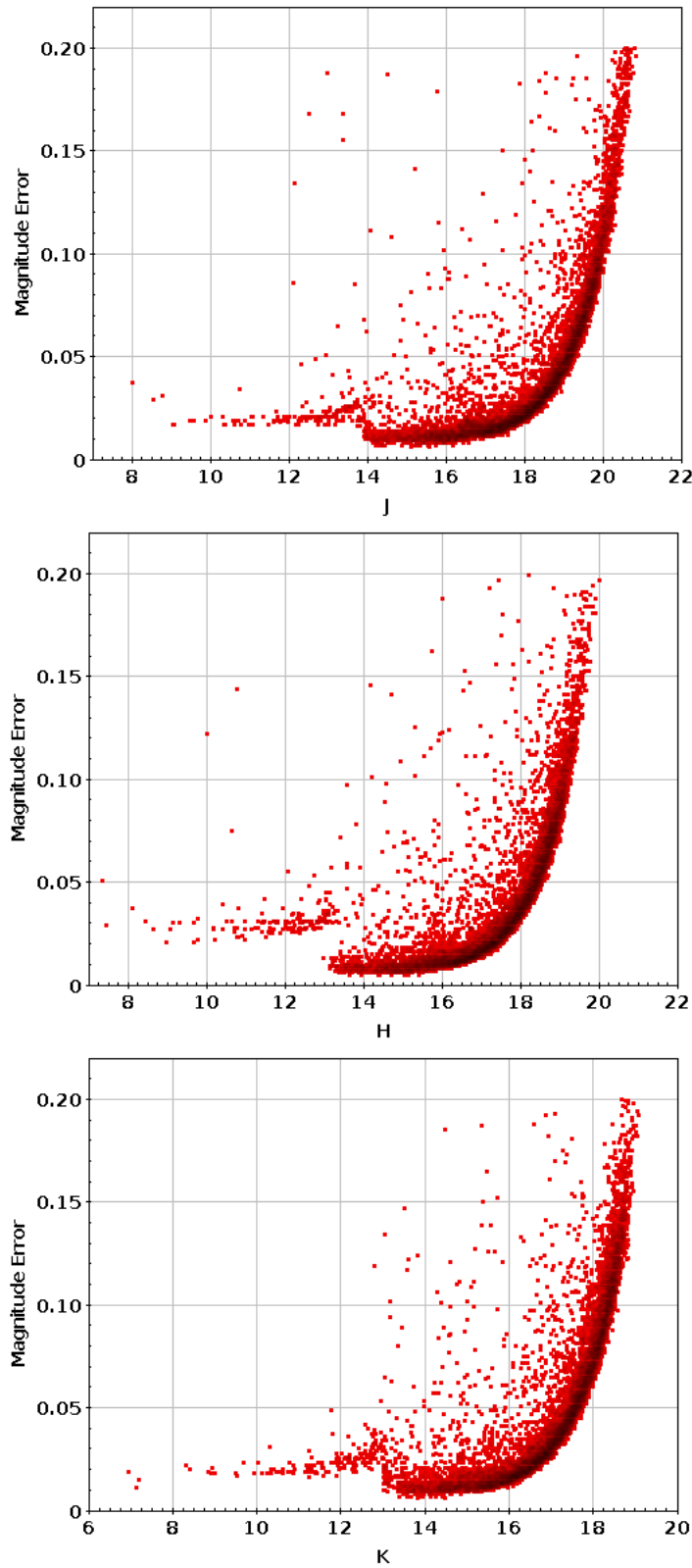


Figure 3.6: Magnitude versus error Plots for JHK filter of merged 2MASS-NEWFIRM catalog. For $K < 13$ mag, 2MASS data is plotted.

3.3 Mid-Infrared Data Reduction

Mid infrared IRAC band data are retrieved from the Spitzer archive (PI: Fazio, Giovanni, program id 201, AOR Key:6610688, observation date 2004-01-18). These observations were taken during the Spitzer cryogenic mission. Filter profiles of the IRAC bands are shown in Fig. 3.7. This project utilizes Post-Basic Calibrated Data (PBCD) product of Spitzer centers IRAC pipeline, they have been already processed as mosaics with dithering scale ‘medium’ and dither N-position equals to 3. These observations came with frame time of 12 sec for each channel. They have a plate scale of 0.6 arcsec/pix.

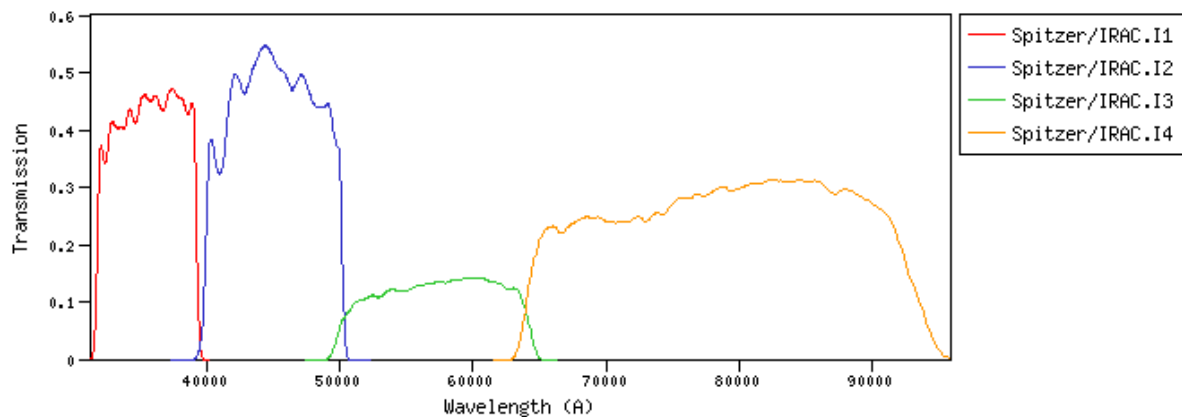


Figure 3.7: IRAC band filter profiles

3.3.1 MIR Source Detection

Following the same procedure as discussed in Section 3.2.5. Here, the average FWHM is estimated from 25 bright stars and the background is calculated in the same manner as discussed earlier. With these parameters (FWHMPSF = 3.75 ; σ = 0.025; Threshold = 3), 13443 sources are detected in the Channel 1 (3.6 μ m) image.

3.3.2 Aperture Photometry

As discussed earlier in Section 3.2.3, aperture photometry is carried out to get the initial values to perform PSF photometry. Result of aperture photometry were used for PSF photometry as initial guess.

3.3.3 PSF Photometry

Following the procedure given in Section 3.2.4, Out of the 13443 sources identified using DAOFIN, 8244 sources converged after ALLSTAR in Channel 1. Similarly, for 5299 sources in Channel 2, 7088 sources in Channel 3 and 4800 sources in Channel 4, the PSF model fit converged. Fig. 3.8 shows the magnitude versus error plot for all four IRAC bands. These plots include only those sources which are common in all four bands with $merr < 0.20$ mag.

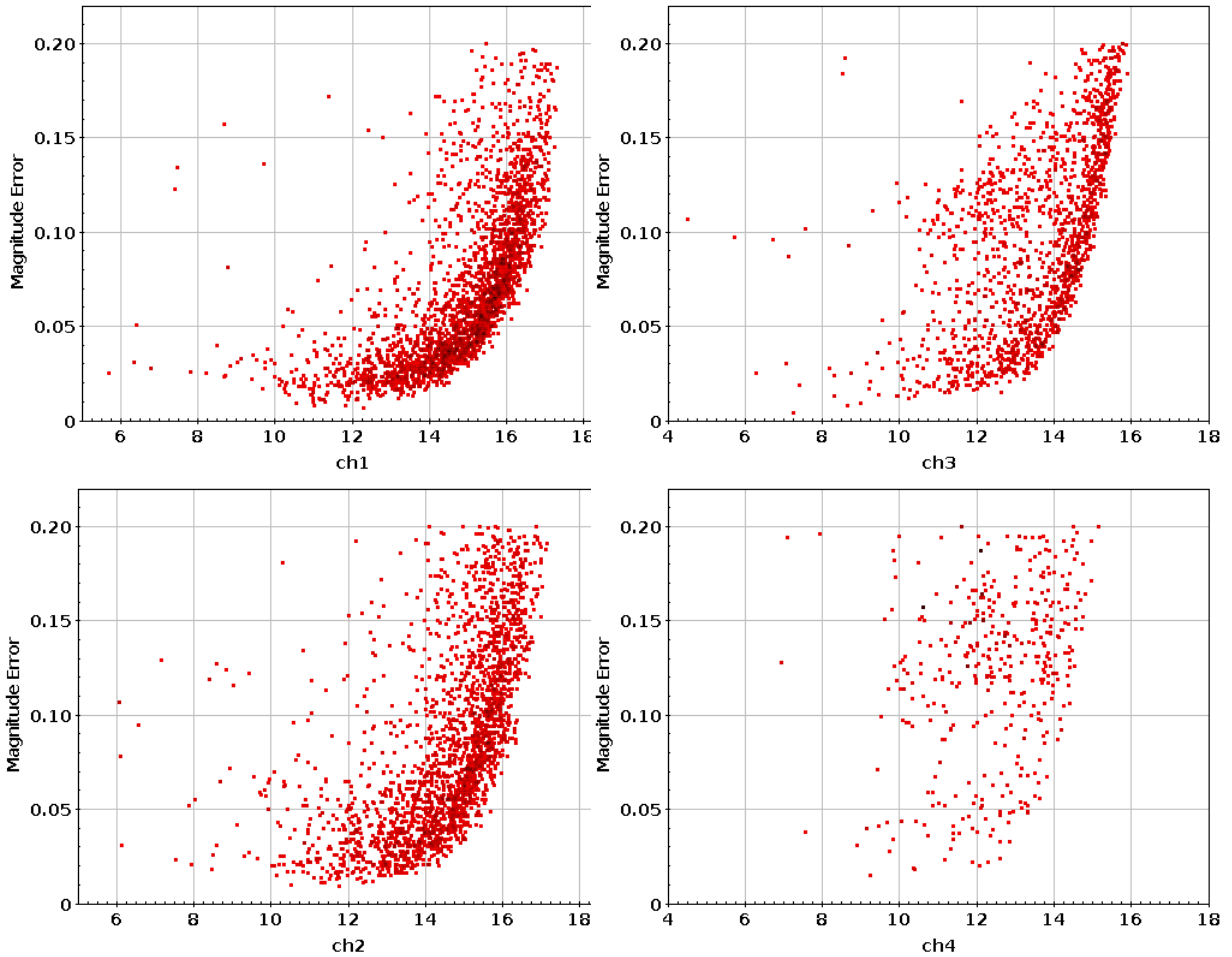


Figure 3.8: Magnitude versus error in magnitude plots for MIR IRAC bands. Channel 1 ($3.6 \mu\text{m}$) (top left), Channel 2 ($4.5 \mu\text{m}$) (top right), Channel 3 ($5.8 \mu\text{m}$) (bottom left) and Channel 4 ($8.0 \mu\text{m}$) (bottom right). Here, only sources with $merr < 0.20$ are shown.

3.3.4 MIR Source Association

Following the procedure from Section 3.2.2, MIR catalog is prepared which includes more than 12700 point sources photometric data in all IRAC bands.

3.3.5 Calibration and Catalog merger

Our MIR catalog is calibrated catalog given by Koenig et al. (2008) photometric data. This is done after carefully identifying the source counterpart in both the catalog using the same approach discussed in section 3.2.5. The distribution histogram with 50 bins and its Gaussian best fit is shown in Fig. 3.9. The offset values in MIR catalog is calculated from Gaussian best fit. Mean values and Sigma values for all the distribution is shown in Table 3.4. Sample catalog after matching NEWFIRM, Spitzer and Pan-STARR data by same procedure adopted in section 3.2.5 is given in Table 3.5.

Table 3.4: Offsets used for calibration

Filter	δMag ($Mag_{psf} - Mag_{koenig}$)	Standard Deviation σ
CH1	3.28	0.292
CH2	3.03	0.309
CH3	3.19	0.094
CH4	4.54	0.145

3.4 Combined Optical, NIR and MIR catalog

As given in Section 3.1, 3.2 and 3.3, we have done the photometry and calibration for NIR and MIR filters. In addition to this, we have take optical counterparts form PanSTARRS survey. NIR and MIR catalog made by the procedure given in Section 3.2.6.2 and 3.3.5 is used to merge with the third catalog form PanSTARR. This is carried out by the same merging procedure given in Section 3.2.5. Thus the final catalog obtained by merging all the three catalog is used for further investigation. In addition to this we have also excluded all the sources with magnitude error $merr > 0.20$ in our analysis. A small part of the final catalog is shown in Table 3.5.

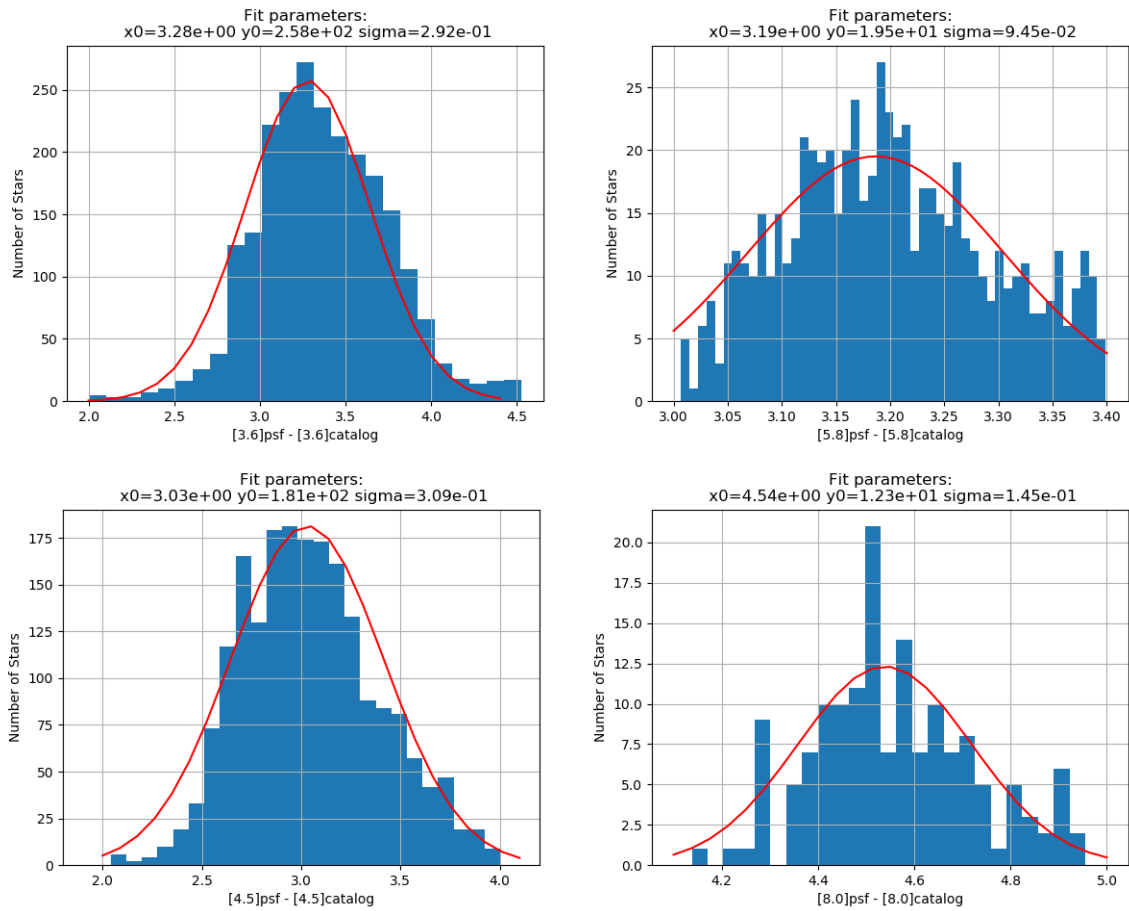


Figure 3.9: Distribution of offset for each MIR filter. Channel 1 (3.6 micron) (top left), Channel 2 (4.5 micron) (top right), Channel 3 (5.8 micron) (bottom left) and Channel 4 (8.0 micron) (bottom right). Offset is calculated from Koenig et al. (2008).

Table 3.5: Sample Catalog of BRC 13 and BRC 14 for NIR (J, H, K), MIR(CH1, CH2, CH3, CH4), Pan-STARR (g,r,i,z,y)

R.A._N	DEC_N	J	Je	H	He	K	Ke	ch1	ch1e	ch2	ch2e	ch3	ch3e	ch4	ch4e	g	ge	r	re	i	ie	z	ze	y	ye
45.16439	60.71191	10.989	0.017	10.773	0.023	10.624	0.018	11.012	0.042	10.641	0.076	10.873	0.068	13.036	0.231	12.727	—	12.347	—	12.149	—	11.984	—	11.902	—
45.57548	60.4964	11.048	0.021	10.769	0.028	10.62	0.02	10.619	0.045	11.201	0.243	10.867	0.058	13.539	0.148	13.425	—	12.802	—	12.43	—	12.13	—	11.9736	0.0067
45.59441	60.53952	11.086	0.021	10.192	0.027	9.939	0.018	—	—	10.026	0.043	—	—	—	—	—	—	—	—	—	—	—	—	—	—
45.17908	60.60609	11.093	0.017	10.913	0.024	10.829	0.019	10.682	0.022	10.49	0.035	10.701	0.032	12.038	0.327	12.84	—	12.444	—	12.194	—	12.029	—	12.0397	0.0005
45.5943	60.62307	11.35	0.021	10.986	0.027	10.906	0.02	—	—	11.128	0.048	—	—	—	—	—	—	—	—	—	—	—	—	—	—
45.24457	60.6005	11.495	0.017	10.701	0.026	10.466	0.019	10.115	0.022	10.078	0.02	10.251	0.012	12.091	0.187	15.9206	0.0029	14.5031	0.002	13.7255	0.001	13.2484	0.0047	12.9171	0.0022
45.60472	60.51123	11.601	0.019	10.637	0.031	10.332	0.018	—	—	—	—	—	—	—	—	—	—	—	—	—	—	—	—	—	—
45.25435	60.6572	11.607	0.018	10.83	0.023	10.532	0.019	10.307	0.02	10.027	0.02	10.37	0.033	10.423	0.044	16.3303	0.0026	14.8508	0.0022	14.0133	0.0033	13.4654	0.0025	13.098	0.0119
45.56343	60.6842	11.615	0.019	11.305	0.028	11.226	0.02	11.526	0.024	11.293	0.061	11.059	0.052	16.065	0.257	13.4357	0.006	13.364	—	12.975	—	12.5309	0.0032	12.694	—
45.49283	60.76231	11.691	0.023	11.429	0.035	11.298	0.026	—	—	—	—	—	—	13.9435	0.0031	13.262	—	12.961	—	12.713	—	12.6276	0.0068	12.7162	0.0022
45.5403	60.69967	11.703	0.021	11.325	0.031	11.196	0.021	11.505	0.03	11.269	0.047	10.984	0.044	—	—	14.1534	0.0031	13.4129	0.0022	13.137	—	12.887	—	12.6607	0.0029
45.33494	60.7552	11.719	0.021	11.403	0.03	11.24	0.016	11.685	0.03	11.456	0.066	11.639	0.091	—	—	14.2245	0.0004	13.5433	0.0045	13.234	—	12.89	—	12.6946	0.0117
45.43908	60.56224	11.73	0.019	11.404	0.026	11.317	0.02	11.001	0.015	10.859	0.032	11.158	0.015	14.502	0.245	13.8908	0.0046	13.088	—	12.862	—	12.737	—	12.694	—
45.46973	60.6246	11.786	0.019	10.988	0.031	10.782	0.023	10.545	0.009	10.382	0.063	10.596	0.028	14.189	0.255	16.0884	0.0032	14.6994	0.0021	13.9584	0.0007	13.4805	0.0019	13.1721	0.0023
45.18121	60.71848	11.791	0.018	10.993	0.022	10.734	0.019	10.803	0.022	10.7	0.079	10.93	0.073	12.852	0.048	16.1763	0.0027	14.7661	0.0034	14.0115	0.0011	13.5466	0.0022	13.207	0.0058
45.48626	60.7744	11.872	0.019	11.494	0.031	11.383	0.019	—	—	—	—	—	—	—	—	—	—	—	—	—	—	—	—	—	—
45.56286	60.65943	11.894	0.021	11.499	0.031	11.368	0.022	11.636	0.044	11.292	0.057	11.307	0.033	—	—	14.2814	0.0024	13.5946	0.0031	13.3328	—	13.024	0.0201	12.8799	0.0037
45.36104	60.57069	11.968	0.019	11.135	0.027	10.871	0.022	10.479	0.022	10.339	0.025	10.654	0.018	11.929	0.159	16.6412	0.0041	15.1183	0.0016	14.2975	0.0023	13.7992	0.0026	13.443	0.0008
45.17113	60.76148	11.97	0.018	11.624	0.025	11.567	0.022	—	—	—	—	12.243	0.098	—	—	14.0767	0.0016	13.496	—	13.218	—	13.0563	0.0052	12.9445	0.0013
45.31638	60.61672	11.98	0.018	11.672	0.025	11.541	0.021	11.223	0.011	10.987	0.029	11.479	0.027	9.671	0.043	14.3164	0.0032	13.739	0	13.38	—	13.1585	0.0031	12.9599	0.0032

Chapter 4

Analysis and Results

In order to understand the star formation process and young stellar objects associated with the two BRCs of W5E star formation complex, an area of $\sim 265.15 \text{ arcmin}^2$ has been considered around the BRCs. The area so chosen ensures that majority of the detected MIR sources and the YSOs identified by Chauhan et al. (2011) are included. Care is also taken to exclude sources lying towards the edge of the NEWFIRM images where the S/N ratio is relatively poor.

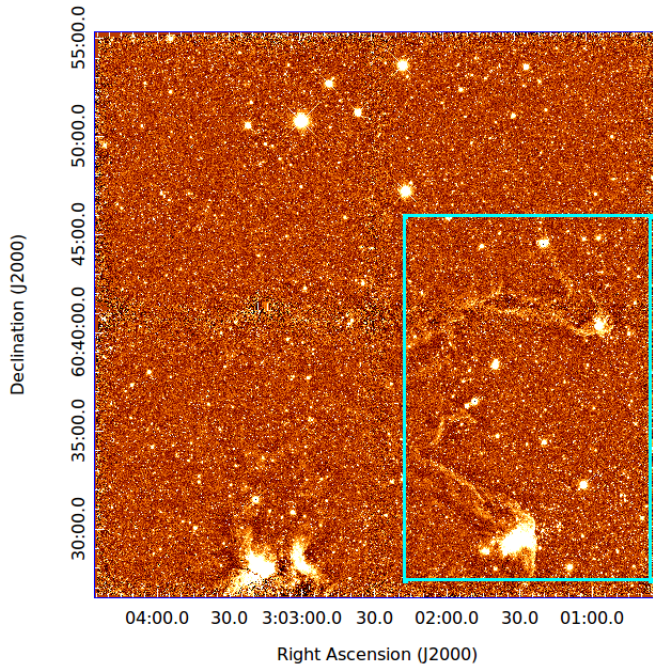


Figure 4.1: NEWFIRM K-band image showing BRC 13 and BRC 14 in the W5E star formation complex. The cyan rectangle denotes the area ($\sim 265.15 \text{ arcmin}^2$) considered for analysis.

4.1 Magnitude distributions and completeness limit

As explained in Sec. 3.2, photometry is done for 7 broadband filters in NIR and MIR. The magnitude distributions are shown in Fig. 4.2 and Fig. 4.3 for the NIR and MIR data, respectively. The magnitude distribution for optical data from PS1 PanSTARRS is shown in Fig. 4.4.

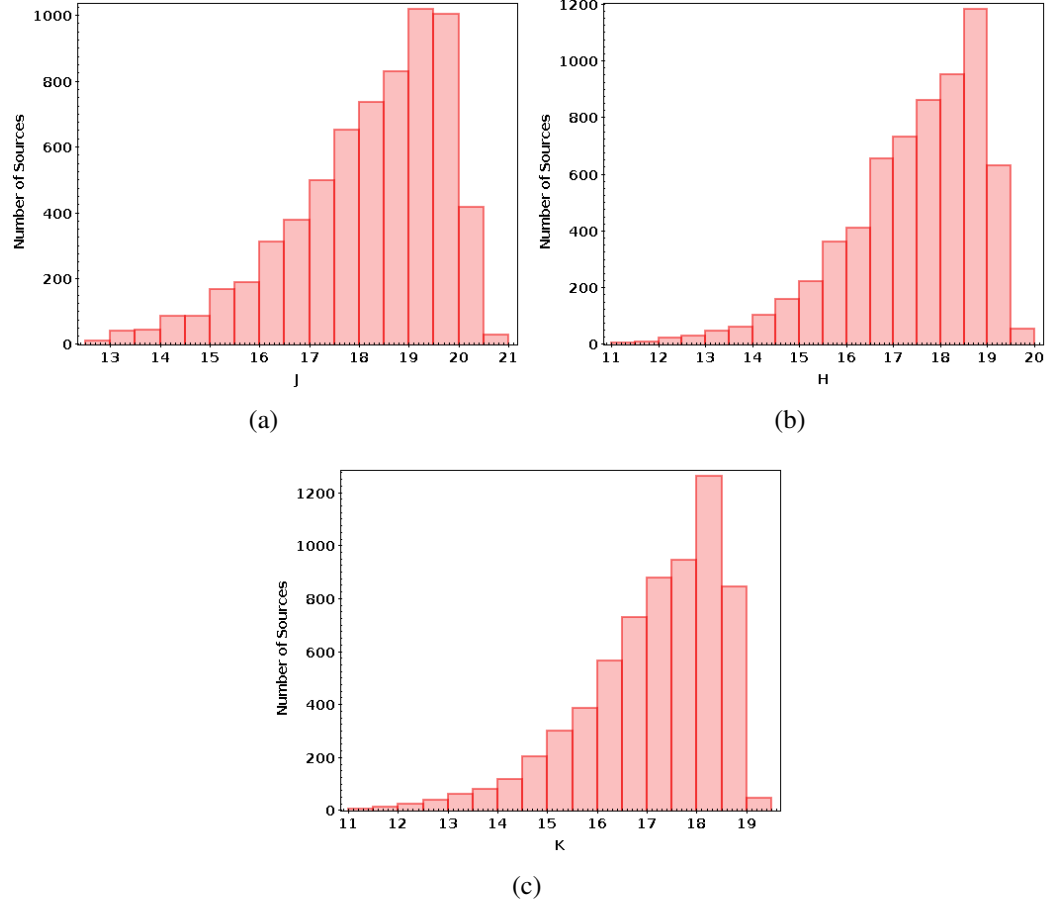


Figure 4.2: Histograms showing the magnitude distribution for the NEWFIRM NIR photometric data. (a) J band (1.2 μm), (b) H band (1.6 μm) and (c) K band (2.2 μm). The distribution is plotted for all sources within the box shown in Fig. 4.1.

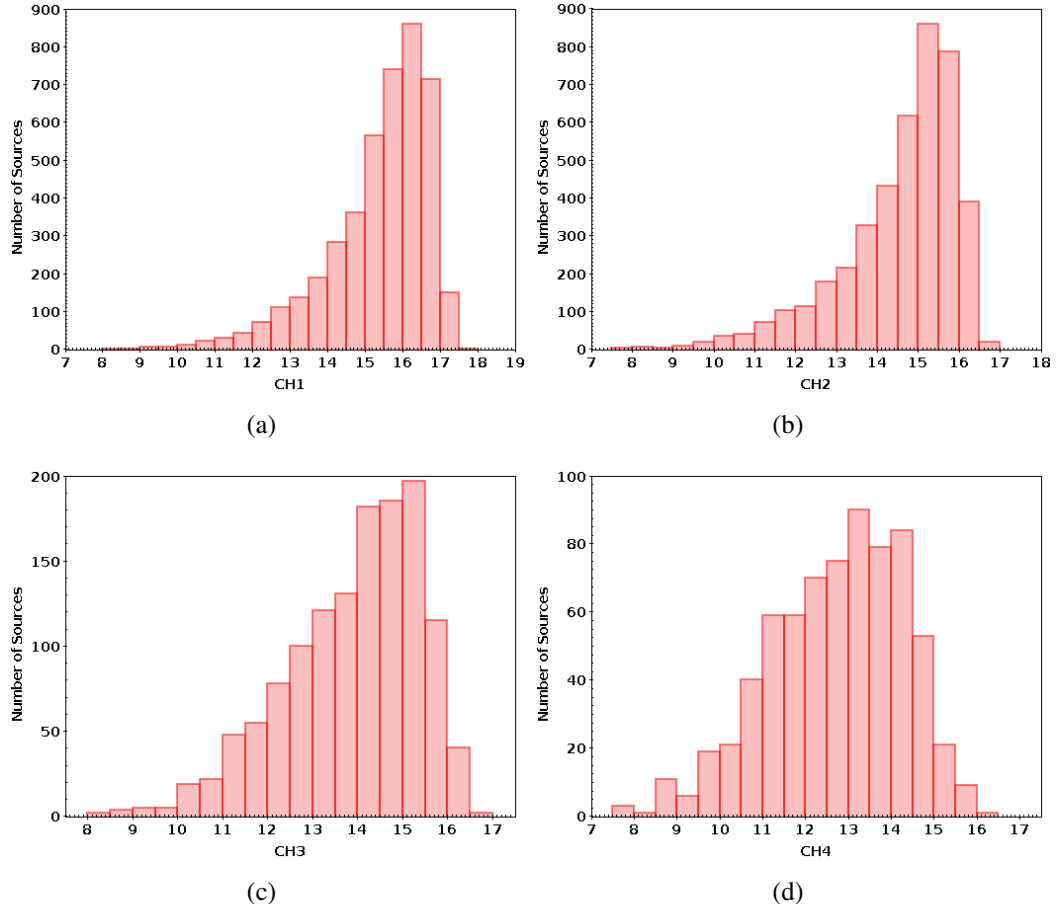


Figure 4.3: Histograms showing the magnitude distribution for Spitzer-IRAC MIR photometric data. (a) CH1 ($3.6 \mu\text{m}$) band, (b) CH2 ($4.5 \mu\text{m}$) band, (c) CH3 ($5.8 \mu\text{m}$) band and (d) CH4 ($8.0 \mu\text{m}$). The distribution is plotted for all sources within the box shown in Fig. 4.1.

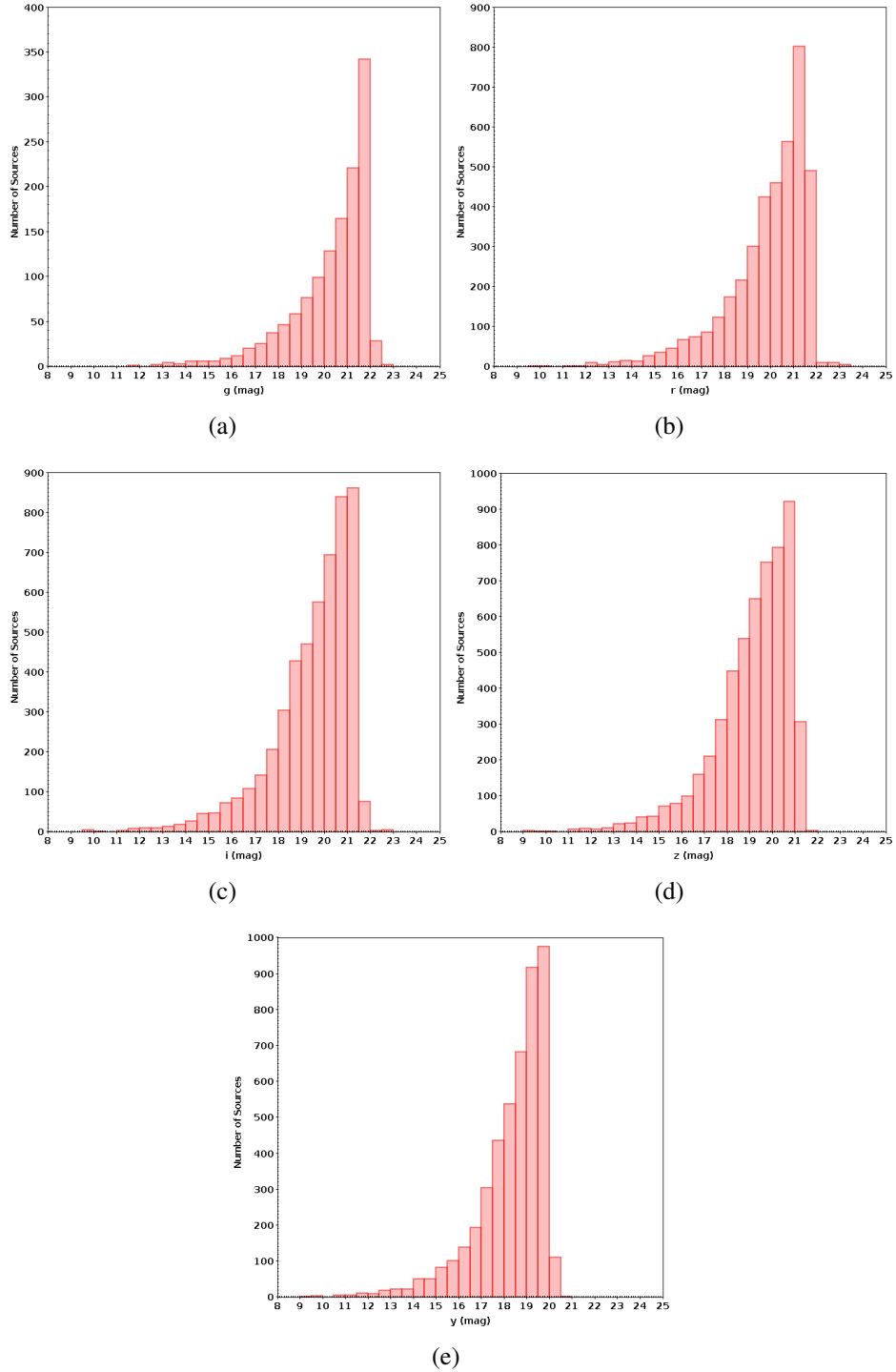


Figure 4.4: Histograms showing the magnitude distribution for PanSTARRS optical photometric data. (a) g ($0.49 \mu\text{m}$) band, (b) r ($0.62 \mu\text{m}$) band, (c) i ($0.75 \mu\text{m}$) band, (d) z ($0.87 \mu\text{m}$) band and (e) y ($0.96 \mu\text{m}$) band. The distribution is plotted for all sources within the box shown in Fig. 4.1.

For further analysis on star formation rate, IMF estimation etc, we consider those sources within 90% completeness limit which is given in Table 4.1. This completeness limit is calculated by using turn-over method discussed in (Ohlendorf et al. 2013; Samal et al. 2015; Dutta et al. 2018). The $\sim 90\%$ limit is considered at that magnitude at which the number of sources can not be shown as power-law. This magnitude is the turnover from the peak of the histogram.

Table 4.1: Estimated completeness limits (90%) in the twelve photometric bands.

S.No.	Filter	λ (μm)	90 % Completeness limit (mag)
1.	g	0.49	21.90
2.	r	0.62	21.65
3.	i	0.75	21.40
4.	z	0.87	20.95
5.	y	0.96	20.10
6.	J	1.20	19.75
7.	H	1.60	18.70
8.	K	2.20	18.30
9.	CH1	3.60	16.80
10.	CH2	4.50	15.85
11.	CH3	5.80	15.20
12.	CH4	8.00	13.71

4.2 Extinction Estimation

As given in section 2.1, there are various method to probe the extinction. Using the measured extinction map, sources are dereddened and these dereddened point sources are used for identifying the YSOs and then Classify them (see Section 2.2). By calculating reddening for each source in our region, we used field stars to estimate the extinction map. In this section, we discuss the methods that have been used to estimate extinction towards our region of interest.

4.2.1 Using Column Density Map

As discussed in Section 2.1.1, visual extinction, A_V , can be determined from the estimated $N(H_2)$ values using the relation $N_{H_2} / A_V = 1.37 \times 10^{21} \text{ cm}^{-2} \text{ mag}^{-1}$. Using Herschel data, Deharveng et al. (2012) have generated and published the molecular hydrogen column

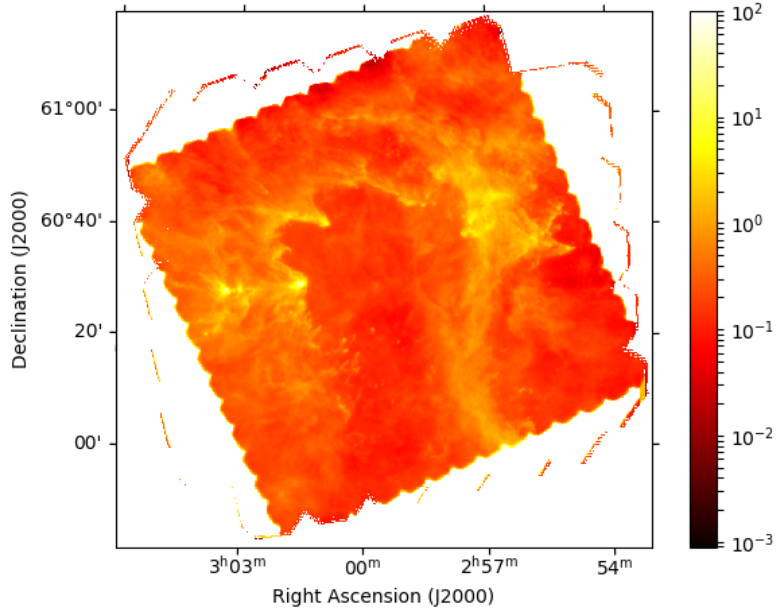


Figure 4.5: Extinction map prepared using column density map shown above using relation $N_{H_2} / A_V = 1.37 \times 10^{21} \text{ cm}^{-2} \text{ mag}^{-1}$.

density map for the W5E complex which harbours the two BRCs that are studied in this project. The corresponding extinction map is shown in Fig. 4.5. The extinction for sources are read out from the A_V map and the histogram of the extinction distribution is shown in Fig. 4.6. The histogram peaks around 0.35 mag. This seems to be lower if we consider typical foreground extinction of 1.0 mag/kpc and the distance of 2 kpc to this complex. As discussed by these authors, the maximum value of visible extinction $A_V = 96 \text{ mag}$ ($\approx N(H_2) = 9.0 \times 10^{22} \text{ cm}^{-2}$) along the line-of-sight towards BRC 14. Similarly the maximum value of visible extinction $A_V = 18.20 \text{ mag}$ ($\approx N(H_2) = 9.6 \times 10^{21} \text{ cm}^{-2}$) towards BRC 13. It should be noted that assumptions such as dust emissivity, gas to dust ratio, and dust opacity variation with wavelength have been included in constructing the column density map.

4.2.2 Using NIR and MIR photometry

Here we use the NEWFIRM JHKs and IRAC CH1 and CH2 photometry data to estimate the extinction. The details of the formalism adopted from Gutermuth et al. (2005, 2009) is presented in Section 2.1.3. The histogram of the estimated extinction is plotted in Fig. 4.7. As seen the histogram peaks at ~ 0.18 . Further, it is difficult to understand the negative extinction values obtained for around 65% of sources.

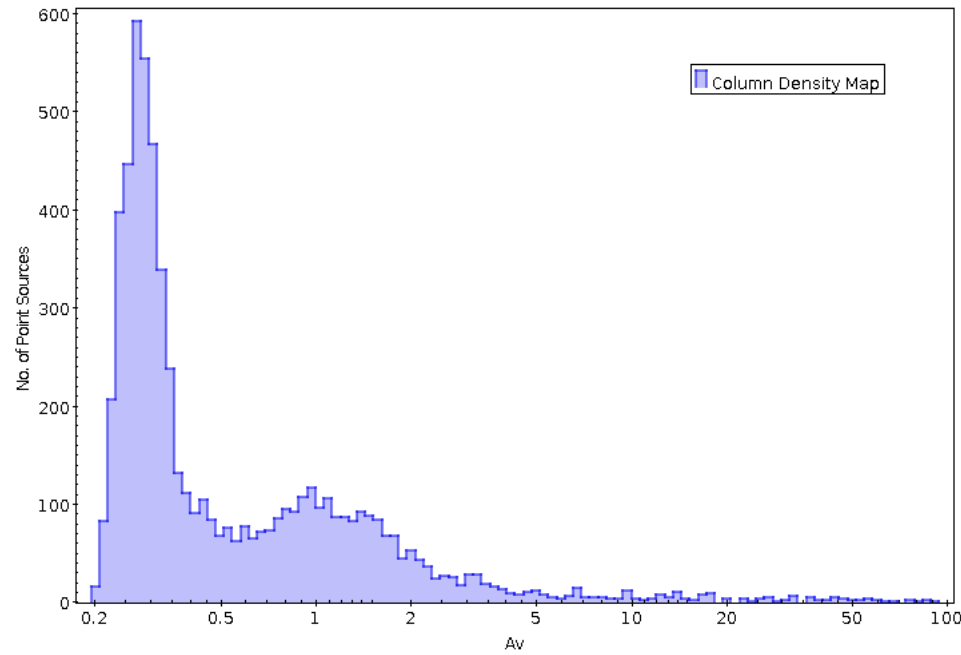


Figure 4.6: Histogram of estimated extinction based on the column density map for sources associated with BRC 13 and 14 and lying within the box shown in Fig. 4.1.

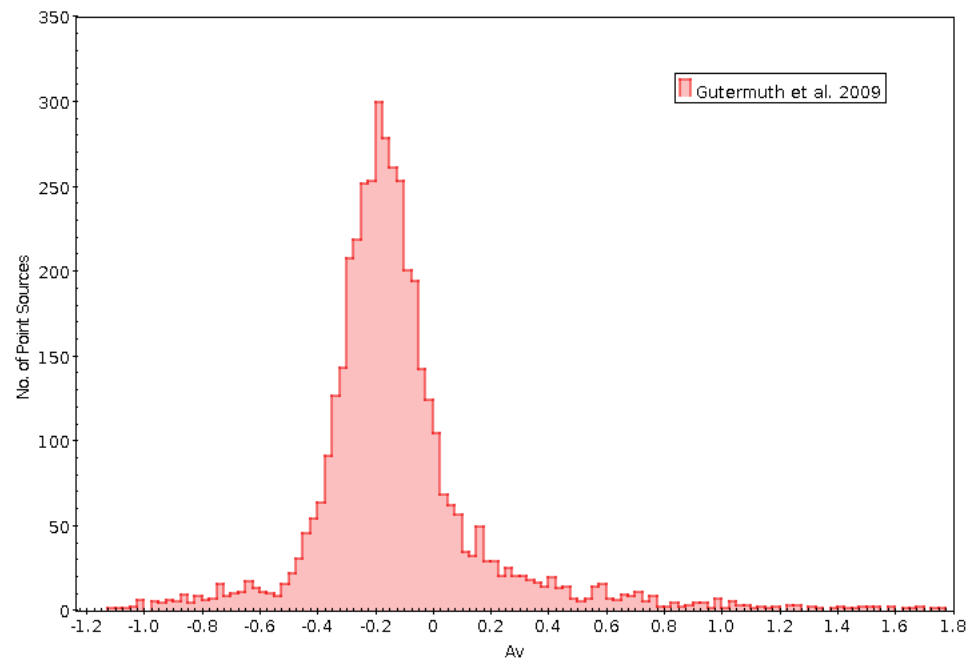


Figure 4.7: Histogram of estimated extinction based on the NIR and MIR photometry for sources associated with BRC 13 and 14 and lying within the box shown in Fig. 4.1

4.2.3 Using Field Stars

Following the method outlined in Pecaut & Mamajek (2013), extinction map is generated by dereddening the [H-Ks] colour of background stars to the nominal average intrinsic [H-Ks] colour of field stars, i.e., $A_K = 1.82 \times [(\text{H-K})_{\text{meas}} - (\text{H-K})_{\text{int}}]$, where $(\text{H-K})_{\text{int}} = 0.2$ is considered the average intrinsic color of field stars (Pecaut & Mamajek 2013).

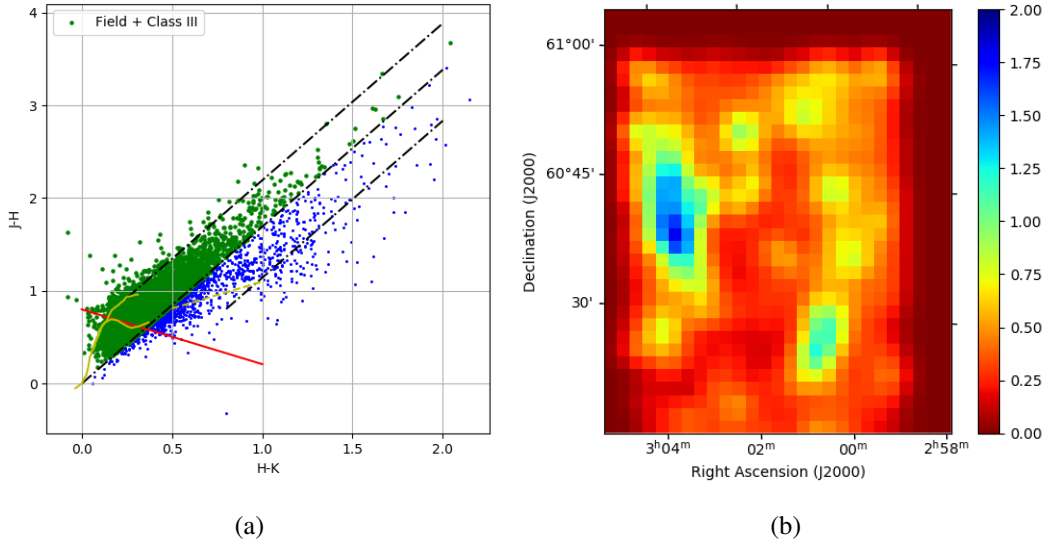


Figure 4.8: (a) CC diagram (J-H)/(H-K) for W5E HII from area shown in Fig. 4.1. The continuous curves shows the intrinsic locus of main sequence (below) and giants (above) (Bessell & Brett 1988). The dashed line represents the locus of intrinsic color of Classical T-Tauri (Meyer et al. 1997). The dashed-dotted lines are reddening vectors from (Cohen et al. 1981). Sources shown in green are field stars and Class III sources. (b) Extinction map of W5E HII region made by using the background field stars. The colorbar shows extinction in K-band i.e. A_K . The map has 265 arcmin² field of view and resolution of 1 arcmin.

The following steps are implemented to create the extinction map;

1. Field stars are identified using (J-H) versus (H-K) plot shown in Fig. 4.8(a). Field stars can be identified as sources falling leftward to the middle reddening vector, although, it is not possible to distinguish Class III and field stars, hence all the sources leftward to middle reddening vectors are considered.
2. For the identified field stars, extinction is calculated as $A_K = 1.82 \times [(\text{H-K})_m - (\text{H-K})_{\text{int}}]$ where, $(\text{H-K})_{\text{int}}$ is taken to be 0.2.

3. Smoothing of map is done by using a Gaussian kernel. The Gaussian used here has a thickness approximately equal to resolution of map (1 arcmin). Since the number of field sources close to the BRCs is low, it is difficult to increase the resolution of the map further without generating spurious extinction values especially near the BRC heads.

The extinction map is shown in Fig. 4.8(b). The FOV of the map is ~ 260 arcmin 2 and resolution is 1 arcmin. The maximum and minimum values of extinction estimated from this map are 0.02 mag and 1.5 mag in K band, respectively.

4.2.4 Using PNICER

We use the PNICER algorithm, discussed in Section 2.1.2, to generate the extinction map. For this the 2MASS Point Source Catalog is used and sources with ‘read-flag’ values of 222 are only retained. For the science field a ~ 280 arcmin 2 region centered on $\alpha_{2000} = 03^h 01^m 2.488^s$; $\delta_{2000} = 60^\circ 35' 16.98''$ is used. A region at $\sim 4.25^\circ$ west from W5E complex is chosen as the control field. It is centered on $\alpha_{2000} = 03^h 31^m 13.146^s$; $\delta_{2000} = 63^\circ 26' 26.51''$ and covers an area of ~ 100 arcmin 2 .

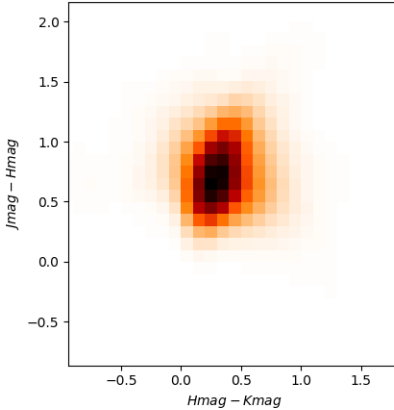


Figure 4.9: CC plot generated by PNICER. Horizontal axis is [J-H] color and vertical axis is [H-K] color. The data is taken from 2MASS Point Source Catalog.

The generated extinction map is shown in Fig. 4.11. The map shown has field of view of 0.5 deg 2 with the resolution of 0.5 arcsec. The color bar shown gives the A_V values. This map yields minimum and maximum A_V values of ~ 0.3 and ~ 10.60 mag, respectively and peaks at ~ 2.5 mag. The uncertainty as shown in Fig. 4.12 lies in the range 0.03 - 0.265 mag. The extinction determination from this method seems to be more reliable and for further analysis we use this.

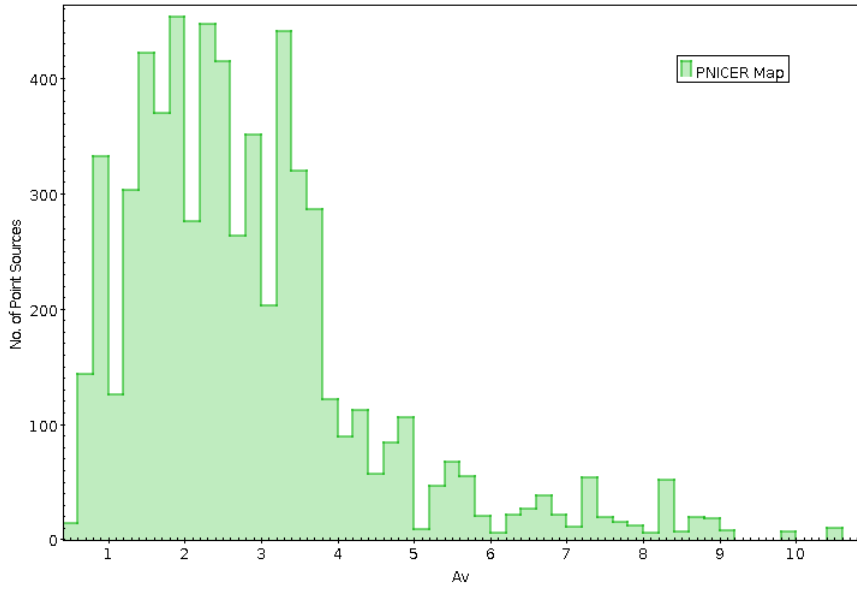


Figure 4.10: Histogram showing the distribution of extinction values, A_V , estimated using the PNICER method for all those sources falling in green box in Fig. 4.1. The extinction values are taken from PNICER map shown in Fig. 4.11.

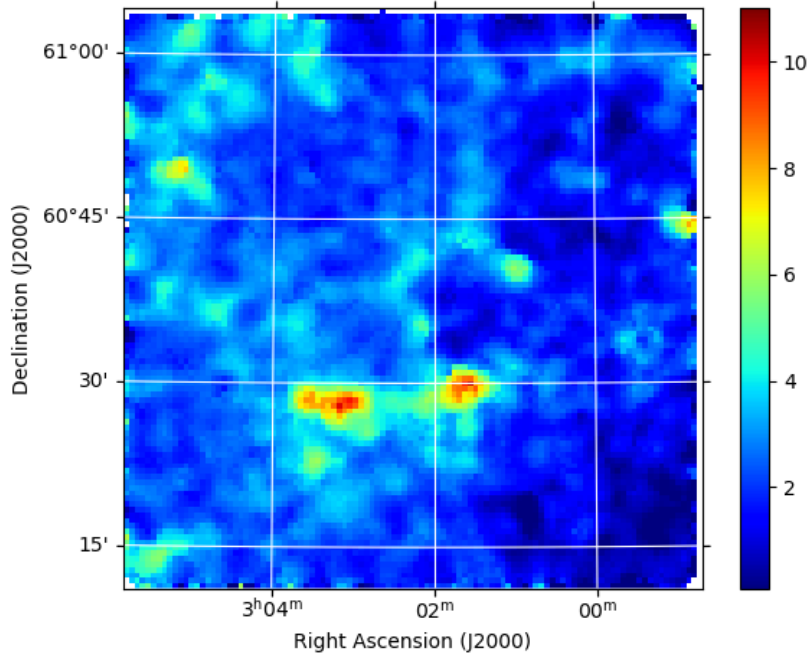


Figure 4.11: Extinction map generated by PNICER. The color bar shows the extinction values in V-band (A_V). The map shown has field of view of 0.5 deg² with the resolution of 0.5 arcsec.

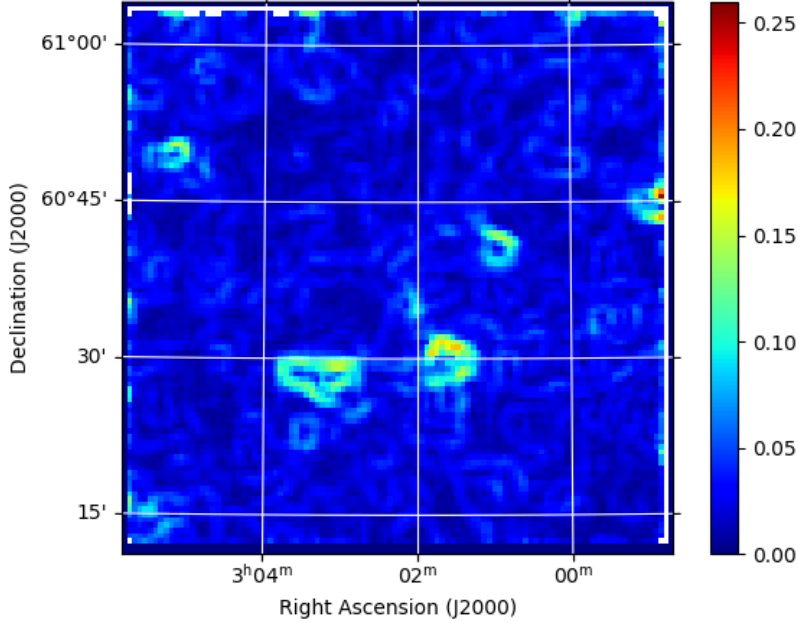


Figure 4.12: Extinction uncertainty map generated by PNICER. The color bar shows the extinction uncertainty values in V-band (σ_{AV}) which is calculated from PNICER map. The map shown has field of view of 0.5 deg^2 with the resolution of 0.5 arcsec .

The error map for extinction presented in Fig. 4.12 is constructed as per the following steps:

1. From the map generated by PNICER map, for each pixel, the 3×3 grid is selected. These nine values are used to make the uncertainty map. For every (i,j) pixel, there would be $(i-1,j)$, $(i+1,j)$, $(i-1,j-1)$, $(i+1,j-1)$etc. pixel values.
2. The standard deviation ($\sigma_{i,j}$) of this 3×3 grid is calculated. For all values of (i,j) , calculate the value of $\sigma_{i,j}$, except for the outer edge of the PNICER map. Hence for $(i \times j)$ pixels, it will give the standard deviation $(i \times j - 2(i+j))$ values.
3. Using all the values of standard deviation calculated from step 2, we generate a map performing convolution to each pixel value such that the uncertainty map should have the same resolution as the PNICER map.

4.3 Class I and II YSO identification

We consider sources detected in all [CH1], [CH2], [CH3] and [CH4] IRAC bands with an uncertainty less than 0.2 mag to identify Class I and Class II sources associated with

the region following the schemes described in detail by Gutermuth et al. (2005, 2009) (see appendix A, phase 1). Various non-stellar contamination, which include emission from features dominated by poly-cyclic aromatic hydrocarbons (PAHs), likely star-forming galaxies and weak-line active galactic nuclei, are eliminated using these schemes.

Fig. 4.13 displays the CC diagram of $[Ks - CH1]_o$ versus $[CH1 - CH2]_o$ showing the Class II (green) and Class I (blue) sources with field/Class III sources (red). The numbers of YSOs identified based in this method amount to 195 Class II and 14 Class I sources for the BRC 13 and BRC 14 region combined. The black line shown in Fig. 4.13 distinguishes Class I and Class II sources. These lines are drawn considering the average value of sigma for all sources (for more detail refer to section 2.3.2).

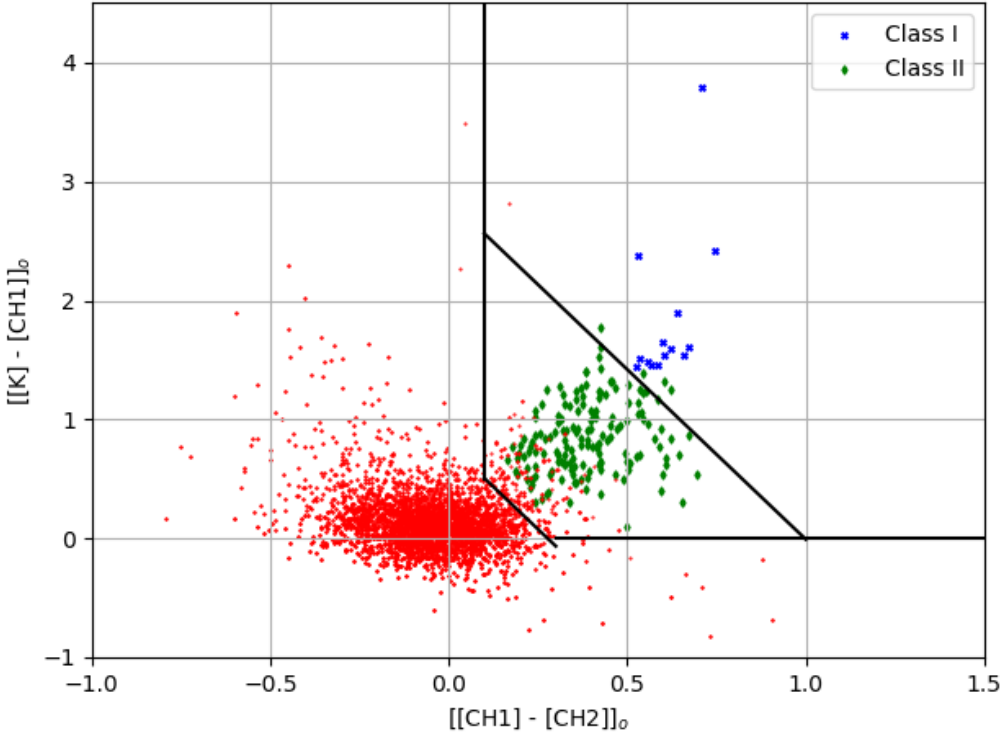


Figure 4.13: CC diagram of $[Ks - CH1]_o$ versus $[CH1 - CH2]_o$ showing the Class II (green) and Class I (blue) sources with field/Class III sources (red). The color cutoff are given in detail in section 2.3. The identification scheme is adopted from Gutermuth et al. (2005, 2009).

As we understand, the magnitude cut-off used in eq. 2.57 and eq. 2.59, is likely to be based on the depth of GLIMPSE-MIR data used by these authors. This basically enables the elimination of faint extra-galactic contaminants. For our study, we use the 90% completeness limit of 16.80 mag at $3.6\mu\text{m}$ (see table 4.1) to filter contaminants from Class I (protostars)

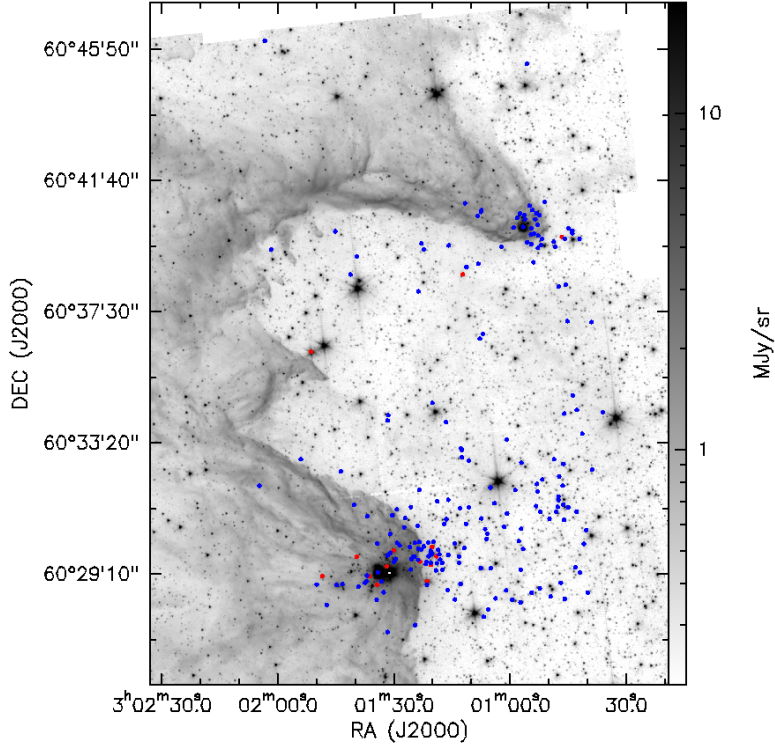


Figure 4.14: Spatial distribution of Class I/II sources identified in the region associated with BRC 13 and 14. Blue sources and red sources are Class II and Class I, respectively.

sources. For Class II sources, 0.5 mag brighter limit of 16.30 mag is used. The spatial distribution for Class I and Class II sources identified is shown in Fig. 4.14. As can be seen, the head of the BRCs show an over abundance of Class I and Class II sources.

4.4 SED Modelling and the HR diagram

The spectral energy distribution of the YSOs identified in section 4.3 are modelled using the online spectral energy analyzer VOSA. As discussed in Section 2.4 of Chapter 2, we use the ‘BT-Settl’ model, the parameter grid of which is shown in Table 2.2. Extinction values that are given as input to this model are taken from the map generated using the PNICER algorithm. Further, the same distance of 2100 ± 300 pc is assumed for all the sources.

The model fitted temperature (T_{eff}) and luminosity (L/L_{\odot}) are used to plot the HR diagram which is shown in Fig. 4.15. Histograms of the temperature and luminosity distribution are also shown in Fig. 4.16 and Fig. 4.17, respectively. The mean temperature is 4540 ± 150 K with minimum and maximum being 2600 ± 100 K and 10000 ± 100 K, respectively. The

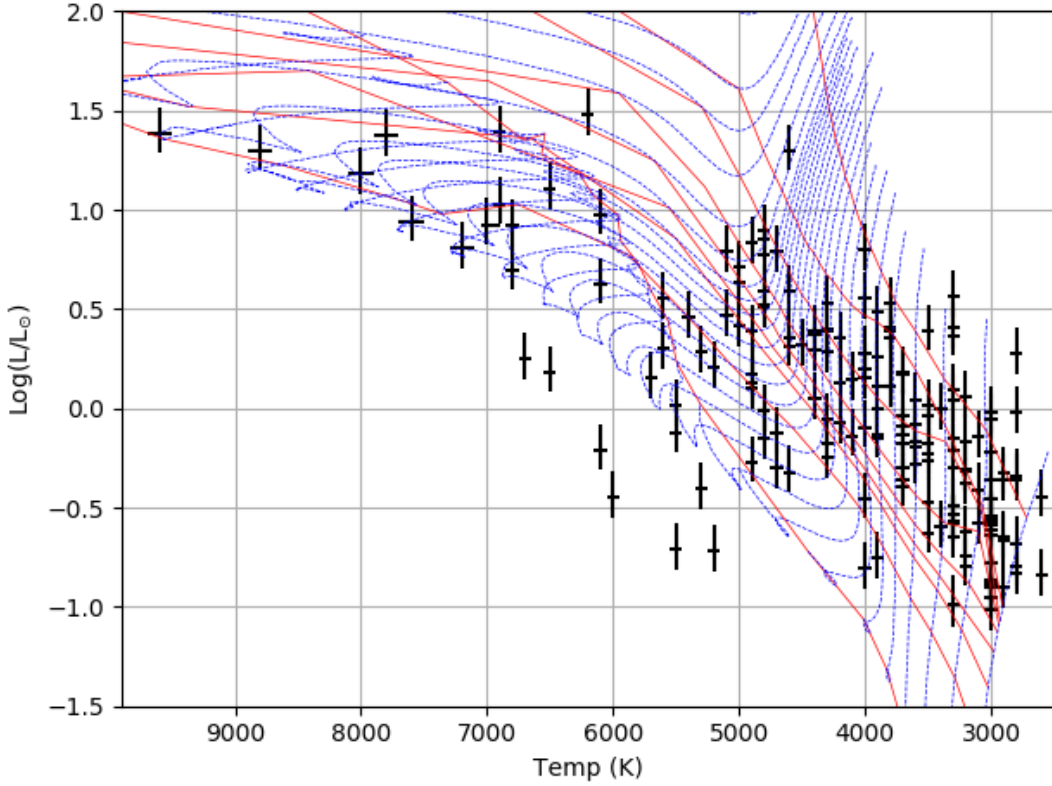


Figure 4.15: The HR diagram for YSOs (in black) identified in Section 4.3. The horizontal axis is temperature in K and vertical axis plots the bolometric luminosity (L/L_{\odot}) in log-scale. The red lines are the isochrones of 0.007 Myr (right most) till 10 Myr (left most). The blue dotted curves are the evolutionary tracks of mass $0.1 M_{\odot}$ (bottom most) to $30 M_{\odot}$ (top most). The isochrones and evolutionary tracks are taken from Siess et al. (2000).

luminosity distribution gives an mean of $0.128 \pm 0.112 L_{\odot}$. The minimum and maximum luminosity values are $0.097 \pm 1.41 L_{\odot}$ and $1629.29 \pm 1.34 L_{\odot}$, respectively. The determination of the other physical parameter is carried out following the discussion in Section 2.4 of Chapter 2. As discussed, to estimate the age, we need the age isochrones and to estimate the mass, we need the evolutionary tracks. For our analysis, we have used the age isochrones and evolutionary tracks from Siess et al. (2000). The age isochrones range from 0.07 Myr to 10 Myr and the evolutionary tracks range from $0.1 M_{\odot}$ to $30 M_{\odot}$. Since the central cluster age is ~ 5 Myr, hence only sources with age < 5 Myr are considered. The minimum age and maximum age obtained are 0.112 ± 0.008 Myr and 4.455 ± 1.722 Myr respectively. The minimum mass and maximum mass determined are $0.107 \pm 0.001 M_{\odot}$ and $2.842 \pm 0.18 M_{\odot}$ respectively. Histograms showing the age and mass distributions are plotted in Fig. 4.18 and Fig. 4.19 respectively.

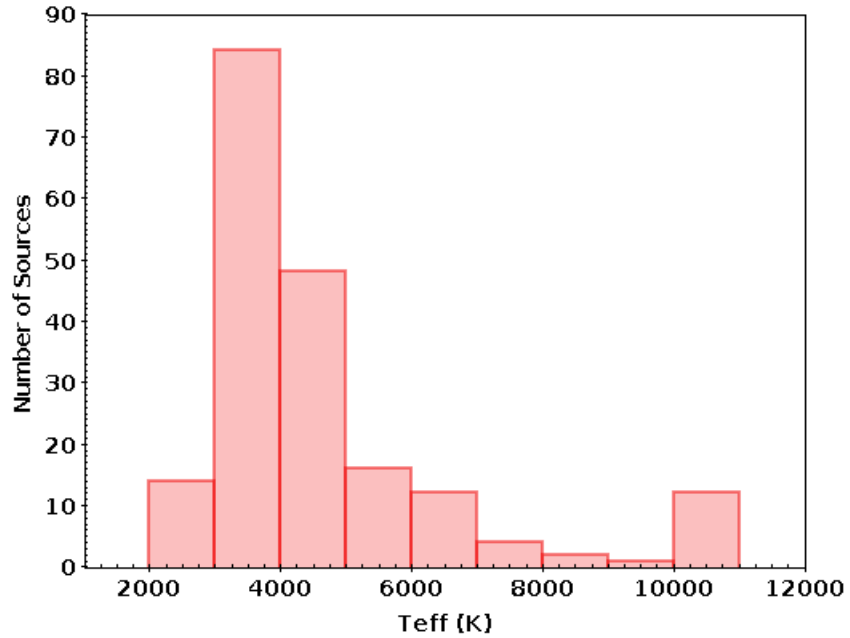


Figure 4.16: Histograms showing the temperature distribution for Class I and II sources for BRC 13 and BRC 14 combined. Bin size used is 1000 K. Mean temperature is 4540 ± 150 K, minimum and maximum temperature is 2600 ± 100 K and 10000 ± 100 K, respectively.

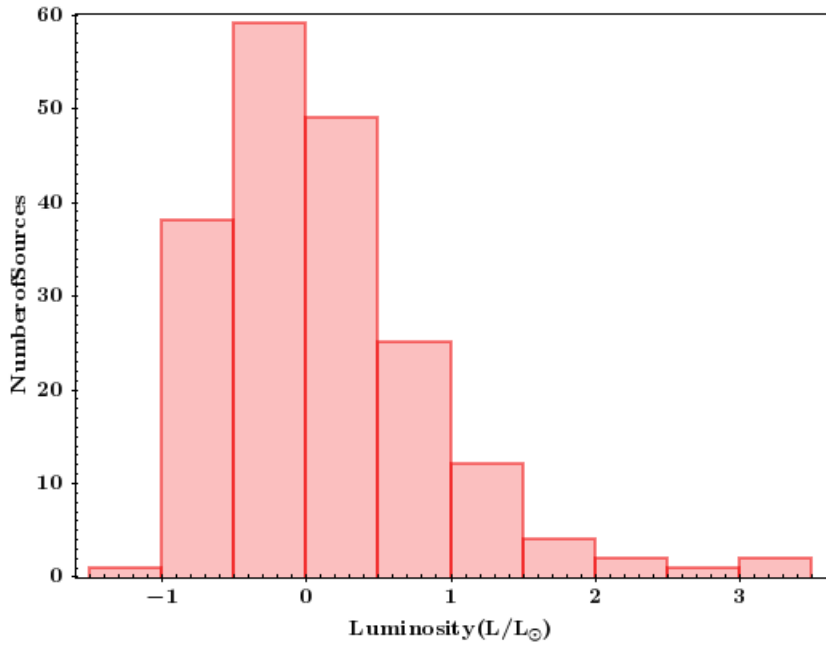


Figure 4.17: Histograms showing luminosity distribution for Class I and II sources for BRC 13 and BRC 14 combined. Mean of $0.128 \pm 0.112 L_{\odot}$. The minimum and maximum luminosity values are $0.097 \pm 1.41 L_{\odot}$ and $1629.29 \pm 1.34 L_{\odot}$, respectively. Bin size is taken as $0.5 L_{\odot}$.

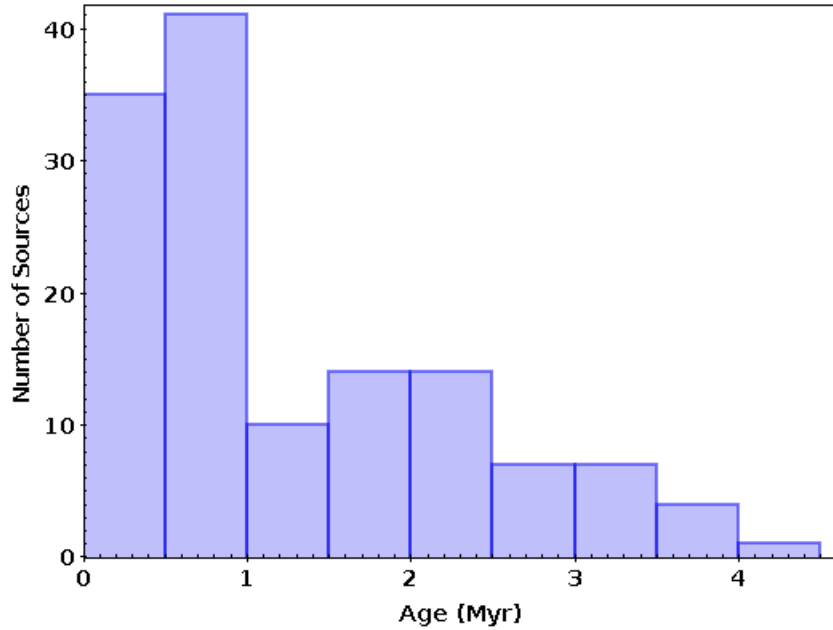


Figure 4.18: Histograms showing age distribution in Myr for Class I and II sources for BRC 13 and BRC 14 combined. The minimum age and maximum age obtained are 0.112 ± 0.008 Myr and 4.455 ± 1.722 Myr respectively. Bin size is 0.5 Myr.

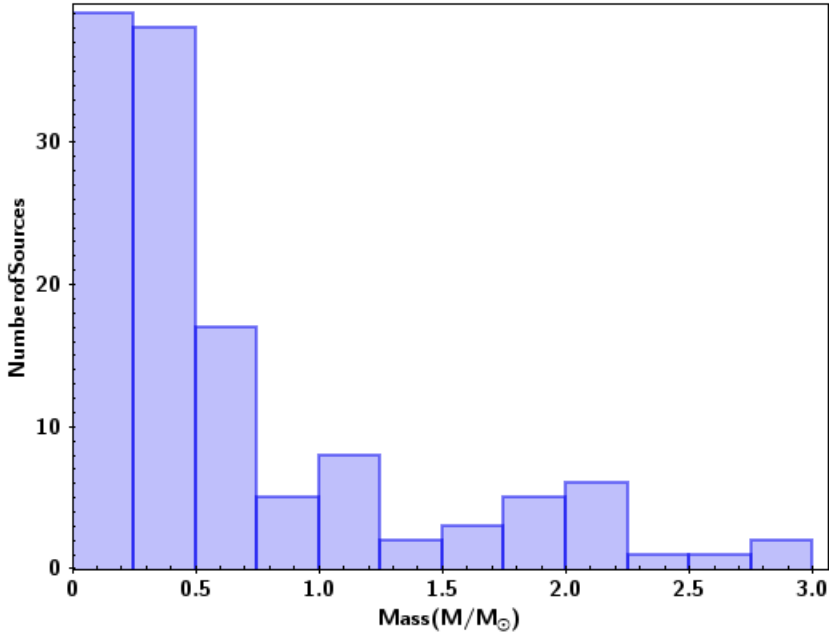


Figure 4.19: Histograms showing mass distribution for Class I and II sources for BRC 13 and BRC 14 combined. The minimum mass and maximum mass obtained are 0.107 ± 0.001 M_\odot and 2.842 ± 0.18 M_\odot respectively. Bin size for this plot is $0.25 M_\odot$.

4.5 Identification of Class III sources

In order to estimate the SFR and SFE, it is required to calculate the the total mass of all sources including Class I, Class II and Class III. For this, Class III sources also needs to be carefully identified. It is difficult to distinguish Class III sources from field sources, so the identification scheme used here is a multi-step process which uses combination of optical-NIR CMD plot and J versus [J-H] CMD plot.

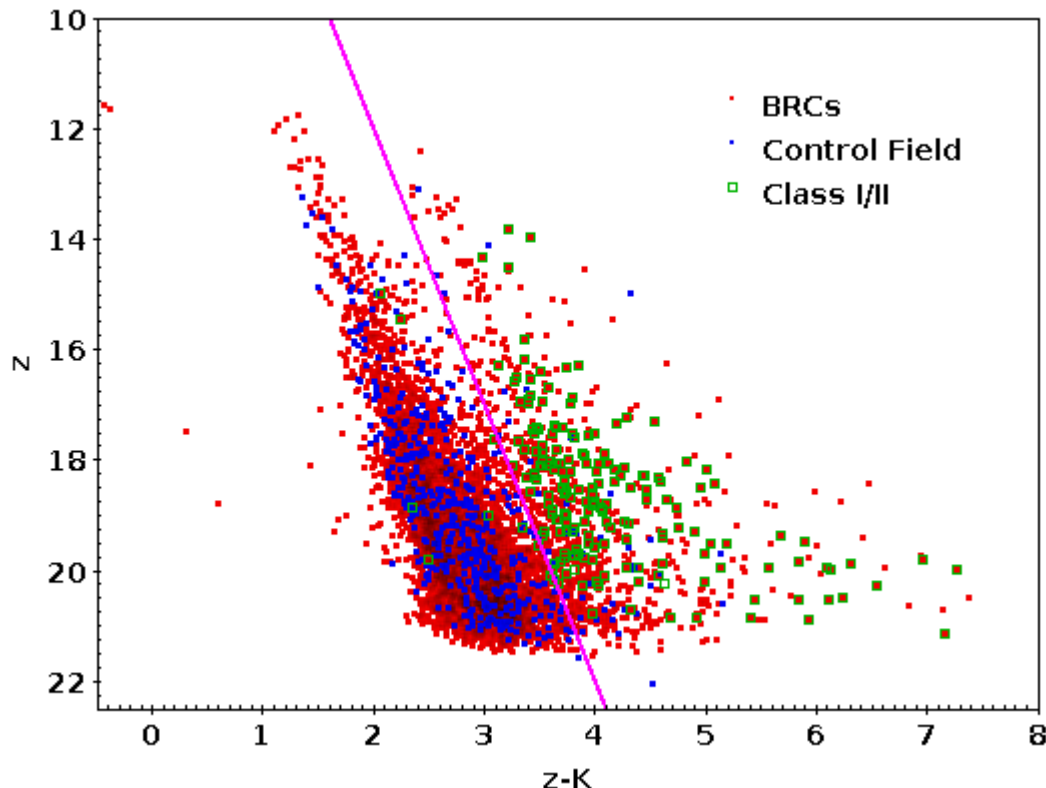


Figure 4.20: CMD plot showing [z-K] color on horizontal axis and z magnitude on vertical axis. This plot is foreground extinction corrected. The mean foreground extinction is assumed to be $A_V = 2.0$ mag. BRC sources falling inside the box shown in Fig. 4.1 are shown in red. Blue sources are the control field sources. The Class I/II sources identified in Section 4.3 are shown in green. Line shown in magenta is the empirical cutoff (eq. 4.1) to identify the initial set of likely YSOs.

The steps involved in identification of Class III sources are as follows;

1. All sources identified in Section 4.3 are plotted on optical CMD z versus [z-K] as shown in Fig. 4.20. Visual inspection of the CMD shows two distinct population of

sources. Based on this gap between the two population, an empirical cutoff is applied which separates the two population which is given by;

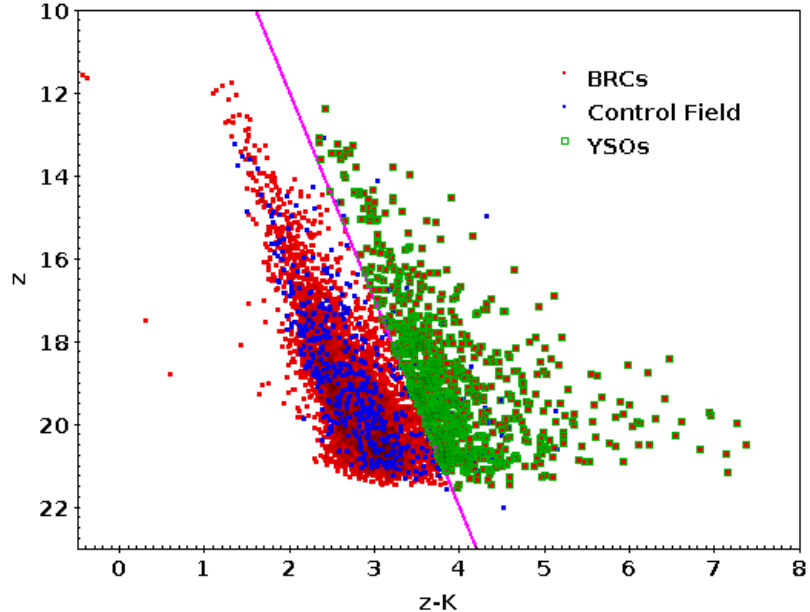
$$[z] < 5 \times [z - K] + 2.0 \quad (4.1)$$

A control field is considered which is assumed to have minimum reddening and abundant field stars. The control field has 53.20 arcmin^2 area with $\alpha_{2000} = 02^h 59^m 51.60^s$; $\delta_{2000} = 60^\circ 45' 36''$ as center. Sources falling rightward to the cutoff line are considered as contamination. Based on the imposed constraint, contaminants in control field is 2.5%. This cutoff is shown as straight line in Fig. 4.20. Sources lying towards right of this line is considered as initial set of likely YSOs. This set includes all the sources previously identified in Section 4.3 along with several other YSOs.

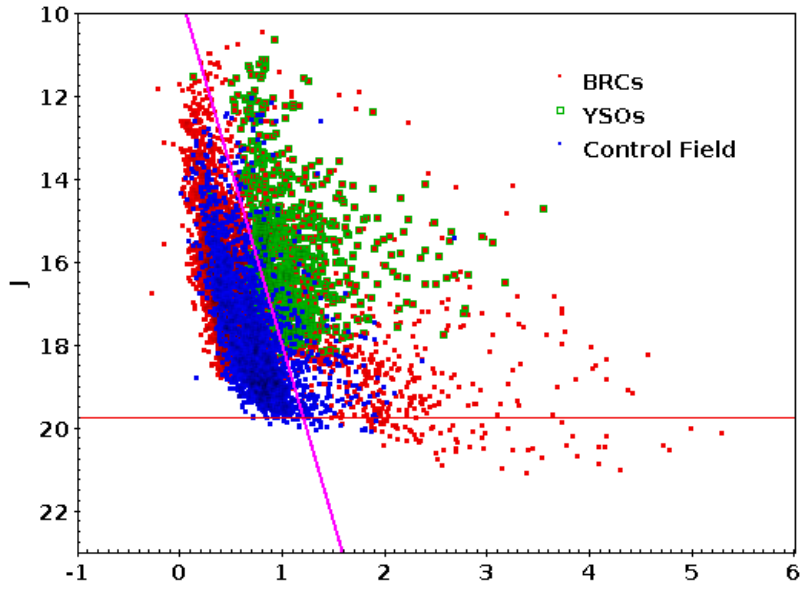
2. The depth of PanSTARRS is less than NEWFIRM, so there would be many YSOs whose photometric data in PanSTARR z band is not available. Using NEWFIRM CMD, the fainter YSOs can also be identified. Sources identified in last step is shown in Fig. 4.21(top) as green points. The same set of YSOs are then plotted on J versus $[J-K]$ CMD plot as green sources as shown in Fig. 4.21(bottom). Following the similar procedure of step 1, two distinct population can be seen in Fig. 4.21(bottom) also. Similar to step 1, an empirical cutoff is applied based on visual inspection which is given by;

$$[J] < 8.5 \times [J - K] + 9.50 \quad (4.2)$$

Sources falling rightward of the slant line in Fig. 4.21(b) are considered as final set of YSOs. Final set of YSOs are shown in Fig. 4.22(a) in green. This set includes all the YSOs identified in Section 4.3, Section 4.5 (step 1 and step 2). Control field shown in blue has 53.20 arcmin^2 with 2.5% contaminants. This can be scaled to area of BRC shown in Fig. 4.1 which is 262.15 arcmin^2 . After scaling contaminant percentage in final YSO list is 12.32%. The spatial distribution of the final population of identified YSOs is shown in Fig. 4.22(b).

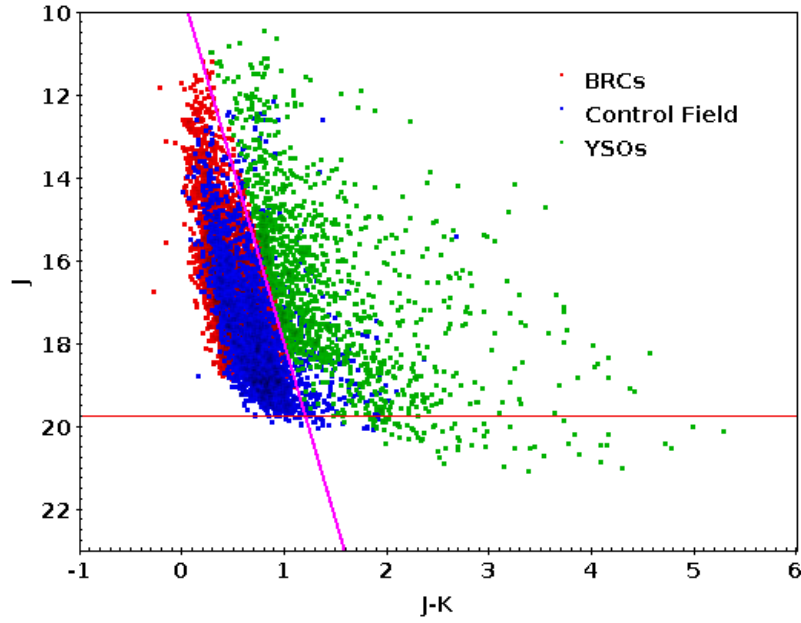


(a)

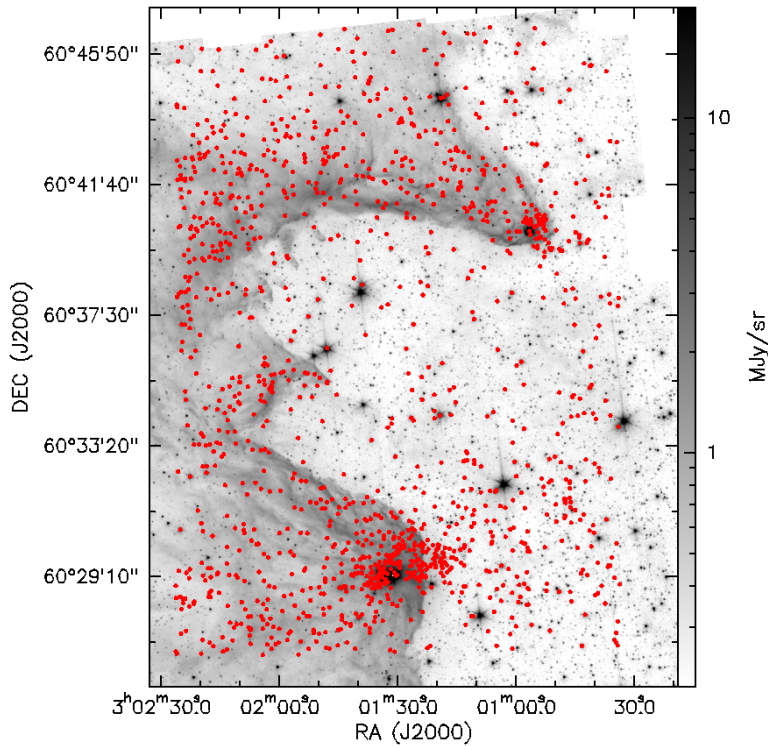


(b)

Figure 4.21: (a) CMD z versus $[z-K]$, sources identified in step 1 is shown in green. Straight magenta line is from eq. 4.1. (b) CMD plot showing $[J-K]$ color on horizontal axis and J magnitude on vertical axis. This plot is foreground extinction corrected. The mean foreground extinction is assumed to be $A_V = 2.0$ mag. BRC sources falling inside the box shown in Fig. 4.1 are shown in red. Blue sources are the control field sources. The Class I/II/III sources identified by Fig. 4.20 are shown in green. Line shown in magenta is the empirical cutoff (eq. 4.2) to identify second set of YSOs. Red horizontal line is 90% completeness limit in J band.



(a)



(b)

Figure 4.22: (a) CMD plot showing final set of YSOs in green. These are all the sources lying rightward to the magenta line in Fig. 4.21(b). The straight line of eq. 4.2 is plotted as magenta line. Red line shows the 90% completeness limit of J band. (b) Spatial distribution of YSOs identified in step 2 and shown in (a) in green.

4.6 Spatial coverage of BRCs from the stellar density map

To calculate the SFR and SFE, it is essential to identify the spatial coverage of BRCs and consider only those YSOs which fall within it and hence associated with the BRCs. To do so, this study uses stellar density map to identify the BRCs head. The stellar density map is shown in Fig. 4.23. Nearest neighbor (NN) method also called k -neighbour method is adopted for estimating the stellar density (Schmeja 2011). For each source in the region of study, we measure the radial distance to its j th nearest source. The resolution of the map depends on the choice of j . The j value is sensitive to statistical fluctuations for small values of j such as $j < 6$. While for large values of j such as $j > 30$ genuine clustering are likely to be smeared out (Schmeja 2011). In our case, we use $j = 16$. The expression for stellar density is given by;

$$\rho_j = \frac{j-1}{S(r_j)} m \quad (4.3)$$

Here, r_j is the distance to j th neighbour, $S(r_j)$ is circular area of radius r_j and m is average mass of source which is taken as 1 for stellar number density map (Schmeja 2011).

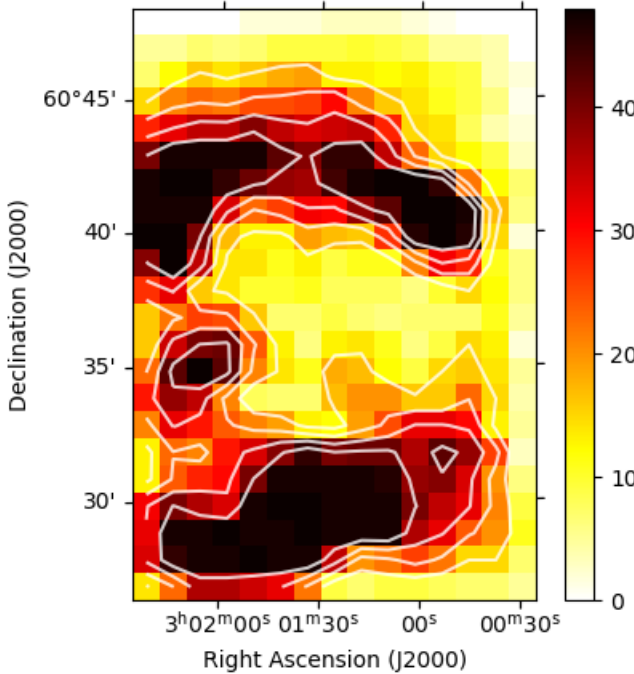


Figure 4.23: Stellar density map prepared with list of YSOs identified and shown in Fig. 4.22. The nearest neighbor method is used with $j = 16$. The contours plotted in white start from the 3σ threshold. The two identified contours are top right contour (for BRC 13) and bottom contour (for BRC14).

To identify the cluster associated with the BRCs, we consider only those sources that lie above a defined threshold of three times the background value (3σ). The contours are shown in Fig. 4.23. The mean background value for this map is estimated to be 5 source/arcmin 2 and the background threshold is taken as 3σ (=15 source/arcmin 2). The spatial distribution of YSOs falling inside the identified contour of Fig. 4.23 are shown in Fig. 4.24. The total number of YSOs likely to be associated with the BRCs are 188 for BRC 13 and 608 for BRC 14. These sources are now considered for total mass estimation and calculation of SFR and SFE.

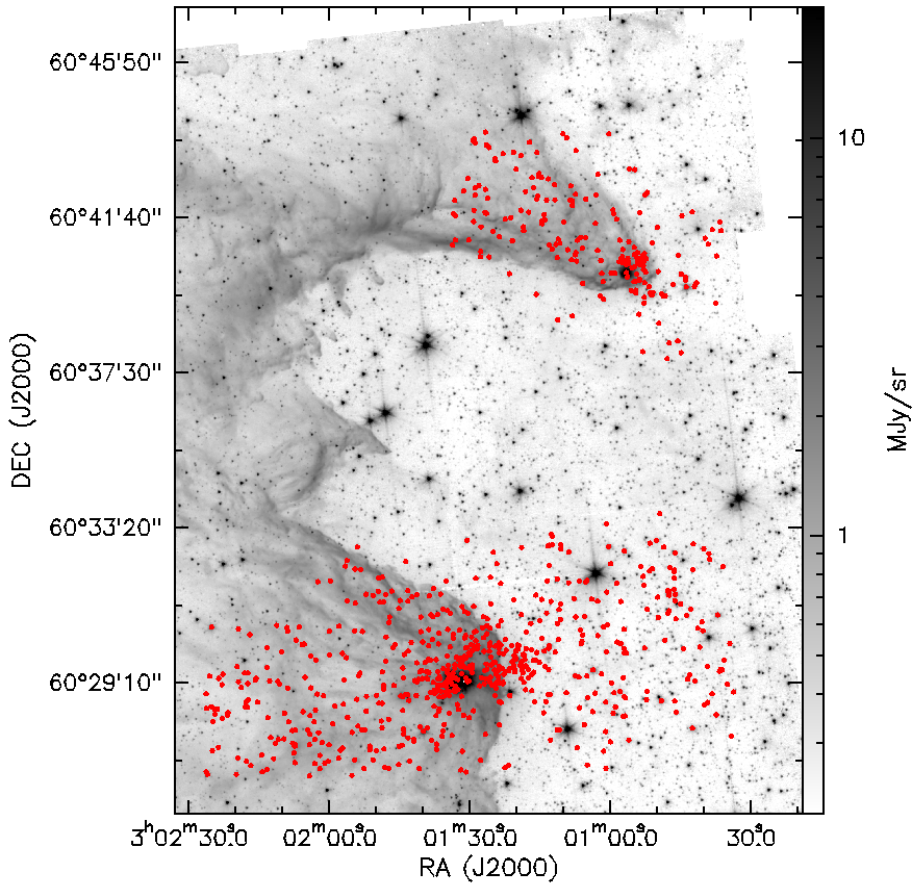


Figure 4.24: Spatial distribution of YSOs lying within the contours of Fig. 4.23. For BRC 13, top right contour is taken and for BRC 14 bottom contour is considered.

4.7 Mass estimation and Initial Mass Function (IMF)

To calculate the mass of each source shown in Fig. 4.24, the mass-magnitude relationship is used. This is a plot between the J band magnitude and $\log(M)$ derived from the 2 Myr isochrones Baraffe et al. (2015) (for $M < 1.40 M_{\odot}$) and Siess et al. (2000) (for $M > 1.40 M_{\odot}$). This plot is shown in Fig. 4.25. Using this empirical plot, masses of the individual sources associated with the BRCs are estimated. The corresponding IMF is plotted in Fig. 4.26. For plotting the IMF, the contaminants in each mass bin ($= 0.2$ dex) is statistically subtracted. Error for each mass bin is taken as the Poisson uncertainty. Fig. 4.26 also shows the power-law fit for $M > 0.5 M_{\odot}$ given by;

$$\frac{dN}{d\log(m)} = M^{\Gamma} \quad (4.4)$$

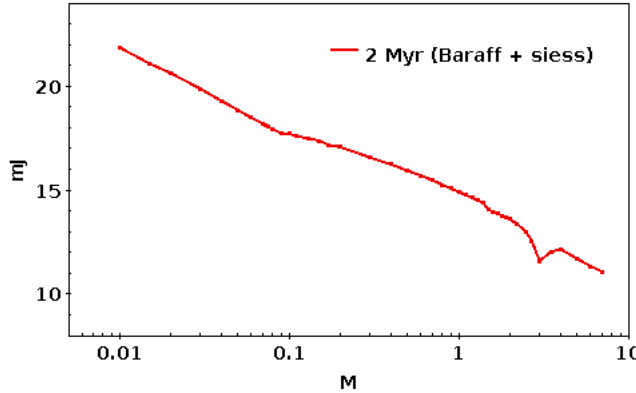


Figure 4.25: Mass-Magnitude relationship taken from Baraffe et al. (2015) for all sources with mass $< 1.40 M_{\odot}$ and from Siess et al. (2000) for mass $> 1.40 M_{\odot}$. The curve is for 2 Myr isochrone. The vertical axis is the J band magnitude and horizontal axis is showing mass in log scale.

The power-law fit for $M > 0.5 M_{\odot}$ yields a slope of $\Gamma = -1.25 \pm 0.19$ which is shown in Fig. 4.26. This is consistent with the classical Salpeter slope of $\Gamma = -1.35$. The IMF flattens at $M \sim 0.35 M_{\odot}$ and drops to lower mass regime. For low mass regime, we have fitted the log-normal distribution given by Chabrier (2003) for $M < 1.0 M_{\odot}$. The Chabrier mass function is given by;

$$\frac{dN}{d\log(m)} \propto \exp\left(-\frac{(m - m_o)^2}{2\sigma^2}\right) \quad (4.5)$$

where m_o is the peak mass and σ is the standard deviation of the Gaussian function. We

estimate $m_o = 0.319 M_\odot$ and $\sigma = 0.81$ dex. In comparison, for Galactic fields, the mass, m_o and σ are $0.25 M_\odot$ and 0.55 dex, respectively.

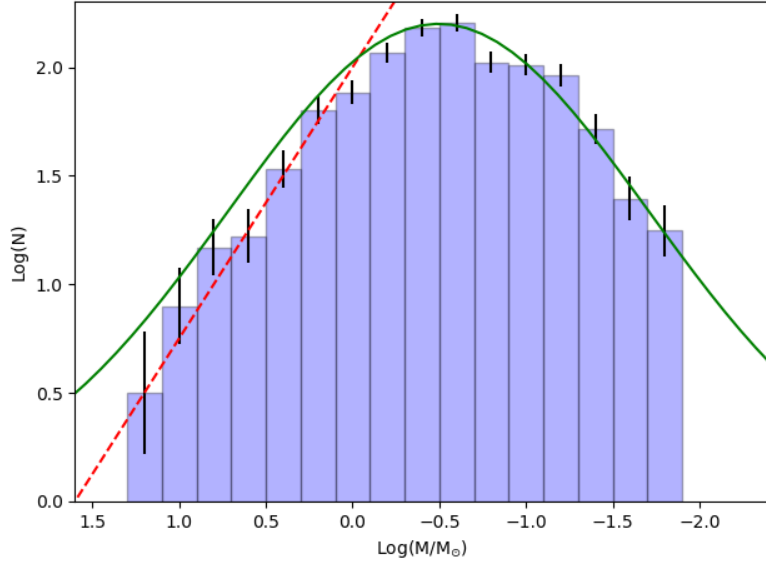


Figure 4.26: IMF estimated from mass-magnitude relationship after removal of contaminants in each mass bin. The bin size in this plot is 0.2 dex. The green curve represents the log-normal distribution by Chabrier (2003) which is fitted for sources $M < 1.0 M_\odot$. The red dotted line is the power-law fitted for sources $M > 0.5 M_\odot$ (Salpeter 1955). The error bars shown are Poisson uncertainty. This IMF presented is for the combined region for BRC 13 and BRC 14.

4.8 Star formation rate and star formation efficiency

To calculate SFE and SFR, all sources shown in Fig. 4.22 are considered. The Classical definition for SFR and SFE are given as (Evans II et al. 2009; Heiderman et al. 2010);

$$SFR = \frac{\sum M_{yso}(\text{ClassI/II/III})}{\langle AGE_{\text{ClassII}} \rangle} \quad (4.6)$$

$$SFE = \frac{\sum M_{yso}(\text{ClassI/II/III})}{\sum M_{yso}(\text{ClassI/II/III}) + \sum M_{\text{gas}}} \quad (4.7)$$

To calculate SFE, total gas mass of the cloud is required which can be determined as

follows (Heiderman et al. 2010);

$$M_{gas} = \mu m_H \left(\frac{N_{H+H_2}}{A_V} \right) \times \left(\frac{A_{pix}}{cm^2} \right) \times \sum \left(\frac{A_V}{mag} \right) \quad (4.8)$$

where A_{pix} is the area of pixel in cm^2 , N_{H+H_2} is column density for molecular and atomic hydrogen, m_H is mass of hydrogen in grams, μ is mean molecular weight which is taken as 1.37. The extinction calculated in Section 4.2.4 can be converted to column density by using the relation $N_{H+H_2} / A_V = 1.37 \times 10^{21} \text{ cm}^{-2} \text{ mag}^{-1}$. Using the column density derived from extinction map shown in Fig. 4.11, YSOs identified in Section 4.6 which are shown in Fig. 4.22 and with their mass obtained in Section 4.7, the calculation for SFE and SFR can be done as follows:

4.8.1 Estimation of SFE

For BRC 13, the SFE calculation is given below;

- Total YSOs within the contour = 188
- Total sum of YSOs mass (M_{yso}) = $113.44 M_{\odot}$
- Total number of pixel covered by contour = 35
- Total sum of A_V over contour = 230.89 mag
- Total Mass of gas within contour = $1111.79 M_{\odot}$
- $SFE = \sum M_{yso} / \sum M_{yso} + \sum M_{gas} = 0.092 (9.2\%)$

Similarly for BRC 14, the SFE calculation is given below;

- Total YSOs within the contour = 607
- Total sum of YSOs mass (M_{yso}) = $343.706 M_{\odot}$
- Total number of pixel covered by contour = 88
- Total sum of A_V over contour = 575.41 mag
- Total Mass of gas within contour = $2769.422 M_{\odot}$
- $SFE = \sum M_{yso} / \sum M_{yso} + \sum M_{gas} = 0.1104 (11.04\%)$

4.8.2 Estimation of SFR

For BRC 13, the SFR calculation is given below;

- Total number of pixel covered by contour = 35
- Total area covered by contour = 11.846 pc^2
- Total sum of YSOs mass (M_{yso}) = 113.44 M_\odot
- Average Class II YSO age within contour = 0.99 Myr
- $\text{SFR} = M_{yso} / \langle \text{Class II age} \rangle = 0.144 \times 10^{-3} \text{ M}_\odot/\text{yr} = 114.58 \text{ M}_\odot/\text{Myr}$
- Star formation rate density $\sum_{SFR} = \text{SFR}_{BRC13} / \text{Area}_{BRC13} = 9.672 \text{ M}_\odot/\text{Myr}/\text{pc}^2$

Similarly for BRC 14, the SFR calculation is given below;

- Total number of pixel covered by contour = 88
- Total area covered by contour = 29.785 pc^2
- Total sum of YSOs mass (M_{yso}) = 343.706 M_\odot
- Average Class II YSO age within contour = 1.459 Myr
- $\text{SFR} = M_{yso} / \langle \text{Class II age} \rangle = 0.235 \times 10^{-3} \text{ M}_\odot/\text{yr} = 235.57 \text{ M}_\odot/\text{yr}$
- Star formation rate density $\sum_{SFR} = \text{SFR}_{BRC14} / \text{Area}_{BRC14} = 7.910 \text{ M}_\odot/\text{Myr}/\text{pc}^2$

4.9 Discussion

Schmidt (1959) proposed a power-law relation between star formation rate density \sum_{SFR} and gas mass density \sum_{gas} with a power-law index N given by;

$$\sum_{SFR} \propto \left(\sum_{gas} \right)^N \quad (4.9)$$

Kennicutt Jr (1998) fitted the SFR density and gas mass density for extra-galactic observations and estimated to be $N = 1.4 \pm 0.15$. The relation obtained by these authors is;

$$\sum_{SFR} = (2.5 \pm 0.7) \times 10^{-4} \left(\frac{\sum_{gas}}{M_\odot \text{pc}^{-2}} \right)^{1.4 \pm 0.15} (M_\odot \text{Myr}^{-1} \text{pc}^{-2}) \quad (4.10)$$

and is known as the *Kennicutt-Schmidt Law*. This is shown in Fig. 4.27 as blue straight line. The horizontal axis of this plot shows $\log \sum_{gas}$ and the vertical axis plots $\log \sum_{SFR}$. Values obtained in Section 4.8 is shown in this plot along with results from several other studies which were obtained using the Spitzer c2d survey. These are Aleala et al. (2008) Chamaeleon II dark cloud, Marin et al. (2008) for Lupus cloud, Lai et al. (2008) for the Perseus cloud, Harvey et al. (2007) for the Serpens cloud and Davis et al. (1994) for the Ophiuchus cloud. All these studies have calculated SFR and SFE for the clouds and these are shown in the Kennicutt-Schmidt diagram (Fig. 4.27). Looking at Fig. 4.27, it can be inferred that the result obtained for BRC 13 and BRC 14 is consistent with the rest of the studies.

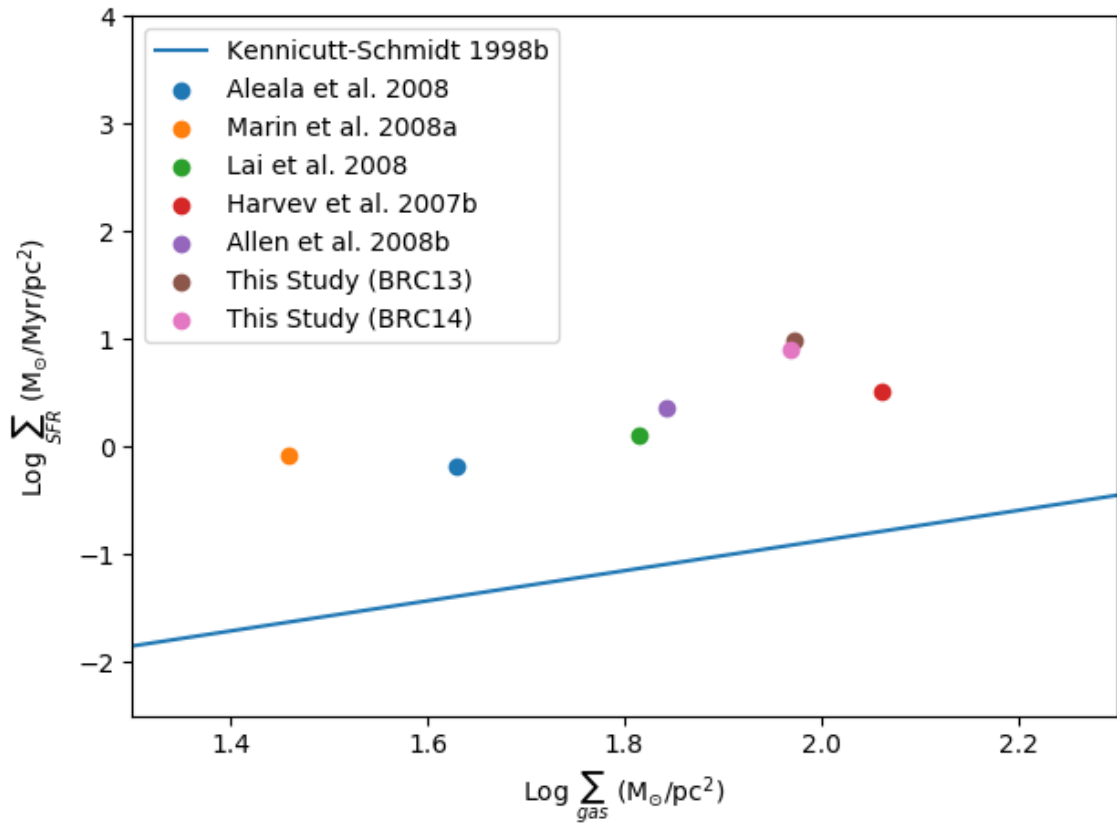


Figure 4.27: Kennicutt-Schmidt diagram. The blue line shows the Kennicutt-Schmidt law given by eq. 4.10 (Kennicutt Jr 1998). Horizontal axis shows the log of gas mass density and vertical axis shows the log of the SFR. Data from various other studies (Aleala et al. 2008; Marin et al. 2008; Lai et al. 2008; Harvey et al. 2007; Allen & Davis 2008) are also shown.

Results obtained in Section 4.8, along with results from above mentioned studies for differ-

ent clouds, can be used to understand correlations between YSO number density N_{YSO}/pc^2 and SFE, SFR and SFRD which are shown in Fig. 4.28, Fig. 4.29 and Fig. 4.30, respectively. All three plots shows a positive correlation between N_{YSO}/pc^2 and (SFE, SFR, SFRD).

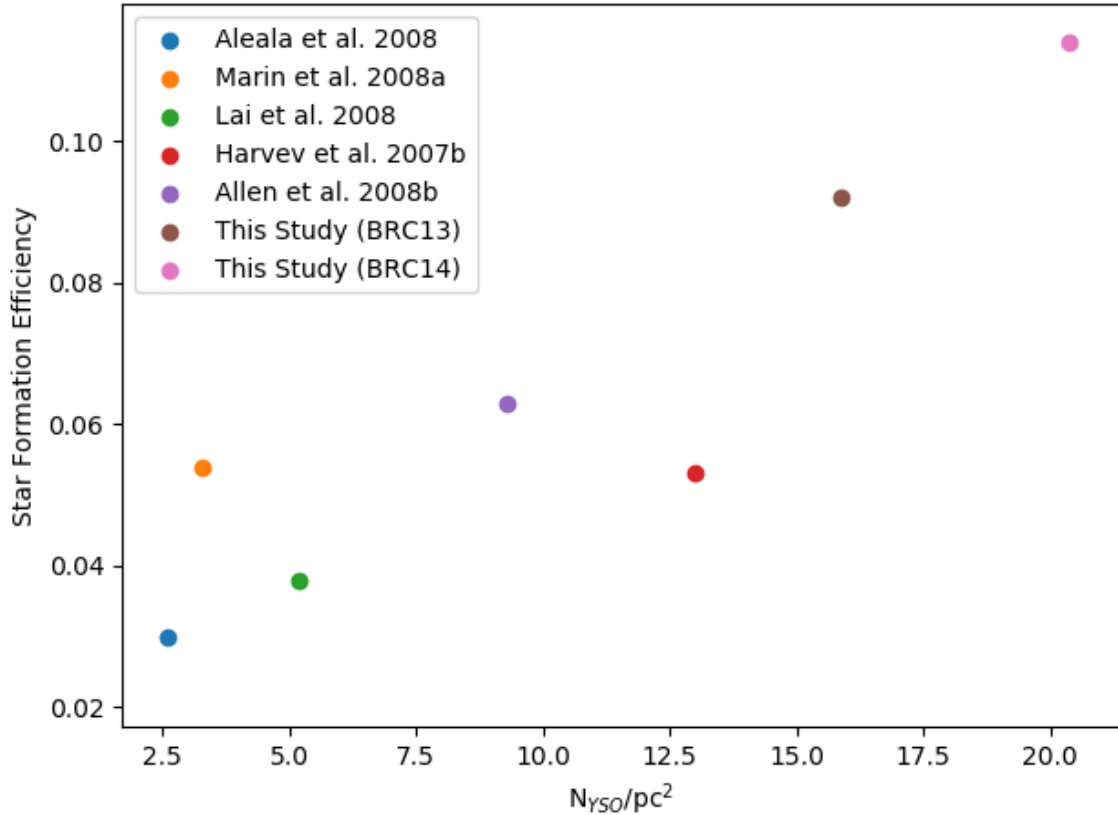


Figure 4.28: YSO density as a function of the SFE. Data from various other studies (Aleala et al. 2008; Marin et al. 2008; Lai et al. 2008; Harvey et al. 2007; Allen & Davis 2008) are also shown.

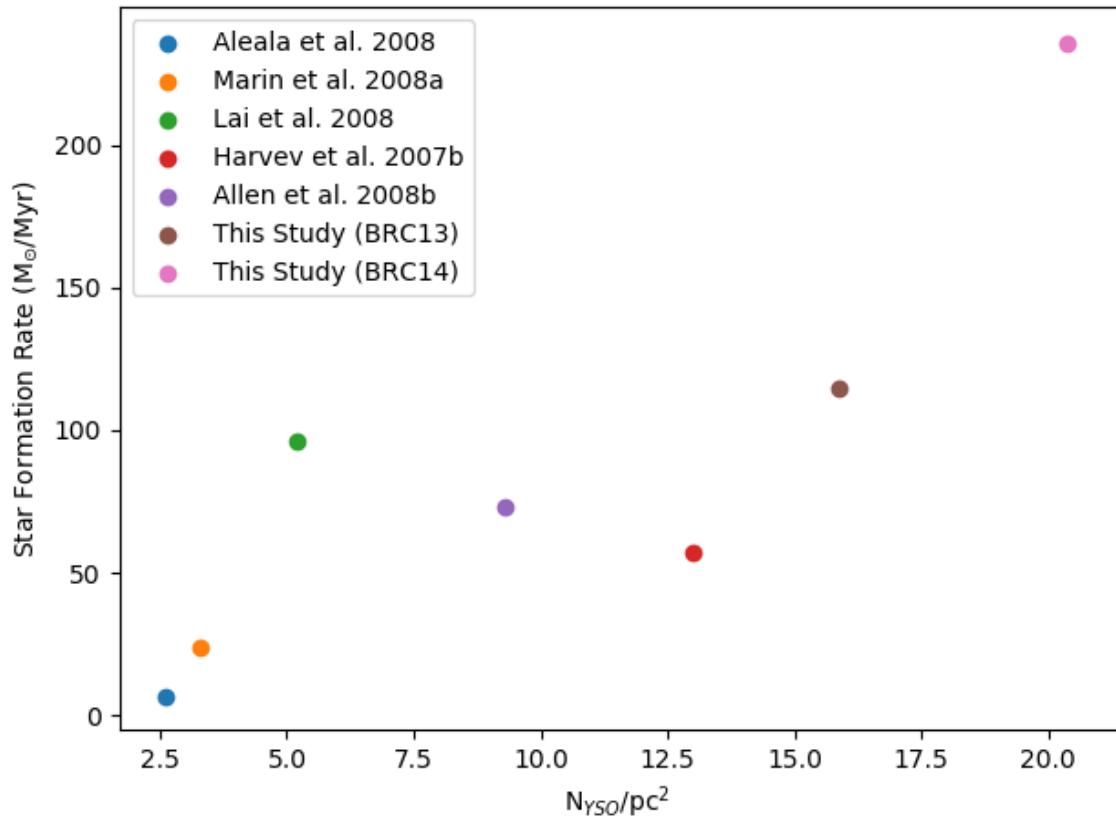


Figure 4.29: YSO density as a function of the SFR. Data from various other studies (Aleala et al. 2008; Marin et al. 2008; Lai et al. 2008; Harvey et al. 2007; Allen & Davis 2008) are also shown.

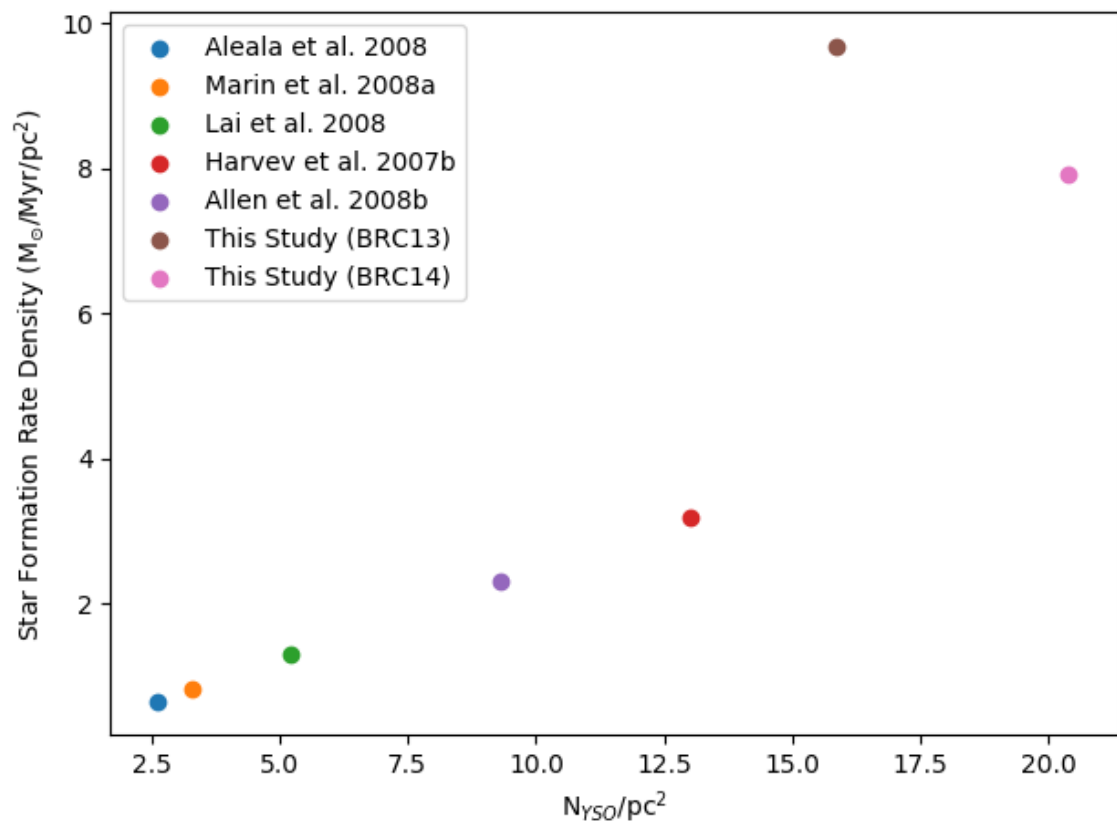


Figure 4.30: YSO density as a function of SFRD. Data from various other studies (Aleala et al. 2008; Marin et al. 2008; Lai et al. 2008; Harvey et al. 2007; Allen & Davis 2008) are also shown.

Chapter 5

Conclusion

Star formation under feedback driven environment is one of the least understood problems in Astrophysics. The main scientific goal of this project is to understand the star formation activity in Bright Rimmed Clouds (BRCs), which are well known examples for ongoing star formation activity in feedback driven environments. The two regions selected for this study are BRC 13 and BRC 14. These BRCs are located at a distance of ~ 2.30 kpc in W5 giant molecular complex, which is in the Perseus arm of the Galaxy. The main ionizing source for the W5E H II region is the massive star HD 18326 at the center of the massive star cluster IC1848-east. This study utilizes multi-wavelength photometric data from PanSTARRS PS1 survey in optical, NEWFIRM-JHK_s observations in the NIR and deep Spitzer-IRAC data in MIR. To our knowledge, this is the deepest multi-wavelength catalog for this region. The photometric results from NEWFIRM and Spitzer images, along with PS1 catalog data are used to derive the following key results:

- Using the photometric data in JHK_s band from 2MASS point source catalog, the extinction map for the region was generated using the machine learning based tool PNICER. The extinction in V band lies in the range of 0.30 to 10.60 mag. The distribution of A_V peaks at ~ 2.50 mag. The FOV of the extinction map is 0.5 deg² and resolution is 0.5'.
- For identification of Class I/II sources, various color criteria given in Gutermuth et al. (2005, 2009) are used. This involves CC diagram [K - CH1] / [CH1 - CH2]. Total of 195 Class II and 14 Class I sources are identified in the combined BRC 13 and BRC 14 regions. Spatial distribution of these sources show clustering at the head of the two BRCs.
- Using the VOSA SED analyzer tool, SEDs of all the 14 Class I and 195 Class II sources are generated where the BT-Settle models are utilized. Results of this SED

modelling include the T_{eff} and luminosity for each source based on which the HR diagram is generated.

- The HR diagram is used to estimate the mass and age for each Class I/II pre-main sequence sources. For this purpose, isochrones and evolutionary tracks from Siess et al. (2000) are used. Minimum and maximum mass obtained are $0.107 \pm 0.001 M_{\odot}$ and $2.842 \pm 0.18 M_{\odot}$, respectively. Minimum and maximum ages are 0.112 ± 0.008 Myr and 4.455 ± 1.722 Myr, respectively. Average age of candidate pre-main sequence members of BRCs are found to be ~ 2 Myr.
- Using a suitable control field, Class III sources are also identified. This is done by plotting foreground extinction corrected $z / [z-K]$ and $J / [J-K]$ CMDs. After visual inspection of these two CMDs, an empirical color cutoff is imposed to distinguish Class I/II/III from field stars. The final list of YSOs are expected to have $\sim 12.32\%$ contamination.
- The spatial coverage of BRCs is estimated from the stellar density map constructed using the nearest neighbour method. Sources lying above the 3σ threshold are considered as associated with the BRCs. Total 188 and 608 YSOs are found to be associated with BRC 13 and BRC 14 clusters, respectively.
- Estimation of mass for individual BRC cluster member is done using mass-magnitude relationship derived from the 2 Myr isochrone of Siess et al. (2000). The IMF of the stellar distribution peaks at $0.319 M_{\odot}$ with $\sigma = 0.81$ dex. The slope above $0.5 M_{\odot}$ is $\Gamma = -1.25 \pm 0.19$ which is consistent with the classical Salpeter value i.e., -1.35.
- From the stellar mass and underlying gas mass, the star formation efficiencies are estimated for BRC 13 and BRC 14 as 9.20% and 11.04%, respectively. For BRC 13, SFR estimated to be $\sim 114.58 M_{\odot}/\text{Myr}$ and for BRC 14, SFR is $\sim 235.57 M_{\odot}/\text{Myr}$. Star formation rate density is also estimated for BRC 13 and BRC 14, which turns out to be $9.672 M_{\odot}/\text{Myr}/\text{pc}^2$ and $7.910 M_{\odot}/\text{Myr}/\text{pc}^2$, respectively.
- In this preliminary analysis of feedback driven BRCs, we do not find any strong variation in the form of stellar IMF. Also, the SFE and SFRs estimated are within the range of values expected for star forming regions.

Bibliography

- Adams, F. C., Lada, C. J., & Shu, F. H. 1987, *The Astrophysical Journal*, 312, 788
- Aleala, J. M., Spezzi, L., Chapman, N., et al. 2008, *The Astrophysical Journal*, 676, 427
- Allen, M. & Davis, C. J. 2008
- Aspin, C., Sandell, G., & Russell, A. 1994, *Astronomy and Astrophysics Supplement Series*, 106, 165
- Axford, W. I. 1964, *The Astrophysical Journal*, 140, 112
- Bally, J., Devine, D., & Reipurth, B. 1996, *The Astrophysical Journal Letters*, 473, L49
- Bally, J., Reipurth, B., Lada, C. J., & Billawala, Y. 1999, *The Astronomical Journal*, 117, 410
- Bally, J., Walawender, J., Johnstone, D., et al. 2008, *Reipurth* (San Francisco, CA: ASP), 459
- Baraffe, I., Homeier, D., Allard, F., & Chabrier, G. 2015, *Astronomy & Astrophysics*, 577, A42
- Bayo, A., Rodrigo, C., y Navascués, D. B., et al. 2008, *Astronomy & Astrophysics*, 492, 277
- Bertoldi, F. 1989, *The Astrophysical Journal*, 346, 735
- Bertoldi, F. & McKee, C. F. 1990, *The Astrophysical Journal*, 354, 529
- Bessell, M. & Brett, J. 1988, *Publications of the Astronomical Society of the Pacific*, 100, 1134

- Bisbas, T. G., Wünsch, R., Whitworth, A. P., Hubber, D. A., & Walch, S. 2011, The Astrophysical Journal, 736, 142
- Castor, J., McCray, R., & Weaver, R. 1975a, The Astrophysical Journal, 200, L107
- Castor, J. I., Abbott, D. C., & Klein, R. I. 1975b, The Astrophysical Journal, 195, 157
- Chabrier, G. 2003, Publications of the Astronomical Society of the Pacific, 115, 763
- Chauhan, N., Pandey, A., Ogura, K., et al. 2011, Monthly Notices of the Royal Astronomical Society, 415, 1202
- Chauhan, N., Pandey, A., Ogura, K., et al. 2009, Monthly Notices of the Royal Astronomical Society, 396, 964
- Cohen, J. G., Frogel, J. A., Persson, S., & Elias, J. H. 1981, Astrophysical Journal, 249, 481
- Dale, J., Ercolano, B., & Bonnell, I. 2012, Monthly Notices of the Royal Astronomical Society, 424, 377
- Dale, J., Ercolano, B., & Bonnell, I. 2013, Monthly Notices of the Royal Astronomical Society, 430, 234
- Dale, J. E., Bonnell, I., & Whitworth, A. 2007, Monthly Notices of the Royal Astronomical Society, 375, 1291
- Davis, L. E. et al. 1994, IRAF Programming Group, NOAO, Tucson
- Deharveng, L., Schuller, F., Anderson, L., et al. 2010, Astronomy & Astrophysics, 523, A6
- Deharveng, L., Zavagno, A., Anderson, L., et al. 2012, Astronomy & Astrophysics, 546, A74
- Dutta, S., Mondal, S., Samal, M. R., & Jose, J. 2018, The Astrophysical Journal, 864, 154
- Dyson, J. E. & Williams, D. A. 1997, The physics of the interstellar medium (CRC Press)
- Elmegreen, B. G. & Lada, C. J. 1977, The Astrophysical Journal, 214, 725
- Evans II, N. J., Dunham, M. M., Jørgensen, J. K., et al. 2009, The Astrophysical Journal Supplement Series, 181, 321

- Fall, S. M., Krumholz, M. R., & Matzner, C. D. 2010, *The Astrophysical Journal Letters*, 710, L142
- Fischera, J. & Martin, P. G. 2012, *Astronomy & Astrophysics*, 547, A86
- Flaherty, K. M., Pipher, J., Megeath, S., et al. 2007, *The Astrophysical Journal*, 663, 1069
- Franco, J., Tenorio-Tagle, G., & Bodenheimer, P. 1990, *The Astrophysical Journal*, 349, 126
- Greene, T. P. & Lada, C. J. 1996, *The Astronomical Journal*, 112, 2184
- Gritschneider, M., Naab, T., Walch, S., Burkert, A., & Heitsch, F. 2009, *The Astrophysical Journal Letters*, 694, L26
- Gutermuth, R., Megeath, S., Myers, P., et al. 2009, *The Astrophysical Journal Supplement Series*, 184, 18
- Gutermuth, R. A., Megeath, S. T., Pipher, J. L., et al. 2005, *The Astrophysical Journal*, 632, 397
- Harvey, P., Merín, B., Huard, T. L., et al. 2007, *The Astrophysical Journal*, 663, 1149
- Hauschildt, P. H., Allard, F., Alexander, D. R., Schweitzer, A., & Baron, E. 1996, in *Symposium-International Astronomical Union*, Vol. 176, Cambridge University Press, 539–546
- Hauschildt, P. H. & Baron, E. 1999, *Journal of Computational and Applied Mathematics*, 109, 41
- Heiderman, A., Evans II, N. J., Allen, L. E., Huard, T., & Heyer, M. 2010, *The Astrophysical Journal*, 723, 1019
- Henney, W. J., Arthur, S. J., De Colle, F., & Mellem, G. 2009, *Monthly Notices of the Royal Astronomical Society*, 398, 157
- Hildebrand, R. H. 1983
- Hodapp, K., Kaiser, N., Aussel, H., et al. 2004, *Astronomische Nachrichten: Astronomical Notes*, 325, 636
- Hosokawa, T. & Omukai, K. 2009, *The Astrophysical Journal*, 691, 823

- Howell, S. B. 1989, *Publications of the Astronomical Society of the Pacific*, 101, 616
- Indebetouw, R. 2015, *IAU General Assembly*, 22
- Kahn, F. 1958, *Reviews of Modern Physics*, 30, 1058
- Kahn, F. 1969, *Physica*, 41, 172
- Kahn, F. et al. 1954, *Bulletin of the Astronomical Institutes of the Netherlands*, 12, 187
- Kaiser, N., Burgett, W., Chambers, K., et al. 2010, in *Ground-based and Airborne Telescopes III*, Vol. 7733, International Society for Optics and Photonics, 77330E
- Karr, J. & Martin, P. 2003, *The Astrophysical Journal*, 595, 900
- Kennicutt Jr, R. C. 1998, *The Astrophysical Journal*, 498, 541
- Kessel-Deynet, O. & Burkert, A. 2003, *Monthly Notices of the Royal Astronomical Society*, 338, 545
- Knee, L. & Sandell, G. 2000, *Astronomy and Astrophysics*, 361, 671
- Koenig, X. P., Allen, L. E., Gutermuth, R. A., et al. 2008, *The Astrophysical Journal*, 688, 1142
- Krumholz, M. R., Bate, M. R., Arce, H. G., et al. 2014, *Protostars and Planets VI*, 243
- Krumholz, M. R. & Matzner, C. D. 2009, *The Astrophysical Journal*, 703, 1352
- Krumholz, M. R., Matzner, C. D., & McKee, C. F. 2006, *The Astrophysical Journal*, 653, 361
- Kudritzki, R., Pauldrach, A., Puls, J., & Abbott, D. 1989, *Astronomy and Astrophysics*, 219, 205
- Kudritzki, R., Puls, J., Lennon, D., et al. 1999, arXiv preprint astro-ph/9910449
- Lada, C. J. 2006, *The Astrophysical Journal Letters*, 640, L63
- Lada, C. J. & Lada, E. A. 2003, *Annual Review of Astronomy and Astrophysics*, 41, 57
- Lai, S.-P., Padgett, D. L., Rebull, L. M., et al. 2008, *The Astrophysical Journal*, 672, 1013
- Lefloch, B. & Lazareff, B. 1994, *Astronomy and Astrophysics*, 289, 559

- Lefloch, B. & Lazareff, B. 1995, *Astronomy and Astrophysics*, 301, 522
- Lopez, L. A., Krumholz, M. R., Bolatto, A. D., PROCHASkA, J. X., & Ramirez-Ruiz, E. 2011, *The Astrophysical Journal*, 731, 91
- Lopez, L. A., Krumholz, M. R., Bolatto, A. D., et al. 2014, *The Astrophysical Journal*, 795, 121
- Magnier, E. 2006, Maui, HI: MEDB, 50
- Magnier, E. 2007, in *The Future of Photometric, Spectrophotometric and Polarimetric Standardization*, Vol. 364, 153
- Magnier, E., Liu, M., Monet, D., & Chambers, K. 2007, *Proceedings of the International Astronomical Union*, 3, 553
- Marin, B., Jørgensen, J., Spezzi, L., et al. 2008, *The Astrophysical Journal Supplement Series*, 177, 551
- Martin, P. G., Roy, A., Bontemps, S., et al. 2012, *The Astrophysical Journal*, 751, 28
- McKee, C. F. 1989, *The Astrophysical Journal*, 345, 782
- Meingast, S., Lombardi, M., & Alves, J. 2017, *Astronomy & Astrophysics*, 601, A137
- Meyer, M. R., Calvet, N., & Hillenbrand, L. A. 1997, *The Astronomical Journal*, 114, 288
- Miao, J., White, G. J., Nelson, R., Thompson, M., & Morgan, L. 2006, *Monthly Notices of the Royal Astronomical Society*, 369, 143
- Miao, J., White, G. J., Thompson, M., & Nelson, R. P. 2009, *The Astrophysical Journal*, 692, 382
- Newman, R. & Axford, W. 1968, *The Astrophysical Journal*, 153, 595
- Norman, C. & Silk, J. 1980, *The Astrophysical Journal*, 238, 158
- Ogura, K. 2010, in *Astronomical Society of India Conference Series*, Vol. 1
- Ohlendorf, H., Preibisch, T., Gaczkowski, B., et al. 2013, *Astronomy & Astrophysics*, 552, A14

Onaka, P., Tonry, J., Isani, S., et al. 2008, in Ground-based and Airborne Instrumentation for Astronomy II, Vol. 7014, International Society for Optics and Photonics, 70140D

Oort, J. H., Spitzer, L. J., et al. 1955, *Astrophysical Journal*, 121

Osterbrock, D. 1974, Institute for Advanced Studies, and National Science Foundation. San Francisco, WH Freeman and Co, 263, 224

Osterbrock, D. E. & Ferland, G. J. 2006, *Astrophysics Of Gas Nebulae and Active Galactic Nuclei* (University science books)

Pandey, A., Sharma, S., Ogura, K., et al. 2008, *Monthly Notices of the Royal Astronomical Society*, 383, 1241

Panwar, N., Chen, W., Pandey, A., et al. 2014, *Monthly Notices of the Royal Astronomical Society*, 443, 1614

Pauldrach, A., Puls, J., & Kudritzki, R. 1986, *Astronomy and Astrophysics*, 164, 86

Pavlakis, K., Williams, R., Dyson, J., Falle, S., & Hartquist, T. 2001, *Astronomy & Astrophysics*, 369, 263

Pecaut, M. J. & Mamajek, E. E. 2013, *The Astrophysical Journal Supplement Series*, 208, 9

Pellegrini, E. W., Baldwin, J. A., & Ferland, G. J. 2011, *The Astrophysical Journal*, 738, 34

Pottasch, S. et al. 1956, *Bulletin of the Astronomical Institutes of the Netherlands*, 13, 77

Pottasch, S. et al. 1958, *Bulletin of the Astronomical Institutes of the Netherlands*, 14, 29

Pottasch, S. R. 1958, in *Symposium-International Astronomical Union*, Vol. 8, Cambridge University Press, 1053–1058

Preibisch, T., Ossenkopf, V., Yorke, H., & Henning, T. 1993, *Astronomy and Astrophysics*, 279, 577

Rieke, G. & Lebofsky, M. 1985, *The Astrophysical Journal*, 288, 618

Robitaille, T. P., Whitney, B. A., Indebetouw, R., & Wood, K. 2007, *The Astrophysical Journal Supplement Series*, 169, 328

- Roy, A., Martin, P. G., Polychroni, D., et al. 2013, *The Astrophysical Journal*, 763, 55
- Salpeter, E. E. 1955, *The Astrophysical Journal*, 121, 161
- Samal, M., Ojha, D., Jose, J., et al. 2015, *Astronomy & Astrophysics*, 581, A5
- Sandell, G. & Knee, L. 2001, in *Science with the Atacama Large Millimeter Array*, Vol. 235, 154
- Sandford, M., Whitaker, R., & Klein, R. 1982, *The Astrophysical Journal*, 260, 183
- Schlafly, E., Finkbeiner, D., Jurić, M., et al. 2012, *The Astrophysical Journal*, 756, 158
- Schmeja, S. 2011, *Astronomische Nachrichten*, 332, 172
- Schmidt, M. 1959, *The Astrophysical Journal*, 129, 243
- Scoville, N., Polletta, M., Ewald, S., et al. 2001, *The Astronomical Journal*, 122, 3017
- Sharma, S., Pandey, A., Borissova, J., et al. 2016, *The Astronomical Journal*, 151, 126
- Siess, L., Dufour, E., & Forestini, M. 2000, arXiv preprint astro-ph/0003477
- Skrutskie, M., Cutri, R., Stiening, R., et al. 2006, *The Astronomical Journal*, 131, 1163
- Smeingast. 2017, smeingast/PNICER
- Spitzer Jr, L. 1954, *The Astrophysical Journal*, 120, 1
- Spitzer Jr, L. 2008, *Physical processes in the interstellar medium* (John Wiley & Sons)
- Stahler, S. W. & Palla, F. 2008, *The formation of stars* (John Wiley & Sons)
- Stern, D., Eisenhardt, P., Gorjian, V., et al. 2005, *The Astrophysical Journal*, 631, 163
- Stubbs, C. W., Doherty, P., Cramer, C., et al. 2010, *The Astrophysical Journal Supplement Series*, 191, 376
- Sugitani, K. 1989, in *The Physics and Chemistry of Interstellar Molecular Clouds: mm and Sub-mm Observations in Astrophysics* (Springer), 112–113
- Sugitani, K., Fukui, Y., & Ogura, K. 1991, *the Astrophysical Journal Supplement Series*, 77, 59

- Sugitani, K. & Ogura, K. 1994, *The Astrophysical Journal Supplement Series*, 92, 163
- Sugitani, K., Tamura, M., & Ogura, K. 1995, *The Astrophysical Journal Letters*, 455, L39
- Tan, J. C., Beltrán, M. T., Caselli, P., et al. 2014, *Protostars and Planets VI*, 149
- Tenorio-Tagle, G., Bodenheimer, P., Rozyczka, M., & Franco, J. 1986, *Astronomy and Astrophysics*, 170, 107
- Tonry, J., Stubbs, C. W., Lykke, K. R., et al. 2012, *The Astrophysical Journal*, 750, 99
- Vink, J. S., de Koter, A., & Lamers, H. J. 2000, arXiv preprint astro-ph/0008183
- Walawender, J., Bally, J., & Reipurth, B. 2005, *The Astronomical Journal*, 129, 2308
- Warin, S., Benayoun, J., & Viala, Y. 1996, *Astronomy and Astrophysics*, 308, 535
- Wasserburg, G., Black, D., & Matthews, M. 1985, University of Arizona Press, Tucson, 703
- Whitworth, A. P., Bhattal, A. S., Chapman, S. J., Disney, M. J., & Turner, J. A. 1994, *Monthly Notices of the Royal Astronomical Society*, 268, 291
- Zavagno, A., Deharveng, L., Comeron, F., et al. 2006, *Astronomy & Astrophysics*, 446, 171